

EXPLORATION OF STRUCTURE-PROPERTY RELATIONSHIP AND
GROWTH MECHANISM OF 1D NANOWIRES USING TRANSMISSION
ELECTRON MICROSCOPY

by

Manira Akter

A dissertation submitted to the faculty of
The University of North Carolina at Charlotte
in partial fulfillment of the requirements
for the degree of Doctor of Philosophy in
Mechanical Engineering

Charlotte

2023

Approved by:

Dr. Terry Xu

Dr. Haitao Zhang

Dr. Youxing Chen

Dr. Thomas Schmedake

ABSTRACT

MANIRA AKTER. Exploration of Structure-Property Relationship and Growth Mechanism of 1D Nanowires Using Transmission Electron Microscopy. (Under the direction of DR. TERRY XU)

One-dimensional (1D) nanostructured materials, e.g., nanowires (NWs) have fascinating properties and applications in various fields including electronic and energy conversion devices. Despite tremendous progress in the NW research field, a thorough understanding of NW structure-properties correlation and their rational synthesis with desired properties are two main roadblocks to the wider application of different types of NWs, which are the main focus of this dissertation.

The first part of this dissertation is a collaborative work, and the goal was to find if any correlation exists between structural parameters, morphology (such as lattice constants and dimensions), and thermal properties of niobium selenide (NbSe_3) NWs. NbSe_3 is a chain-like structure with molecular chains joined by van der Waals (VdW) force and suitable for the exploration of the effect of electron-phonon (e-ph) interaction on thermal conductivity. However, superdiffusive thermal transport was observed for ultra-thin NbSe_3 NWs (hydraulic diameter <26 nm), which led us to measure the structural parameters and investigate their interrelation with the observed properties. Individual NW was examined using a transmission electron microscope (TEM) to obtain high-resolution TEM images, diffraction patterns (DP), and morphology at lower magnifications. But while examining NbSe_3 NW, it was discovered that the NW needs to be tilted out-of-plane to obtain all the lattice parameters. The process is constrained due to the tilt limitation in the TEM. A DP roadmap was built from the measured and simulated DPs to facilitate the TEM examination and analysis. The obtained results eliminated the structural effect from the unusual thermal properties and led to considering other factors (change in heat capacity and Debye temperature) to explain the phenomenon.

For the second part of this work, the growth mechanism of boron carbide NWs was explored using TEM-based cross-sectional examination. Because of their unusual structural complexity and exceptional bonding, boron carbide materials are known for their excellent chemical and physical properties and have potential applications in high-temperature thermoelectric devices. To obtain improved thermoelectric performance, our previous group members synthesized boron carbide NWs and performed extensive characterization of their structures and thermal properties. However, rational synthesis of boron carbide NWs with desired properties could not be obtained yet. For this purpose, a thorough understanding of the growth mechanism is crucial.

To investigate the growth mechanism and understand the effect of each reaction parameter, cross-sectional TEM examinations were conducted on multiple growth substrates. Those substrates were prepared in different experimental conditions with varying reaction parameters (Ni film as a catalyst, diborane and methane as precursor gases, and annealing temperature and time). During the annealing of Ni film on the SiO₂/Si substrate, catalyst-substrate interaction could be observed. The contrast in the TEM images demonstrated that Ni film agglomerated into particles and diffused into the SiO₂ layer. Also, voids were formed in the SiO₂, which could be nucleated due to the coincidence of the microchannels in the SiO₂ and stress in the Ni film/substrate interface during annealing. Higher temperatures showed a contradictory trend in the agglomeration and void nucleation behavior. Diborane was seen to etch the SiO₂ layer and facilitate the diffusion of the particles whereas methane exhibited the opposite effect. Some nanostructures with a catalyst on top grew in the latter case. Diborane and methane together generated thin films with nanostructures in the absence of Ni film. It can be hypothesized that Ni-catalyzed diborane species cause the etching of the SiO₂ which is suppressed when both precursors are present. With all the reaction parameters present in the chamber, the diborane and methane react predominantly to form B_xC_y film, and NWs grow from this film with the help of the

catalyst. Although etching is prevented, the diffusion of particles into SiO₂ could still be observed. Compositional analysis of the particles and nanostructures and cross-sectional examination of more growth substrates are required to verify the hypothesis. Despite the lack of compositional information, cross-sectional TEM images presented in this dissertation provide useful data such as the interaction of the catalyst with the substrate, and precursor gases individually and in combination that is not explored extensively before.

DEDICATION

To my parents

ACKNOWLEDGEMENTS

I am wholeheartedly grateful to my advisor Dr. Terry Xu for her continuous guidance, support, and encouragement throughout my research and study in the doctoral program. I am truly indebted to her for giving me ample opportunities to acquire knowledge and skills which would definitely be beneficial for my future career.

I would like to express my gratitude to Dr. Haitao Zhang, Dr. Youxing Chen, and Dr. Thomas Schmedake for serving on my dissertation committee, and for their valuable time and help. Additionally, I am grateful to Dr. Zhang and Dr. Chen for their help in solving many issues with the equipment, and for guidance to prepare cross-sectional samples. I owe thanks to Dr. Deyu Li and his students for providing me with the opportunities to work on collaborative projects.

I am also thankful to my previous groupmate Dr. Siang Yee Chang for teaching me the operation of different equipment, and maintenance of the lab and providing me with other valuable advice necessary for a new Ph.D. student.

I gratefully acknowledge the financial support provided by UNC Charlotte as GASP and Graduate Student Summer Fellowship. I am thankful to the department of Mechanical Engineering for supporting me and giving me the opportunity to teach the lab course.

I would like to thank my friends Syeda Lammim Ahad and Ruslan Brilenkov to help me with python programming and Latex. I am extremely fortunate to have Manzila and Lammim as my kindred spirits who keep inspiring me through their creativity, passion, and humor. I cannot thank enough all my friends (Maitraye, Sunandita, Subhasree, Farida, Madhumita, Liuqing, Zhuo, Pedram, Pavitra, Sujithra, Mehnaz, Nuren, Mehrab, Liza apu, and Shohan bhaiya) in the US and my home country for always being there, supporting me during my difficult time, and sharing good times with me. Lastly, I am most grateful to my parents, brother, and other family members for always loving, cherishing, and believing in me.

TABLE OF CONTENTS

LIST OF TABLES	xii
LIST OF FIGURES	xiii
LIST OF ABBREVIATIONS	xvii
CHAPTER 1: INTRODUCTION	1
1.1. Overview of 1D Nanostructures	1
1.1.1. Growth of Nanostructures	3
1.1.2. Properties and Applications of 1D Nanostructures	12
1.1.3. Study of VLS Growth Mechanism	16
1.2. Summary	24
CHAPTER 2: EXPERIMENTAL METHODS AND TOOLS	27
2.1. Electron Microscopy	27
2.1.1. Scanning Electron Microscope (SEM)	29
2.1.2. Transmission Electron Microscopy (TEM)	34
2.2. Energy Dispersive X-ray Spectroscopy (EDS)	43
2.3. Preparation of Cross-Sectional Sample	46
2.3.1. Cutting and Bonding	47
2.3.2. Mechanical Thinning by Grinding and Polishing	48
2.3.3. Dimple Grinding	50
2.3.4. Precision Ion Milling	52
2.3.5. Challenges on Preparation of Nanowires-on-Substrate Cross-Sectional Sample	54
2.4. Software Tools	55

CHAPTER 3: MATERIALS CHARACTERIZATION OF NIOBIUM SELENIDE NANOWIRES	57
3.1. Background Information	57
3.1.1. Significance of Niobium Selenide (NbSe_3) for Distinct Signatures of Electron-Phonon Coupling	57
3.1.2. Crystal Structure of Niobium Selenide (NbSe_3)	58
3.1.3. Preparation of NbSe_3 Nanowires	61
3.1.4. "Routine" Materials Characterization and Understanding of Electron-Phonon Interaction	62
3.1.5. Anomalous Thermal Transport in Ultrathin Nanowires	65
3.2. Determination of Lattice Constants of NbSe_3 Crystal	67
3.2.1. Solving Planar Spacing Equation for NbSe_3 Lattice	68
3.2.2. The Need of Results from Multiple Zones and Challenges in Tilting	68
3.2.3. Construction and Utilization of DP Roadmap	71
3.2.4. Results	73
3.3. Summary	76
CHAPTER 4: GROWTH MECHANISM OF BORON CARBIDE NANOWIRES	78
4.1. Research Status on Boron-Based 1D Structures	78
4.1.1. Bulk Boron and Boron Rich Materials	78
4.1.2. Bulk Boron Carbide Structure and Properties	80
4.1.3. Current Status of Boron Carbide Nanowires	83
4.2. Experimental Results from Cross-Sectional Examination	90
4.2.1. Reference Cross-sectional Sample	91

	xi
4.2.2. Effect of Annealing	95
4.2.3. Catalyst Formation and Effect of Temperature	97
4.2.4. Effect of Diborane	108
4.2.5. Effect of Methane	110
4.2.6. Boron Carbide Nanostructures Without Catalyst	112
4.2.7. Cross-sectional Examination of Nanowires	114
4.2.8. Effect of Reaction Time	117
4.2.9. Summary and Hypothesis of Growth Mechanism	118
CHAPTER 5: CONCLUSIONS	124
5.1. Conclusions	124
5.2. Future Works	125
REFERENCES	127

LIST OF TABLES

TABLE 1.1: Comparison between VLS and VSS growth mechanisms	7
TABLE 1.2: Comparison table for different TEM based techniques to explore growth mechanisms	24
TABLE 4.1: List of experimental conditions of varying reactants for cross-sectional sample preparation	91
TABLE 4.2: EDS results from different locations from a sample obtained in condition 2	107
TABLE 4.3: List of experimental conditions of varying reaction time for cross-sectional sample preparation	117

LIST OF FIGURES

FIGURE 1.1: Bottom-up synthesis routes of 1D nanowires.	4
FIGURE 1.2: Schematic diagram of VLS mechanism.	5
FIGURE 1.3: Schematic diagram of chemical vapor deposition (CVD) method	8
FIGURE 1.4: Schematic diagram of chemical vapor transport (CVT) method	9
FIGURE 1.5: Examples of TEM images from routine examinations of different types of NWs	17
FIGURE 1.6: Cross-sectional TEM images of plan-view of Si NWs grown along different growth directions	19
FIGURE 1.7: Cross-sectional TEM images of side-view of GaP NW, NW-substrate interface and catalyst-substrate interface	20
FIGURE 1.8: Observation of in-situ nanowire growth	22
FIGURE 2.1: Interaction of electron with a thin specimen and generated signals	29
FIGURE 2.2: Schematic diagram of SEM showing major components and ray diagram for image formation	30
FIGURE 2.3: Schematic diagram of an electromagnetic lens	31
FIGURE 2.4: Schematic drawing of interaction volume	32
FIGURE 2.5: Schematic diagram of TEM	35
FIGURE 2.6: Imaging and diffraction mode in TEM	36
FIGURE 2.7: Bright field and Darkfield imaging	37
FIGURE 2.8: Phase contrast imaging with many beams	38
FIGURE 2.9: Schematic drawing of electron ray paths for the derivation of camera constant equation	39

FIGURE 2.10: Example of a DP from a Si sample, and calibration of DP from standard TEM calibration sample	42
FIGURE 2.11: Generation of X-ray	44
FIGURE 2.12: Si(Li) detector	45
FIGURE 2.13: Cutting and bonding	48
FIGURE 2.14: Mechanical grinding and polishing	49
FIGURE 2.15: Dimple grinding	52
FIGURE 2.16: Ion milling	54
FIGURE 2.17: Schematic diagram showing m-bond coated nanowires-on-substrate and comparison with substrate without nanowires	55
FIGURE 3.1: Simulated crystal structure of NbSe ₃	59
FIGURE 3.2: Monoclinic crystal structure of NbSe ₃ viewed along <i>b</i> axis	60
FIGURE 3.3: TEM results of a representative NbSe ₃ nanowire	63
FIGURE 3.4: Electrical and thermal measurements data, and modeling results with respect to temperature to show the effect of e-ph interaction in NbSe ₃ nanowires	64
FIGURE 3.5: Superdiffusive transport of 1D phonons in NbSe ₃ nanowires based on the dependence of thermal conductivity on size and temperature	66
FIGURE 3.6: Schematic drawing of monoclinic crystal structure including vector directions to show three zone axes and their corresponding simulated DPs	70
FIGURE 3.7: A DP roadmap for NbSe ₃ monoclinic crystal structure. It consists of simulated DPs from some common low index zone axes obtained during TEM examination	72

FIGURE 3.8: A schematic diagram for NbSe ₃ monoclinic crystal structure consisting of two unit cells. Three vector directions are shown to indicate three zone axes from a common origin (o), and angles between them are shown to visualize the angles projected on the roadmap in Figure 3.7. As they are not in the same plane, it is not straightforward to calculate the angles based on the roadmap	73
FIGURE 3.9: Four lattice constants with the change of width measured from TEM images	74
FIGURE 3.10: Elastic stiffening in NbSe ₃ nanowires	76
FIGURE 4.1: (a) B ₁₂ icosahedron labeled from 1 to 6 for the polar atoms and 7 to 12 for the equatorial atoms, and (b) crystal structure of α -rhombohedral boron showing eight B ₁₂ icosahedra in the rhombohedral unit cell and red triangles denoting three center bonds	79
FIGURE 4.2: Crystal structure of boron carbide and boron-carbon phase diagram	81
FIGURE 4.3: Schematic Diagram of the LPCVD system	84
FIGURE 4.4: Schematic Diagram of the reactor chamber showing temperature profile, position of three substrates at three temperatures T1, T2 and T3 and concentration profiles of B ₂ H ₆ and CH ₄ [1]	85
FIGURE 4.5: Schematic diagram of the substrate showing regions of interest, SEM image of as-synthesized NWs, and HRTEM images of TF and AF NWs	87
FIGURE 4.6: Dependence of thermal conductivity on diameter, carbon concentration, and fault orientation	88
FIGURE 4.7: Different types of kinked nanowires and thermal conductivity	89
FIGURE 4.8: Cross-sectional images from reference sample	92
FIGURE 4.9: EDX result from reference sample	94
FIGURE 4.10: Cross-sectional images from condition 1	96
FIGURE 4.11: Cross-sectional TEM and top view SEM images from Condition 2	98

FIGURE 4.12: Histograms plotted from cross-sectional TEM and top view SEM images from Condition 2	100
FIGURE 4.13: Annealing of 5 nm Ni film on SiO ₂ layer at different temperatures for 1 hour	103
FIGURE 4.14: Schematic diagram of void formation in the SiO ₂ layer	105
FIGURE 4.15: Temperature effect in the catalyst formation in the different regions of the reaction chamber	106
FIGURE 4.16: Cross-sectional TEM image of condition 2 from 15-18 mm away from low T end showing locations of acquired EDX spectra	107
FIGURE 4.17: cross-sectional TEM and top-view SEM images from condition 3	109
FIGURE 4.18: cross-sectional TEM and top-view SEM images from condition 4	111
FIGURE 4.19: cross-sectional TEM and top-view SEM images from condition 5	113
FIGURE 4.20: Cross-sectional high magnification TEM images from condition 5	114
FIGURE 4.21: Cross-sectional TEM and top-view SEM images from condition 6	115
FIGURE 4.22: Cross-sectional high magnification TEM images from condition 6	116
FIGURE 4.23: Cross-sectional TEM images and top-view SEM images from two conditions of varying reaction time	118
FIGURE 4.24: Summary of all conditions from the relatively low-temperature region	119
FIGURE 4.25: Summary of all conditions from the relatively high-temperature region	121

LIST OF ABBREVIATIONS

0D	zero-dimensional
1D	one-dimensional
2D	two-dimensional
3D	three-dimensional
AAO	anodized aluminum oxide
AEM	analytical electron microscope
AFM	atomic force microscopy
APCVD	atmospheric pressure chemical vapor deposition
BF	bright field
BFP	back focal plane
BSE	backscattered electron
CCD	charge-coupled device
CIF	crystallographic information file
CVD	chemical vapor deposition
DF	dark field
DP	diffraction pattern
DSSCs	dye sensitized solar cells
EDX	electron dispersive x-ray spectroscopy
EELS	electron energy loss spectroscopy

FEG field emission gun

FET field effect transistor

HAADF high angle annular dark field

HRTEM high resolution transmission electron microscopy

ICDD international centre for diffraction data

LaB₆ lanthanum hexaboride

LPCVD low pressure chemical vapor deposition

MFP mean free path

MOVPE metal-organic vapor phase epitaxy

NW nanowire

NWFET nanowire field effect transistor

OAG oxide assisted growth

p-i-n p-type/intrinsic/n-type

PCE power conversion efficiency

PDF powder diffraction file

PECVD plasma enhanced chemical vapor deposition

PIPS precision ion polishing system

PMT photomultiplier tube

SA-MOVPE selective area metal-organic vapor phase epitaxy

SADP selected area diffraction pattern

SAXS small angle x-ray scattering

SE secondary electron

SEM scanning electron microscope

SFSL supercritical fluid-liquid-solid

SFSS supercritical fluid-solid-solid

SiNW silicon nanowire

SLS solution-liquid-solid

TEM transmission electron microscope

UHVCVD ultrahigh vacuum pressure chemical vapor deposition

VLM visible light microscope

VLS vapor-liquid-solid

VSS vapor-solid-solid

XRD x-ray diffraction

CHAPTER 1: INTRODUCTION

The main objective of this dissertation work is to explore the structure-property relationship and growth mechanism of one-dimensional (1D) nanostructures i.e., nanowires. Recent advancements in synthesis, characterization of structure, and properties of different types of nanowires compel us to obtain more understanding of structure-property correlation, and also to gain control over the rational synthesis of specific types of nanowires. In this chapter, background information about synthesis, properties, and applications, and the study of the growth mechanism of 1D nanostructures are discussed.

1.1 Overview of 1D Nanostructures

Nanomaterials are defined by the class of materials that contain at least one dimension between 1-100 nm [2] and change properties with size reduction [3]. Based on dimensionality, nanostructures can be classified as zero-dimensional (0D), one-dimensional (1D), two-dimensional (2D), and three-dimensional (3D) nanostructures [2]. Nanomaterials with all the external dimensions in the nanoscale such as quantum dots are termed 0D nanomaterials. 1D nanomaterials have one external dimension outside the nanoscale and the other two in the nanoscale e.g., nanowires. Similarly, nanomaterials with only one external dimension in the nanoscale are defined as 2D nanomaterials such as thin films. The last category, 3D nanostructured materials do not have any external dimension in the nanoscale region but usually have multiple phases where at least one of the phases contains the nanoscale feature, for example, nanocomposites [4].

Much of the research interest in nanostructures has grown due to their unique prop-

erties and potential applications compared to their bulk structures [5]. The ability to synthesize materials in the nanometer range has opened vast opportunities to investigate fundamental concepts in physical sciences and engineering [2, 5]. Due to the unique one dimensionality, nanostructures such as wires, rods, belts, and tubes are recognized as the ideal systems to investigate the relationships between dimensionality, size, and functional properties of the nanostructured materials [3]. Inspired by the Vapor-Liquid-Solid (VLS) mechanism for the growth of silicon whiskers proposed by R.S. Wagner in the 1960s [6], several researchers started synthesis and characterization of 1D nanostructures including nanowires or nanowhiskers of elemental semiconductors, oxides, carbides, and III-V compounds in the early 1990s [7]. In the following three decades, intensive research has been performed and nanowire research has become an active research area within the nanoscience community with new opportunities and potential applications [8]. For example, nanowires can be used as the interconnects and building blocks for the fabrication of electronic and photonic, biomedical, and energy conversion and storage devices [5, 8]. Also, nanowire growth has been found to have the natural mechanism that enables lattice-strain-free epitaxial growth of III-V nanowires on group IV substrates which has been an issue in the case of 2D thin films technology. Usually, lattice and thermal expansion mismatch between III-V materials with group IV substrates generate lattice strain, and antiphase or twin boundaries in the interface, that can be avoided during nanowire growth due to reduced contact area between nanowire and substrate [8, 9]. Despite the current progress and development, the synthesis of 1D nanostructures in large quantities, rapidly, at reasonably low costs, and from diversified materials require further endeavors [5]. The following sections will discuss different synthesis methods, properties, applications, and the study of the growth mechanism of 1D nanostructures from the current research advancements.

1.1.1 Growth of Nanostructures

Two basic fabrication methods for all types of nanomaterials are top-down and bottom-up approaches. The top-down approach refers to the fabrication of nanostructures by sculpting or etching from bulk material, and the bottom-up approach employs the growth of nanostructures from atomic and molecular scale components. The top-down approach, for example, optical lithography has been used successfully in the manufacturing of integrated circuits for decades. However, this approach can be limiting based on scalability and cost such as fabricating NW-based field effect transistor (FET) devices. The bottom-up approach can be employed to fabricate nanomaterials by overcoming the limitations of conventional top-down approaches. In addition, a wide range of nanostructures can be synthesized from all transition metals, noble metals, and semiconductors in large quantities by taking different synthetic routes [10].

In this section, we will limit our discussion to bottom-up synthesis methods of 1D nanowires. In a comprehensive review by Dasgupta et.al., these methods were classified into the following categories: catalyst/ metal-nanoparticle mediated, direct deposition, template-directed and oriented-attachment methods. Catalyst-mediated methods can be realized by two synthesis routes, i.e., gas phase and solution phase synthesis. Those synthesis routes were affiliated with five growth models/mechanisms: Vapor-Liquid-Solid (VLS) and Vapor-Solid-Solid (VSS), Solution-Liquid-Solid (SLS), Supercritical Fluid-Liquid-solid (SFLS) and Supercritical Fluid-Solid-Solid (SFSS) methods [11]. The categorized methods, routes, and growth mechanisms are presented as a chart in Figure 1.1 and discussed in the following subsections.

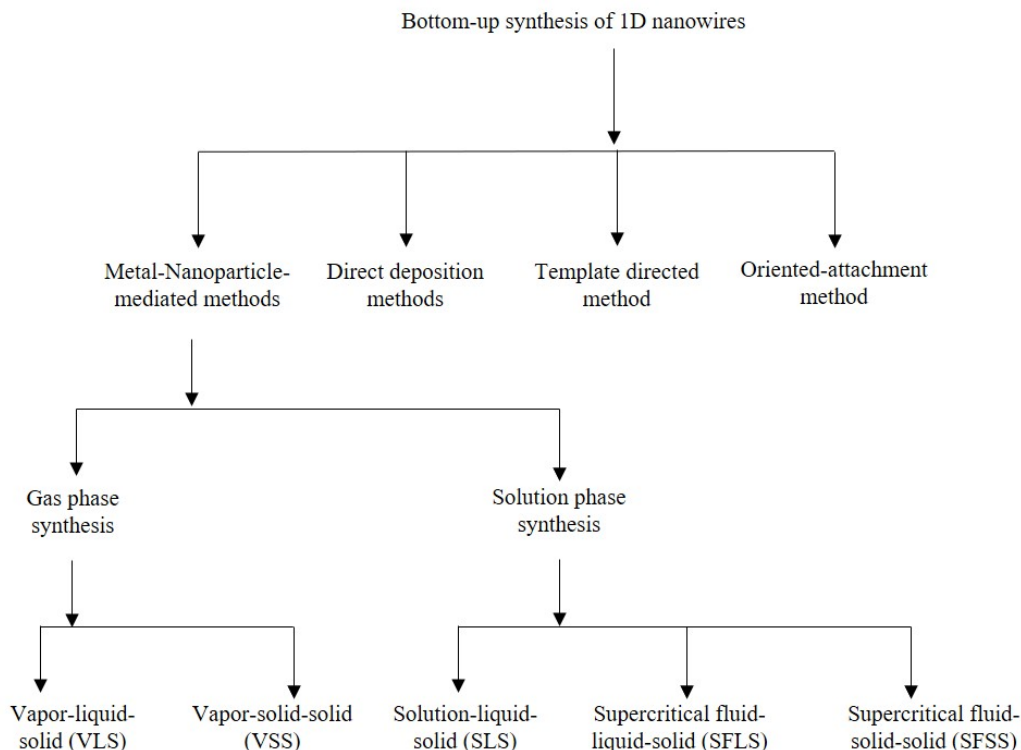


Figure 1.1: A detailed categorization of bottom-up synthesis methods, routes and growth models of 1D nanowires by Dasgupta et. al. [11]

1.1.1.1 Catalyst Mediated Methods and the Associated Growth Mechanisms

As briefly mentioned above, while synthesizing 1D nanostructures, the catalyst-mediated method can be acquired by two synthesis routes and five associated growth mechanisms. In this subsection, we will focus our discussion mainly on the gas/vapor phase synthesis route and the corresponding growth models (i.e., VLS and VSS mechanisms) along with a short discussion of the solution phase route and the related mechanisms.

Gas Phase Synthesis, and VLS and VSS Mechanisms

Gas phase synthesis involves 1D nanostructures to grow from gas/vapor phase reactants and is one of the most common and versatile routes. Among two growth models of this route, Vapor-Liquid-Solid (VLS) mechanism was originally developed by Wagner and Ellis in the 1960s [6]. This growth mechanism can be explained by

using a schematic diagram presented in Figure 1.2(a). In this mechanism, nanowire-forming constituent materials (which can be referred to as precursors) are gasified by physical/chemical vaporization processes [5]. After vaporization, an impurity metal or alloy of low freezing temperature is added to the system, which acts as a catalyst and forms nanosized liquid droplets. The gaseous reactants deposit preferably in the liquid droplets of the catalyst, and single crystalline rods and wires form through nucleation and growth in the interface of the substrate and liquid droplets [6]. These droplets control the lateral growth limit of nanowires by acting as soft templates [5].

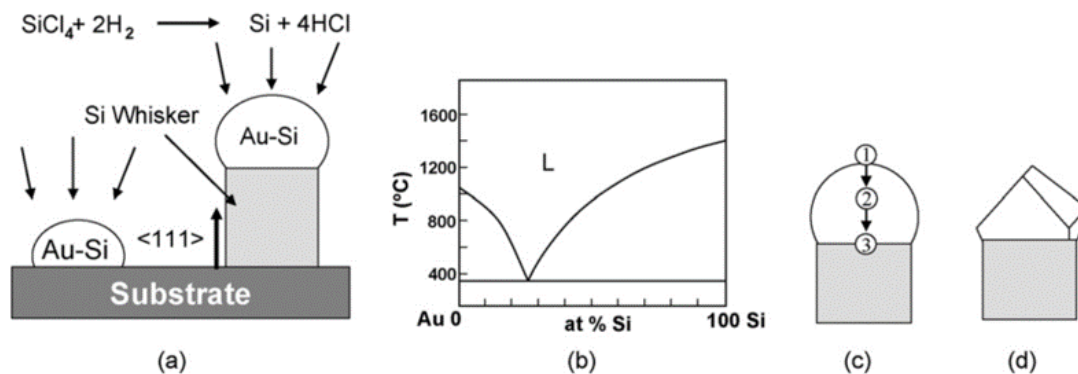


Figure 1.2: Schematic diagram of VLS mechanism [12]

There are several issues with the VLS growth model. First, according to the conventional VLS model, assuming catalyst droplets to be stable throughout the growth period, droplet size and growth time can regulate the diameter and length of nanowires independently [11]. But it has been seen that, in the carefully controlled growth environment, catalyst atoms can migrate from one droplet to another, and to the nanowire and substrate surface. Thus, the diameter of the droplets changes, affecting the diameter, sidewalls, and length of the nanowires during the growth [13]. Second, catalyst atoms can be incorporated into nanowire lattice which might change the properties of the nanowires [11]. Another major limitation of the VLS mechanism is that it cannot be employed to grow metal nanowires [5].

Also, the above process requires the availability of a solvent that forms eutectic

compounds with the target material. So far, this requirement has been fulfilled by using the equilibrium phase diagram [5]. Like the VLS mechanism, nanowires can grow with the assistance of solid-state catalyst nanoparticles, known as the VSS growth mechanism. In this mechanism, metal and semiconductors can react in the solid state to yield crystalline compound nanoparticles which can act as catalysts for vapor phase precursors. This mechanism is much similar to the VLS mechanism in terms of nucleation and growth. One disadvantage of the VSS mechanism is that in some materials systems, the nanowire growth rate is one/two orders of magnitude lower than the VLS mechanism due to the low solubility of semiconductor elements in the solid-state catalyst nanoparticles. However, the VSS mechanism is advantageous when the eutectic temperature between metal and semiconductor is very high. Nanowires can be grown in this mechanism at a lower growth temperature which is more compatible with the fabrication of nanowire-based devices [11] as compared to the VLS mechanism. A comparison between VLS and VSS mechanisms is presented in Table1.1.

Table 1.1: Comparison between VLS and VSS growth mechanisms [11, 14, 15, 16].

Criteria	VLS	VSS
Catalyst state	Liquid	Solid
Growth temperature	Eutectic temperature of catalyst and precursor	NWs can grow below eutectic temperature
Advantages	<ul style="list-style-type: none"> • It can be used for a wider range of materials than VSS • Higher growth rate than VSS mode based on the specific chemical system, precursor decomposition, and diffusion 	<ul style="list-style-type: none"> • NWs can be grown at lower temperatures in the material system with high eutectic temperature • Compositional control can be achieved in atomic scale
Disadvantages	<ul style="list-style-type: none"> • Liquid catalyst acts as a reservoir of precursor materials, inhibiting compositional control in the atomic scale for heterostructure nanowires • Higher growth temperature and incompatibility with device fabrication in some cases 	<ul style="list-style-type: none"> • In some materials systems, VSS growth rate is one or two orders of magnitude lower than VLS • Less catalytic activity due to solid state
Representative materials	Elemental semiconductor, III-V, and II-VI, oxide, carbide, and nitride nanowires	Ge, Si, GaAs, and InAs nanowires

Vapor phase synthesis is carried out in different physical and chemical systems/processes such as laser ablation, thermal evaporation, arc discharge, and chemical vapor deposition [5]. Among them, chemical vapor deposition (CVD) is one of the most widely used processes to synthesize high-quality low-dimensional nanostructures including nanowires [17, 18, 19, 20]. This method involves gas-phase precursors, surface chemical reactions on or near the heated substrate, and the formation of solid phase nanostructures [17]. A simplified schematic diagram [17] is presented in Figure 1.3 which shows the decomposition of precursor material into molecules/ atoms carried by a neutral carrier gas and deposition on the substrate uniformly. Heat, plasma, or other methods are used to activate the decomposition of precursors and reaction [21]. CVD processes have many variants depending on the pressure, reactor type, or precursor materials. Based on the pressure inside the reactor, there can be three types of CVD methods, (i) atmospheric pressure CVD (APCVD) that uses atmospheric pressure (760 torrs), (ii) low-pressure CVD (LPCVD) using pressure in the $\approx 10^{-3}$ torr range, (iii) ultrahigh vacuum CVD (UHVCVD) using pressure in the $\approx 10^{-8}$ torr [17, 22].

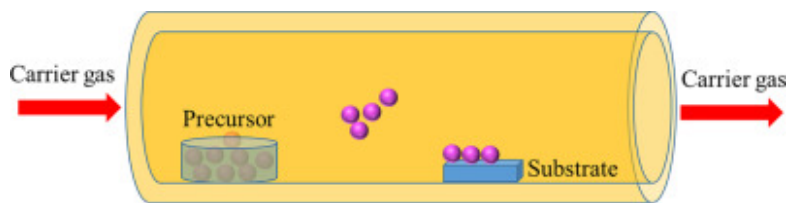


Figure 1.3: Schematic diagram of chemical vapor deposition (CVD) method [17].

For this dissertation, two types of 1D NWs have been studied. Boron carbide NWs were prepared by LPCVD technique (discussion can be found in more detail in Chapter 4), and niobium selenide bulk crystal was prepared by chemical vapor transport (CVT) process and NWs were obtained by ultrasonic cleaving of the bulk crystal (refer to Chapter 3). CVT process involves volatilization and transportation of the reactants with the help of a transport agent from one zone to the other zone

in the reaction chamber (schematic diagram in Figure 1.4). A temperature gradient is created between the two zones. Reactants are volatilized in the hot zone T_2 and transported to the cold zone T_1 where crystallization occurs [23].

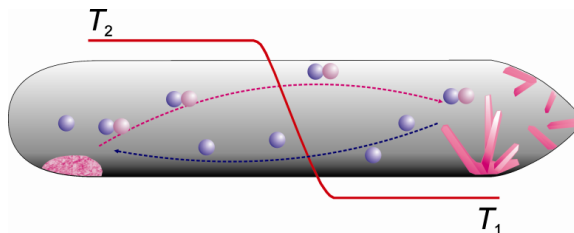


Figure 1.4: Schematic diagram of chemical vapor transport (CVT) method [23].

Solution Phase Synthesis and the Related Growth Mechanisms

Analogous to the vapor phase route, solution phase synthesis routes have also been developed to generate colloidal semiconductor nanowires. In a typical solution-liquid-solid (SLS) mechanism, a metal with a low melting point is used as a catalyst and organometallic precursors/surfactants are used to generate whiskers or filaments of the desired material. This organic surfactant decomposes and forms a complex in several steps and finally gets eliminated to form a non-molecular unit of the nanowire. Using this method, the diameter of the nanowire can be controlled in the quantum confinement regime, as surfactant molecules protect the surface and control the radial growth of colloidal nanowires. Also, nanowires can be generated at a much lower temperature than the VLS method. But obtaining control over crystal structure and growth orientation of nanowires is a challenge in this method [11]. In solution phase growth, nanowires can also be grown using supercritical fluid as solvents, known as supercritical fluid-liquid-solid (SFLS) [5]. In this mode, the growth temperature is higher than that of SLS mode [11] which enables the dissolution of organic solvent and promotes crystallization of desired material [5]. Transition metal nanoparticles can be used as seeds for nanowire growth due to supercritical conditions. Additionally, reaction pressure can control the growth orientation of nanowires [5]. Like VSS

growth mode, nanowire has been seen growing at a lower temperature than metal-semiconductor eutectic temperature, hence in the solid state of catalyst nanoparticles, which can be termed as supercritical fluid-solid-solid (SFSS) mode [11].

1.1.1.2 Direct Deposition Method

Catalytic-assisted growth can induce impurities that can significantly change nanowire properties. The problem can be overcome by self-catalyzed growth, but that is limited for some semiconductor nanowires growth [11]. In some cases, nanowires can be grown via direct deposition methods such as selective growth of GaAs nanowires by metal-organic vapor phase epitaxy (MOVPE). Ikejiri et al. conducted growth of GaAs in an SA-MOVPE method and showed that under certain growth conditions, NW growth occurred depending on the low index facet formation in the absence of catalytic metal or oxide [24]. Nanowires can also be grown directly by using dislocation-driven mechanisms. For example, ZnO nanowire arrays have been grown directly from heteroepitaxial GaN with deliberately generated surface screw dislocations. Nanowires grown using dislocation-driven mechanisms have central continuous dislocation lines [11].

1.1.1.3 Template Directed Method

Soft templates such as polymer-like complex chains and bio templates can be used to grow ultra-thin metal nanowires and single crystalline metal sulfide nanowires. Ultra-thin Au nanowires were synthesized from polymer-like complex chains that formed one-dimensional Au^I containing channels that reduced to Au nanowires as thin as 1.6 nm. In the case of bio templates, nucleation and growth of densely packed nanocrystals occur at the template surface. At high temperatures, those templates can be completely removed and single crystalline nanowires form from the merging of the oriented nanocrystals. Porous templates such as anodized aluminum oxide (AAO) that contain cylindrical nanochannels are commonly used as a hard template

to grow hierarchical nanowires. Hierarchical branched channels can be produced by applying multistep anodization using controlled voltage and that templates can be used to fabricate nanowires of well-controlled branched structures by electrochemical deposition (such as). Mesoporous silica with a hexagonal array of nanopores can also be used as a hard template to fabricate nanowires of such morphology that cannot be achieved by other methods [11].

1.1.1.4 Oriented Attachment Method

Another method to synthesize nanowires with controlled morphology and dimensions is the oriented attachment method. In this method, crystalline colloidal particles dispersed in a liquid phase or suspension align their atomic lattices and form a single crystal. Then, two aligned crystals attach to each other by epitaxy of two specific facets and form crystalline 1D, 2D or 3D nanostructures with specific geometries. The attachment decreases the surface energy and lowers the total free energy of the system. This method can be used both for suspensions of charge-stabilized crystals in water, and ligand-capped nanocrystals in nonpolar organic solvents [25]. Tang et. al. demonstrated the growth of wurtzite CdTe nanowires from the oriented attachment of zinc blende CdTe nanocrystals upon controlled removal of ligands from the surface of the nanocrystals and aging in darkness. Removal of ligands invokes the dipole-dipole attraction that initiates linear aggregation of nanoparticles. Due to the intrinsically anisotropic nature of the wurtzite (hexagonal) lattice, nanocrystals of the zinc blende structure reorganize to match the crystal symmetry and geometry of the 1D structure. The low activation energy of the phase transition facilitates the process. This method can be extended to other types of semiconductors, and high-quality nanowires with uniform diameters and high aspect ratios can be prepared [26].

In summary, although other methods are available to grow nanowires successfully, the VLS mechanism is most extensively explored and can be used to process any bulk materials into 1D nanostructures by controlling the supersaturation level in the

vapor phase. Also, it is a widely adopted technique to grow semiconductor nanowires with single crystalline structures. In this work, we will explore the growth mechanism following the VLS model.

1.1.2 Properties and Applications of 1D Nanostructures

As briefly mentioned before, 1D nanostructures have unique characteristics such as anisotropy, large surface area, and potential quantum confinement effect that render their superior properties and promising applications in various fields such as nanoelectronics, photonics, chemical and mechanical sensing, optoelectronics, energy generation, and storage devices. To date, many reviews are available covering properties and applications of semiconductor nanowires [5, 27, 11, 28, 29]. A few of the notable applications will be discussed here briefly.

1.1.2.1 Nanowire Electronics

Semiconductor nanowires are promising for complex functional devices and nanoscale integrated circuits due to their predictable electrical properties and controllable synthesis [7, 29]. Lieber group first demonstrated rectifying electron transport by using diode structures with crossed p-type and n-type nanowires that are comparable to planar p-n junctions. Such crossed p-n junctions are highly reproducible [30] and can be used for constructing nanoLEDs by crossing p-type SiNW with n-type III-V and II-VI NWs (such as GaN, CdS, CdSe and InP NWs) as demonstrated by Huang et al. [31]. Similarly, a field effect transistor (FET) can be developed by using crossed nanowires. In this case, one nanowire can be used as an active semiconducting channel and the other one as the gate dielectric [32]. These NWFET devices can be developed with well-controlled width and length of the nanoscale channel, and gate dielectric thickness. As a result, improved transistor properties (e.g., speed, gain) and reduced power dissipation can be obtained [29]. By using the bottom-up approach, these cross-nanowire FETs and p-n diodes can be assembled into logic circuits such

as OR, AND, and NOR gates [32]. Similarly, using these logic gates, complex logic circuits can be built using nanowires as interconnects that eliminate additional wiring [29].

NWFET devices can be efficiently used as biological and chemical sensors because a small change in the gate signal in FET can significantly alter drain-source current [33]. NWs can be modified or functionalized with a target-specific molecular receptor. In the solution, the target species will bind or link with the receptor, resulting in a change in the surface charge that can be detected as a direct change in conductance in the device [27]. Thus, NWFETs can be used to detect trace molecules with high sensitivity and selectivity [34]. Despite the availability of different types of nanowires, Si and its derivatives are still the most widely sought for improved sensing performance due to their advanced synthesis and nanofabrication techniques [35]. Lieber group first functionalized Si NWs with amine and oxide to use them as nanoscale pH sensors. Also, they demonstrated biotin- and antigen-modified SiNWs to detect bacterial protein streptavidin and antibody binding respectively [34]. This work led to the development of many applications such as the detection of DNA sequences, different types of protein cancer markers [27] as well as monitoring and probing of intra and extracellular activities as bio-interfaces [33].

1.1.2.2 Nanowires in Energy Conversion Applications

Alongside nanowire electronics, nanowire photonics also has significant growth where nanowires demonstrate optical properties in the subwavelength region and can be used as photonic building blocks. These developments also led to advancements in other areas such as nanowire photovoltaics [7].

Having the confinement effect due to nanoscale diameter, nanowires have the ability to electron transport along their long axis. That feature enables nanowires to be used for energy conversion applications such as in the construction of solar cells [36]. Conventional Si-based solar cells suffer from the disadvantage of a low absorp-

tion coefficient of Si in the visible and near-infrared regions of the spectrum. As the majority of the sunlight is in this region, Si solar cells are required to be thick to absorb much of the incident photons. Also, solar cell efficiency is limited by the minority carrier diffusion length, which is affected by various recombination mechanisms [36, 37]. An optimal design was demonstrated by Tian et al. by fabricating radial heterostructures of p-type/intrinsic/n-type (p-i-n) Si solar cells that provided the power conversion efficiency (PCE) of 3.4%. Such structures are advantageous in terms of carrier separation along the radial direction instead of the axial direction and thus the decrease of the carrier collection distance resulting in higher carrier collection efficiency without large bulk recombination [38].

III-V materials such as GaAs and InP are excellent candidates for nanowire solar cells due to their direct band gap energy and high absorption coefficient [39]. Different design optimizations such as radial or axial p-n and p-i-n junctions have been explored in the past decade for both single nanowire and nanowire array solar cells. Maximum PCE of 10.5% could be obtained for a single horizontal InP nanowire solar cell of axial p-i-n junction after surface passivation with SiN_x layer [40]. However, better efficiency (15.3%) could be obtained for GaAs nanowire array solar cells [41]. All these results present NW-based solar cells as promising candidates in terms of low cost, higher efficiency, and reduced material consumption. However, further endeavors are required for the optimization and control of design, materials growth, and device fabrication for viable solar cell applications [39, 40].

Nanowire arrays have also been used to improve the performance of excitonic solar cells such as dye-sensitized solar cells (DSSCs). Excitonic solar cells are inexpensive because of the use of polymers or dye molecules and have the capability of large-scale solar energy conversion. Law et al. first fabricated DSSCs using ZnO nanowire arrays as photoanodes and reported PCE of 1.5% [42]. Zi et al. compared different morphologies of ZnO photoanodes for DSSCs and found enhanced performance for ZnO

nanowire array compared to film and nanosheet. Because the nanowire array enables improved dye absorption and provides channels for faster collection of the carriers that results in more photon utilization [43]. Despite having better electron transport properties, the overall efficiency of NW-based DSSCs is lower than nanoparticle-based cells because of the smaller surface area of the nanowire array [37]. To further improve performance, multidimensional and hierarchically branched nanowires can be used as reported for the DSSCs made with densely branched TiO₂ nanowire arrays. Densely packed branches in all directions increased surface area and effective photon absorption, and efficiency improved up to 6.2%) [44].

1.1.2.3 The Importance of Establishing Structure-Property Relationships

So far, we have discussed and provided examples of how different types of NWs can be used to improve efficiency in different applications such as electronics and energy conversion applications. However, to fully utilize the potential of the NWs for the development of nanoscale devices, one of the roadblocks remains to be able to correlate the properties with the structurally well-understood NWs. Structural parameters such as lattice constants, phase purity, defects, and lattice strains have impacts on different properties including piezoelectric and photoluminescence and transport properties [45, 46]. For example, electrical conductance behaviors of metal NWs had been controversial, due to the difficulty of separating the structural and electronic effects during NW stretching measurement experiments. Rodrigues et al. demonstrated the dynamic structural evolution of metallic Au, Ag, and Pt NWs due to elongation. Conductance was correlated to the more frequently occurred rodlike [110] NWs with the reduced number of structures (determined by surface energy) [47, 48]. This emphasizes the need of correlating the properties to the structural parameters to remove the gaps in the knowledge and for wider application of the NWs in the devices.

1.1.3 Study of VLS Growth Mechanism

Substantial research has been conducted to investigate the growth mechanism of 1D NWs in the past two decades. NWs synthesized in the presence of a catalyst or in the case of self-catalyzed NWs, the catalyst can be observed on the tip of the NWs and, they are explained based on the VLS growth model [49, 50]. But growth mechanism is not fully understood yet to obtain the controlled synthesis of NWs with specific morphology, size, and structures. Qualitative and quantitative studies of the growth mechanism of the NWs have been conducted by using different analytical techniques such as in-situ and ex-situ electron microscopy (scanning electron microscopy (SEM) and transmission electron microscopy (TEM)), energy dispersive X-ray spectroscopy (EDX), electron energy loss spectroscopy (EELS), atomic force microscopy (AFM), small angle x-ray scattering (SAXS), X-ray diffraction (XRD) and Raman spectroscopy. Electron microscopy is the most used and powerful technique among them. In this subsection, our focus is to explore different TEM-based techniques, for example, 'routine' TEM examination, in-situ growth, and cross-sectional examination that have been performed for the growth mechanism study of different types of NWs.

1.1.3.1 Routine Examination

Routine examination refers to the regular TEM examination of individual NW by directly transferring it from the growth substrate to the TEM grid. High-resolution TEM (HRTEM) images and selected area diffraction patterns (SADP) can be used to determine growth direction, phase structure, and defects. Also, the examination of catalyst structure, shape, and composition as well as the NW-catalyst interface provides useful information. Some examples are presented in Figure 1.5. Figure 1.5 (a) is presented to show an InAs NW with the Au catalyst particle on the top of the NW. NW-catalyst interface is zoomed in the inset and shows a boundary layer of δ where diffusion and supersaturation of the growth species in the catalyst occur.

Analysis of the diffraction pattern in the NW confirms the wurtzite structure and EDX analysis is used to determine the composition of the catalyst particle which is an alloy of Au and In (As or Si were not detected in the catalyst) [51]. Another example of InAs NW with Au catalyst is shown in Figure 1.5 (b). The corresponding diffraction pattern (in the inset) in the NW shows the zone axis of $\langle 1\bar{2}10 \rangle$. From the HRTEM image, the catalyst has a well-defined hemispherical shape which indicates a liquid catalyst phase during NW growth. For NW growth from solid state catalyst, results in faceted interface confirmed from in situ TEM examination [52].

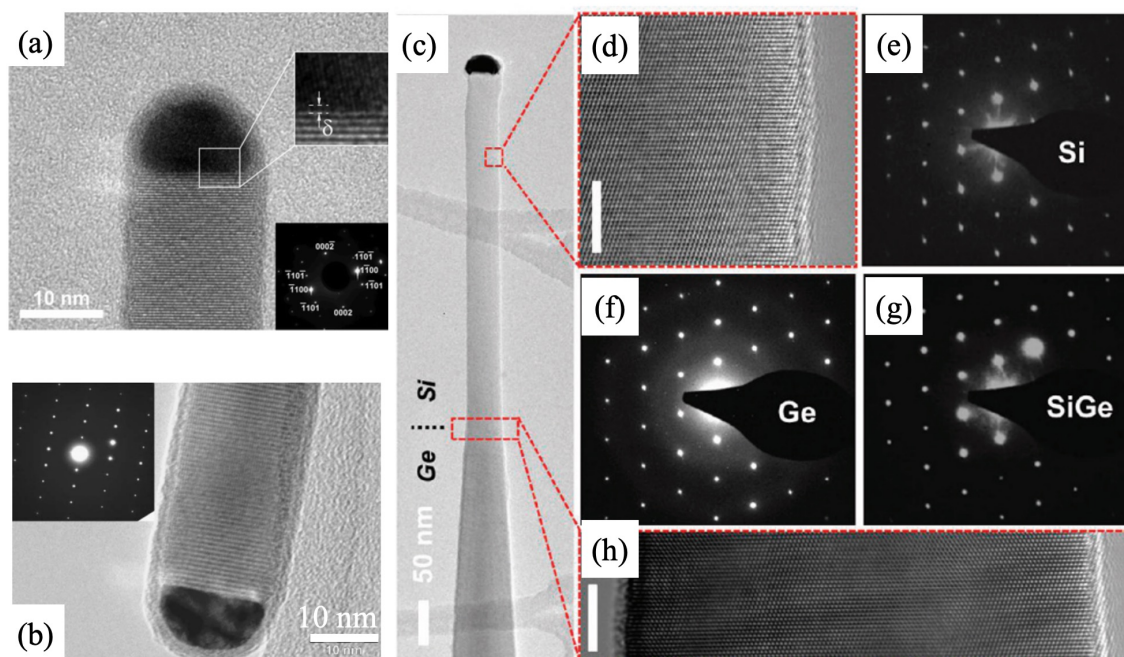


Figure 1.5: Examples of TEM images from routine examinations of different types of NWs. (a) TEM image of an InAs NW with Au catalyst on top. A magnified image of the NW-catalyst interface is shown in the top inset and a diffraction pattern from the NW is shown in the lower inset [51]. (b) NW-catalyst interface of another InAs NW with Au catalyst on top. Inset shows the diffraction pattern indicating zone axis of $\langle 1\bar{2}10 \rangle$ [52]. (c) A Si-Ge axial NW heterostructure with Au catalyst. Si and Ge segments are indicated along the NW length. (b) HRTEM image of the Si segment from the red box shows lattice fringes of a single crystalline Si. (e), (f) and (g) represent diffraction patterns from Si, Ge, and SiGe segments respectively, and demonstrate single crystal structure without stacking faults or twin boundaries. (h) HRTEM image of the transition area between Ge and Si. Scale bars in (d) and (h) are 5 nm [53].

Composition modulation of Ge-Si NW axial heterostructure was explored by Dayeh et al. by controlling growth conditions such as precursor pressure and temperature. TEM images from the NW are presented in Figure 1.5 (c)-(h) that was grown after reducing SiH_4 partial pressure. This reduction results in a decrease in the growth rate but the growth of single crystalline Ge-Si NW segments without noticeable defects [53].

However, the routine examination is limited to viewing in the perpendicular direction of the NW axis. Furthermore, NWs are removed from the growth substrate for the TEM examination eliminating the NW-substrate interfaces.

1.1.3.2 Cross-Sectional Work

The cross-sectional examination is also proved to be an effective technique to understand growth mechanisms and can be done by looking at the planar view and side view. The planar view can help to determine the cross-sectional shape, growth direction, and facet planes which give insight into the growth mechanism. Lee and co-workers conducted cross-sectional examinations to investigate the reason behind the growth direction of Si NW in the oxide-assisted growth (OAG) mechanism. They examined the shape, size, and growth direction of the NWs. Figure 1.6(a) shows a roughly rectangular Si core with well-defined facets of $\{111\}$ and $\{110\}$ planes and the growth direction measured for this type of NWs is along $\langle 112 \rangle$ direction. Figure 1.6(b) shows an HRTEM image of a single crystalline Si NW with a lattice spacing of 3.15 \AA and a twin boundary at 30° . The growth direction of this NW is determined to be $[110]$ based on the lattice image. The NW had a roughly circular cross-section with a facet of $[111]$ plane marked in the image.

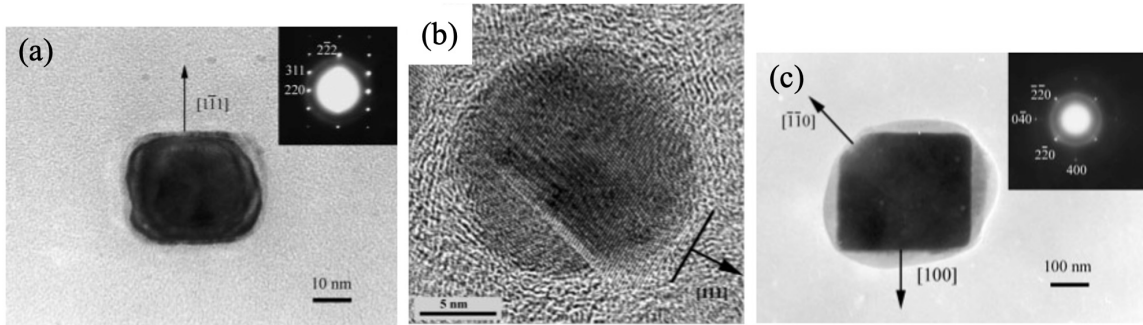


Figure 1.6: Cross-sectional TEM images of Si NWs grown along (a) $[112]$, (b) $[110]$ (HRTEM image) (c) $[001]$ [54].

Figure 1.6(c) shows another NW with a roughly pentagonal cross-section with an amorphous outer SiO_x layer. The growth direction of this NW was $\langle 001 \rangle$ and the occurrence of this type of NW was rare. Summarizing the results helped to find out a trend in the growth direction based on the relative surface energies of different crystallographic planes. Surface energy of $\{111\}$ is lower than $\{100\}$ and $\{110\}$, which facilitates the NW growth predominantly along $\langle 110 \rangle$ and $\langle 112 \rangle$ directions and bounded by $\{111\}$ facets [54].

Wu et al. obtained controlled growth of molecular-scale SiNWs with a small diameter distribution using gold nanoclusters as catalysts. But larger diameter NWs were observed to grow along $\langle 111 \rangle$ direction and smaller diameter NWs along $\langle 110 \rangle$ direction. Routine TEM examination of the NW-catalyst interface shows that for larger NW diameter, growth direction is along $\langle 111 \rangle$ due to the formation of the lowest free energy interface which is parallel to a single (111) plane. But smaller diameter NWs have V-shaped interfaces consisting of two $\{111\}$ planes, which result in the growth axis of $\langle 110 \rangle$. A planar view of the cross-sectional TEM image of a smaller diameter NW confirms the hexagonal cross-section with the well-defined facets of low free energy (111) and (100) planes and in agreement with the equilibrium shape [55].

Cross-sectional TEM examination from a side-view can assist to look at the NW-substrate interface for epitaxy, defects or amorphous layer, and catalyst-substrate

interaction during the initial state of growth. For example, Roest et al. demonstrated cross-sectional TEM examination to study hetero-epitaxial growth of III-V NWs on Si(111) substrate. Cross-sectional images of a single GaP NW and HRTEM of GaP-Si are shown in Figure 1.7(a) and (b). EDX analysis was used to determine that the catalyst particle consisted of Au and Ga. HRTEM image of the GaP-Si interface confirms epitaxial growth but also shows a typical roughness of about 5-10 nm. The roughness might be induced due to the formation of Au-Si eutectic alloy before NW growth. To investigate the initial growth stage, dark field and HRTEM images (Figure 1.7 (c) and (d)) were taken right after the annealing of Au colloids on the Si(111) substrate. Au particle is seen to be sunk into the substrate from the dark field image and thus creates a different $\{111\}$ facets than the initial (111) plane. When gas phase precursors of III and V materials are added for NW growth, these Au-Si particles dissolve but create a roughness in the interface.

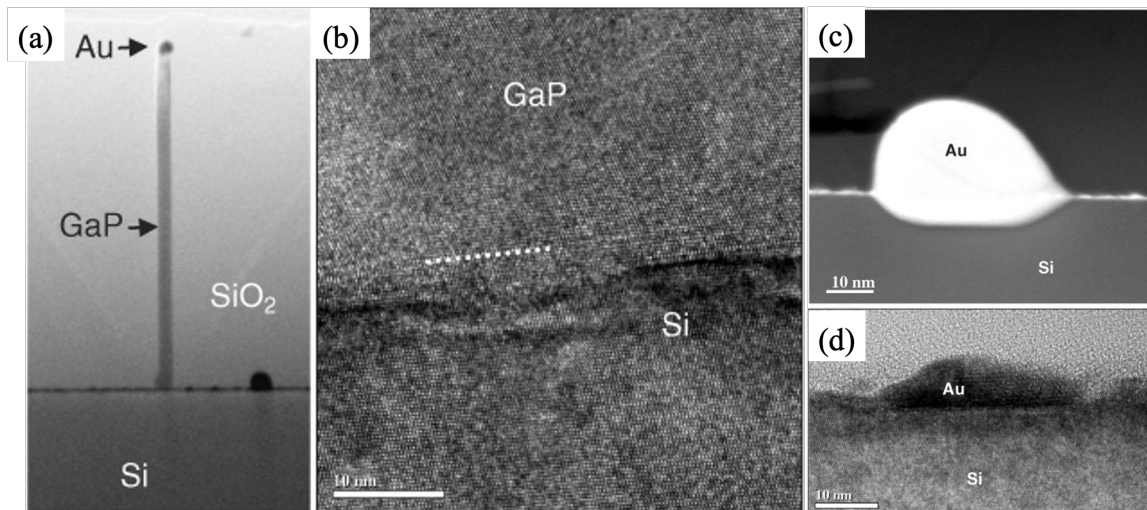


Figure 1.7: Cross-sectional examination of side-view for the growth of GaP NW on Si substrate. (a) TEM image of a single GaP NW (b) HRTEM image of GaP-Si interface, (c) and (d) high angle annular dark field (HAADF) and HRTEM images of two different Au particles on Si substrate after annealing. The dark field image clearly shows the particle sunk into the substrate [9].

Another cross-sectional study was demonstrated by Tomioka and Co-workers to determine the epitaxial growth of InAs NWs on Si substrate. Despite having a large

lattice mismatch, InAs NWs can be grown on Si substrate in the same manner as homoepitaxial growth. The cross-sectional TEM image shows that the NW-substrate interface is nearly atomically flat and the crystallographic structure of the NWs is similar to the ones grown on the InAs substrate. However, the cross-sectional TEM image also shows dark contrast in the NW-substrate interface of about 5 monolayer thickness. Strain mapping data provides that this dark contrast lamellar shape represents the misfit dislocations generated due to lattice mismatch. But the dislocations were accommodated in the interface and were not observed in the NWs [56].

1.1.3.3 In-Situ Technique

Section 1.1.1.1 discussed different synthesis methods to grow 1D nanowires that have been extensively studied. To obtain more control over the parameters such as compositions, sizes, crystal structures, and growth orientations of nanowires [57], a thorough understanding of the growth mechanism is important. For this purpose, many groups have proposed and investigated different growth mechanisms employing different strategies. As previously stated in section 1.1.1, Wagner and Ellis introduced the VLS growth mechanism that explained the role of impurities and the growth of dislocation-free Si whiskers [6]. Yang and co-workers conducted in situ TEM examination at high temperatures and reported real-time growth of Ge nanowire using gold (Au) nanoclusters as the catalyst for the first time [57]. Images recorded during nanowire growth (Figure 1.3) clearly showed alloy formation of Ge and Au, nucleation of Ge, and axial growth and formation of Ge nanowire [57] which is consistent with the VLS mechanism [6].

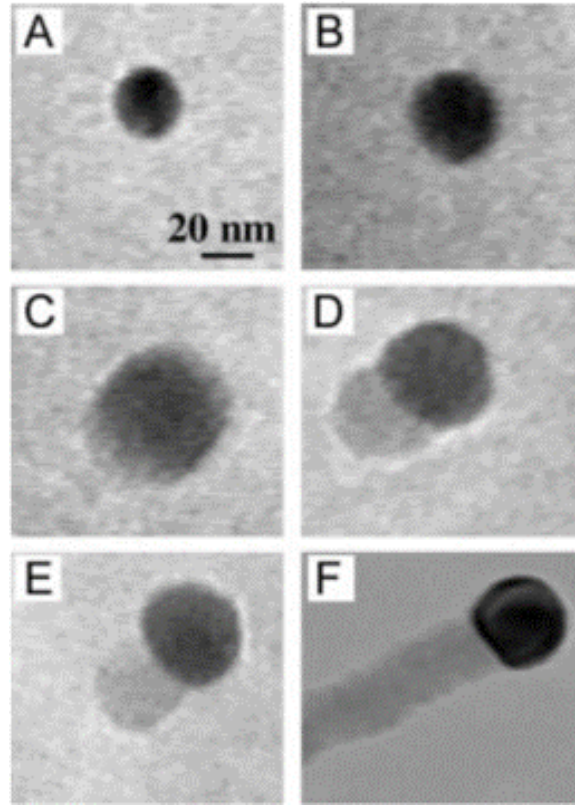


Figure 1.8: Real-time observation of Ge nanowire growth (a) solid Au nanoparticle, (b) alloy formation of Au and Ge and melting, (c) increase of alloy droplet size, (d) nucleation of Ge component after supersaturation, (e)-(f) Ge nanowire growth with increasing growth time [5].

Ross et al. also reported in situ growth of Au catalyst-assisted VLS growth of Si nanowires in an ultrahigh vacuum chemical vapor deposition (UHV-CVD) system. The sidewalls of the grown nanowires were periodically faceted. They proposed using thermodynamic arguments that near equilibrium, the sidewall facet does not have an ideal growth situation (energetically favorable facet, i.e., perpendicular to the growth direction), rather either has widening or narrowing geometry. While the facet is widening, there will be an inward force to favor minimizing the surface energy for the narrowing facet. Similarly in the next step, a widening facet will be introduced. The period and amplitude of the facet were observed to be directly proportional to the wire diameter. This type of periodic facet can happen in most semiconductor nanowires but can be difficult to observe without in situ observation as post-growth

oxidation or noncatalyzed CVD growth can affect the nanowire sidewall [58].

In-situ observation also allows measurement of the growth rate of individual nanowires along the length and sidewalls as demonstrated by Kadambaka et. al, which is otherwise unviable using post-growth measurements. From the real-time monitoring, the growth rate has been observed independent of diameter. This finding deviates from the generally accepted analysis of Givergizov which illustrates the proportional dependence of growth rate on wire diameter due to the Gibbs-Thomson effect. This deviation is seen because, in most of the VLS growth systems, dissociative adsorption of the precursor on the catalyst droplet is an irreversible process. In this case, Si desorption and evaporation are negligible due to the lack of a reactive environment and reaction temperature being not very high (500-650 °C). Also, it has been shown that the adsorption of Si in the catalyst is the rate-limiting step rather than the diffusion of Si through the catalyst and deposition of Si in the liquid-solid interface. Because it has been confirmed that the growth rate depends on disilane pressure linearly and the reactive sticking probability of an incident molecule is constant at different chemical potentials implying that the last two steps (diffusion and deposition) do not have any effect on the growth rate. However, the growth rate has been seen to depend on tapering. Due to out diffusion of the catalyst in case of decreasing wire diameter, an excess of Si is deposited at the liquid-solid interface that increases the nanowire growth rate and vice versa for the increasing wire diameter [59].

In-situ technique is much more useful than other techniques and gives dynamic growth information on nanowires. However, this is expensive and only available in large research facilities including national laboratories. A brief comparison between different TEM-based techniques is presented in Table 1.2.

Table 1.2: Comparison table for different TEM based growth mechanisms [9, 54, 57, 60].

Method	Advantage	Disadvantage
“Routine” TEM examination	<ul style="list-style-type: none"> • Simple (i.e., no extensive sample preparation) • “Quickly” provide information such as diameter, growth direction etc. 	<ul style="list-style-type: none"> • Nanowires can only be viewed perpendicular to their axial axis • The nanowire-substrate interface is lost
Cross-sectional TEM examination	<ul style="list-style-type: none"> • Both side view and plan view • Provide information at the nanowire-substrate interface 	<ul style="list-style-type: none"> • Tedious sample preparation
In-Situ TEM examination	<ul style="list-style-type: none"> • Provides dynamic observations of the growth of nanowires 	<ul style="list-style-type: none"> • Special TEM set-up (mostly only available in national labs or large research centers)

1.2 Summary

In this dissertation, we addressed two issues. As discussed briefly in the section 1.1.2, establishing structure-property correlation is crucial for a better understand-

ing of materials properties and their applications. As a part of the collaborative work, we were motivated to develop the correlation between obtained mechanical and thermal properties and structural parameters of niobium selenide NWs because of their anomalous thermal properties observed in ultrathin NWs. However, niobium selenide has a monoclinic chain-like structure, which poses roadblocks to determining the structural parameters. Inspired by the work done by Guan et al. [61] to obtain ‘hidden’ defects in boron carbide NWs, which has a complex rhombohedral crystal structure, we performed a thorough TEM examination to build a diffraction pattern roadmap and obtain structural parameters from NWs. The correlation between lattice parameters and the width of the NWs proved to be neutral, eliminating the structural effects on the unusual properties. The background information, challenges in obtaining the data, and results are discussed in detail in chapter 3.

In chapter 4, we discussed the growth mechanism study of boron carbide NWs. Based on the discussion in the section 1.1.3, extensive research has been conducted to investigate the effects of different growth parameters and explain the growth model/mechanism of different material systems, especially group IV and III-V materials. However, many fundamental aspects still need to be realized such as at which growth conditions planar defects, and kinks are formed in the NWs. Thus, predicting the reasonable growth model is still not possible.

In the past decade, our group has synthesized boron carbide NWs, characterized planar defects, measured thermal conductivity, and established structure-transport property relationship in collaboration with researchers at Vanderbilt University [62, 61, 63]. Routine TEM examination was performed thoroughly to explore growth mechanisms with different planar defects as well. But as discussed in the section 1.1.3, only routine examination cannot provide all the information, specifically the NW-substrate interface after growth and catalyst-substrate interface in the initial growth stage. To gain more insight into the growth mechanism, we conducted cross-

sectional examination of boron carbide nanowires. As stated before, the catalyst plays important role in the nucleation and growth of the nanowire, therefore, we put emphasis on the formation of catalyst nanoparticles during the initial stage of the growth. For this purpose, the effect of each constituent element on the synthesis of boron carbide nanowires with control experiments was studied. Results from the cross-sectional studies emphasize the effects of the reactant parameters and provide insights into the growth of the boron carbide NWs.

CHAPTER 2: EXPERIMENTAL METHODS AND TOOLS

Major steps to conduct the experiments for this dissertation include synthesis of boron carbide nanowires, characterization of individual nanowires using scanning electron microscope (SEM), transmission electron microscope (TEM), and energy dispersive x-ray spectroscopy (EDX), and preparation of cross-sectional samples for TEM examination. In this chapter, synthesis methods, working principles of the characterization tools including their operation parameters, and helpful software tools (such as CrystalMaker[®] and imageJ) are discussed.

2.1 Electron Microscopy

Electron microscopy, providing higher resolution, large depth of fields, and ample compositional information, is extensively used in this work. In electron microscopes, a beam of electrons is used to form an image in contrast to a visible-light microscope (VLM) that uses photons. Because of using the shorter wavelength of electron beams, they provide advantages such as higher resolution, magnification, and depth of field over VLM. Image resolution can be defined as the smallest distance between two points that is distinguishable from each other. Resolution of VLM is limited by the wavelength (λ) of visible light and can be approximated by Rayleigh criterion [64]:

$$resolution, \delta = \frac{0.61\lambda}{NA} \quad (2.1)$$

where NA represents the numerical aperture of the lens. According to the equation 2.1, using the shortest wavelength of visible light (≈ 400 nm) and maximum value of NA (≈ 1.5), the best resolution for VLM can be estimated as 200 nm [65]. This resolution limit can be overcome by using a much smaller wavelength of electrons which

can be determined approximately from the electron energy by using the following equation (ignoring the relativistic effects)

$$\lambda = \frac{1.22}{\sqrt{E}} \quad (2.2)$$

Where E is the electron energy. Another property, depth of field indicates the depth of the object plane within which the object can be moved while still maintaining focus. Depth of focus is the equivalent depth in the image plane. A larger depth of field of SEM can be used to generate 3D-like images and in TEM, for electron transparent samples, top and bottom surfaces can be imaged while both remaining in focus at the same time [64].

In electron microscopes, when high-energy electrons strike the sample, a wide range of signals are generated from the sample. A summary of different types of signals generated from a thin specimen is shown in Figure 2.1. These signals can be detected using different types of TEM/ SEM, and used for the characterization of the specimen. For example, secondary and backscattered electrons are used in SEM to obtain topographical and compositional images of the specimens.

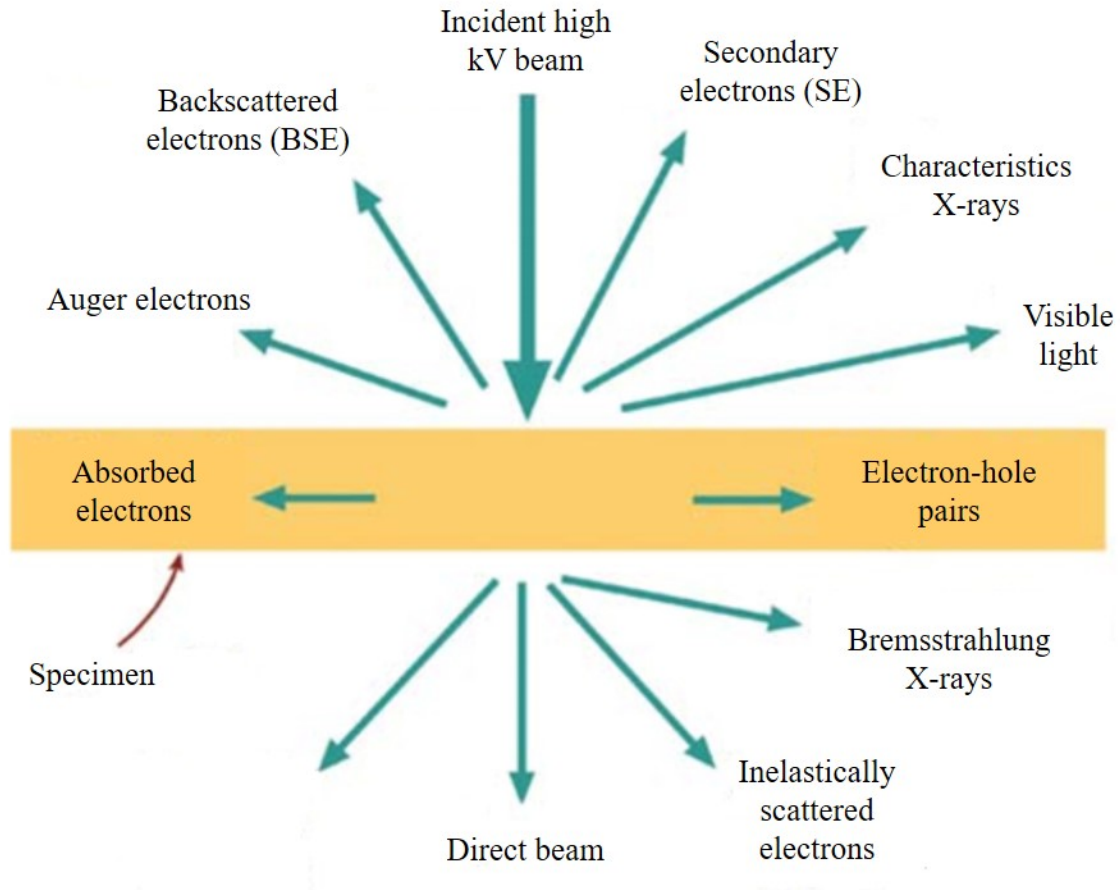


Figure 2.1: Different types of signals generated due to the interaction of high energy electron with a thin specimen [64].

In the following two subsections, the components and mode of operations of SEM and TEM are discussed in more detail.

2.1.1 Scanning Electron Microscope (SEM)

Due to easy operation and maintenance, SEM is one of the most widely used tools for nanostructured materials [65]. Generated by scanning the surface of the specimen, SEM images can provide information about the variation in the geometrical features (topography) and chemical composition of the specimen. Major components of SEM include an electron gun, electromagnetic lenses and apertures, scanning coils, detectors, and a vacuum system as shown in the schematic diagram below.

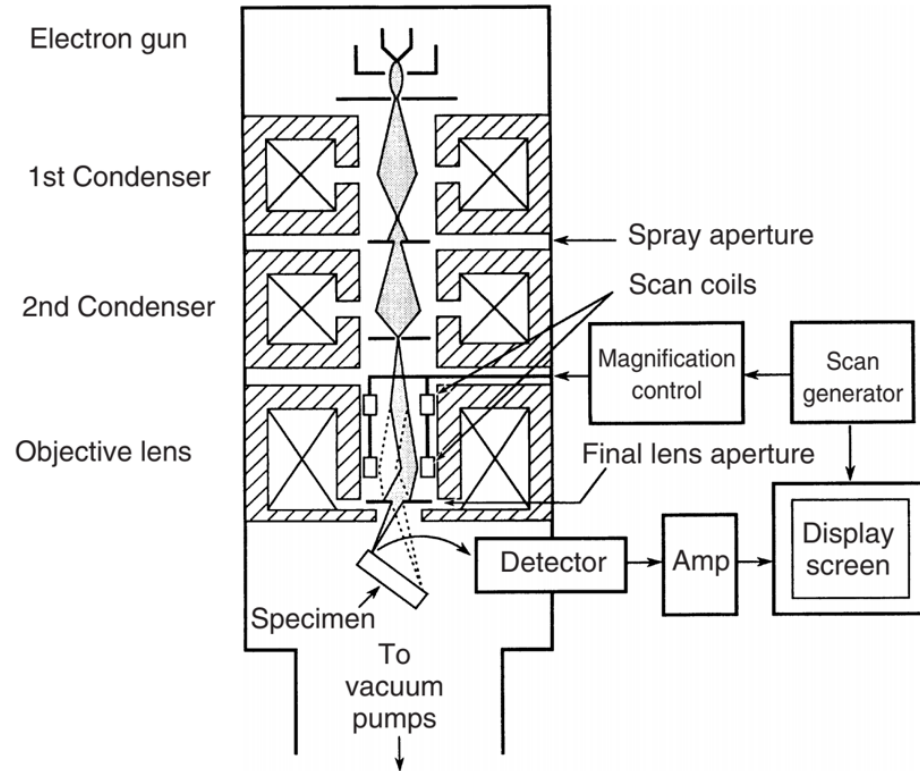


Figure 2.2: Schematic Diagram of an SEM showing major components and ray diagram for image formation [65].

From Figure 2.2, the electron gun is located at the top of the column and used to generate a beam of electrons by applying acceleration voltage between the electron source (acts as a cathode) and anode plate. Acceleration voltage in SEM ranges from 1 to 40 KV [65]. Two types of electron sources or guns are available, thermionic electron guns and field emission guns (FEG). Using the thermionic gun, an electron beam can be generated by applying thermal energy. Tungsten (W) filament due to having a high melting point, and lanthanum hexaboride (LaB_6) crystal because of having low work function are used as thermionic sources. FEG is in the shape of a very fine needle known as a tip. Electrons can be generated from the FEG tip by applying a voltage as the electric field strength is very high at the sharp point. Compared to the thermionic gun, FEGs have smaller source sizes, higher brightness, and better coherency but lower stability and require higher vacuum. Also, FEGs

are not good for routine, low-magnification imaging because of the smaller source size. Between thermionic sources, LaB_6 has better properties compared to tungsten filament. But tungsten filament is still used for SEM because of its lower price, similar beam stability as LaB_6 , and requires relatively low vacuum [64].

In the column, also there are two condenser lenses and one objective lens (Figure 2.2. These are electromagnetic lenses that consist of a cylindrical core of magnetically soft material such as soft iron with a hole through it. The core is termed a pole piece which is surrounded by a copper coil. A schematic diagram of the electromagnetic lens is demonstrated in Figure 2.3. When current is applied through the coil, it creates a magnetic field in the hole. Electron beam paths are controlled by the strength of the magnetic field of the lenses [64].

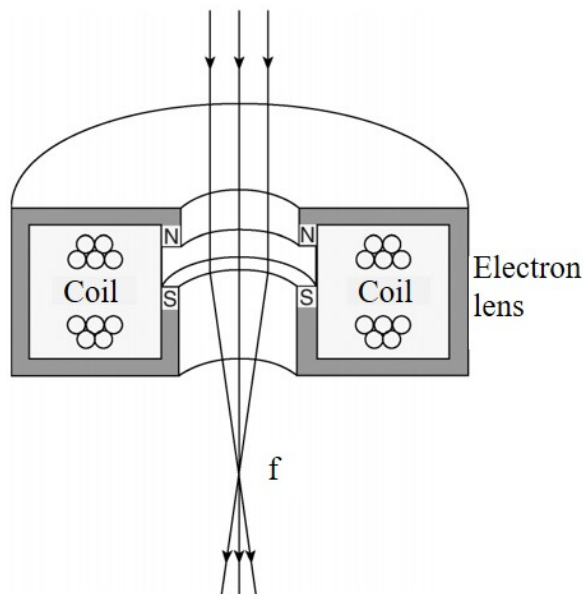


Figure 2.3: Basic structure of an electromagnetic lens [65]. A Pole piece surrounded by copper coils is demonstrated schematically. Current runs through the copper coils and creates a magnetic field in the hole. The strength of the magnetic field is weak along the axis but stronger towards the pole piece. So off-axis electrons are deflected more strongly [64].

In SEM, two condenser lenses are used to decrease the size of the beam cross-over and the objective lens focuses the beam into a small probe on the specimen. The

function of the objective lens is very different in SEM as it demagnifies the beam cross-section. That is the opposite in the case of TEM [65]. Probe diameter is also referred to as spot size. Probe size can be reduced by changing the current in the condenser lenses [66]. Also, there are apertures used after each lens to refine the beam by limiting higher scattered beams and increasing the resolution, and depth of field, and reducing the charging effect.

Another major component of SEM that distinguishes it from conventional TEM is the use of deflectors or scanning coils. By changing the current in the scanning coils, the beam can be deflected in the x-y plane and the specimen can be scanned line by line creating a raster pattern. Beam deflection can be seen following the ray diagram in Figure 2.2.

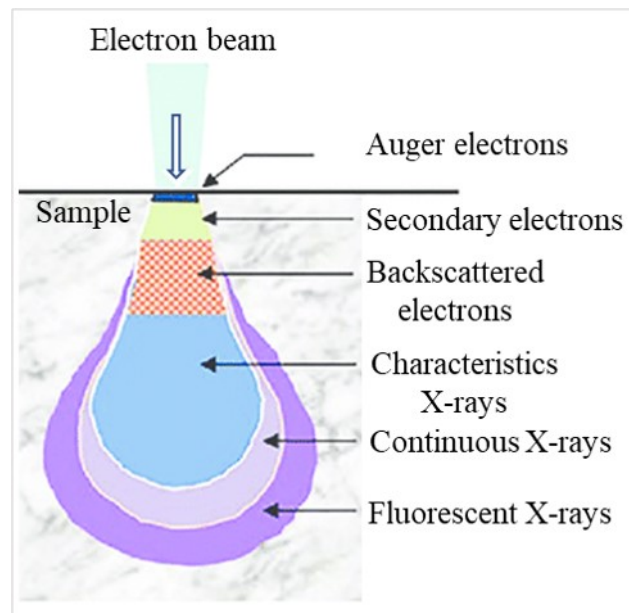


Figure 2.4: Schematic drawing of interaction volume [67] under the specimen surface produced due to electron-specimen interactions. Different signals escape from different zones of the interaction volume.

As mentioned before, when the electron beam interacts with the specimen surface, different signals are generated due to electron scattering (Figure 2.1). The interaction zone represented as a pear-shaped zone in Figure 2.4 indicates that interaction

happens below the specimen surface within a particular volume. Different types of electron signals such as secondary electrons (SE), backscattered electrons (BSE), and characteristic x-rays escape from the different zones of the interaction volume. SEs are generated from the subsurface (within 5-50 nm from the surface) due to the inelastic scattering. Typically they have lower energies but are sensitive to the surface structure, thus, can provide surface topographic information. On the other hand, BSEs are produced due to the elastic scattering of incident electrons with the specimen. They have higher energies and can be used for compositional contrast for specimens containing two or more chemical elements. Incident electrons are backscattered more strongly by the specimen with a higher atomic number (Z), creating more BSEs and will appear brighter. For typical SEM operation, SEs and BSEs are captured using separate detectors. In SEM, a commonly used detector is named the Everhart-Thornley (E-T) detector which consists of a scintillator, a light guide, and a photomultiplier tube (PMT). The scintillator converts electrons into photons, then, the light guide directs the photons towards the PMT which converts photons to electrical signal again and amplifies the signal [65]. For SE, the E-T detector is placed at the side of the chamber at an angle to increase the signal collection efficiency. For BSE, a separate detector (usually a semiconductor detector or scintillator type) is placed directly above the sample in a ‘doughnut’ geometry to maximize the BSE signal collection.

To obtain high-resolution images using SEM, three parameters, acceleration voltage, working distance, and spot size are important along with the alignment of the microscope. With higher acceleration voltage, more electron beams will be generated but it will affect the specimen. Working distance is the distance of the specimen surface from the lower end of the objective lens. If the working distance is reduced, the convergence angle of the probe will increase and the probe size will be reduced. As a result, the resolution will increase but the depth of field will be decreased. Also,

a larger convergence angle can cause spherical aberration, and too small a probe/spot size will block sufficient signal electrons for the imaging. So, optimum working distance, and spot size are required. For our work, after the synthesis, as-grown boron carbide nanowires were examined using SEM (JEOL, model JSM-6480, with a tungsten filament as electron source). For the imaging in SE mode, spot size, working distance, and acceleration voltage were selected as 30 nm, 10 mm, and 10 KV respectively.

2.1.2 Transmission Electron Microscopy (TEM)

A transmission electron microscope (TEM) is another powerful tool to examine nanostructured materials. TEM can provide a wide range of structural and chemical information such as size and shape of particles and grains, lattice type, phase type, crystallographic information, defects structure, grain boundaries and interfaces, chemical composition, and so on [68, 69]. Electron diffraction and high-resolution TEM images can be used to obtain the microstructure of defects, grain boundaries, and interfaces in great detail. Similar to SEM, the major components of TEM are an electron source, different types of electromagnetic lenses, a sample stage, a vacuum system, and electron detectors, but the structure of TEM is more sophisticated than SEM as can be seen in Figure 2.5. In TEM, typically higher acceleration voltage (80-400 KV) than SEM is used which generates electrons of much higher energy and extremely short wavelength. According to equation 2.1, a much better resolution is expected and that is confirmed in reality. Both thermionic and FEGs can be used. As the thermionic source, only LaB₆ crystal is used as beam intensity and the lifetime of the tungsten filament is too less. But as mentioned before, LaB₆ electron gun requires a higher vacuum.

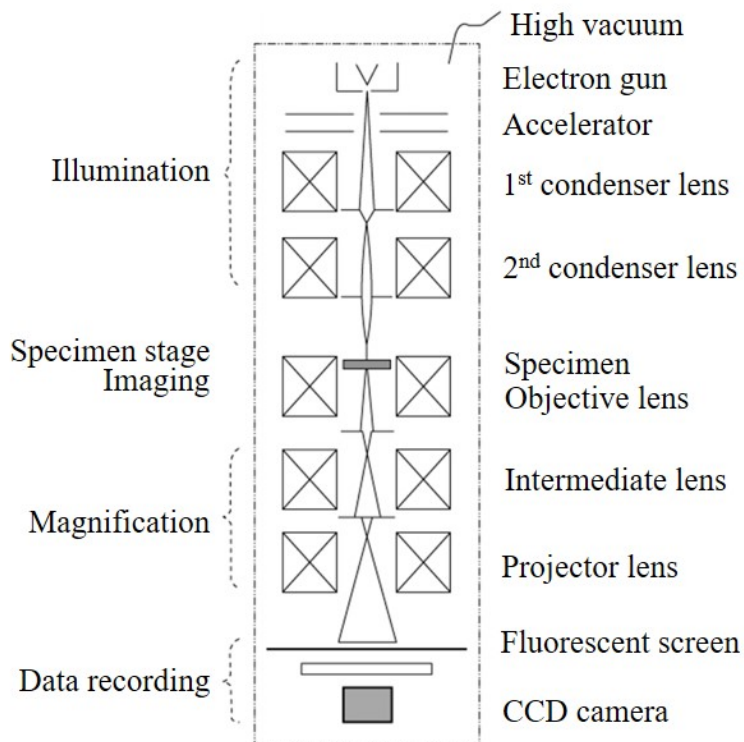


Figure 2.5: Schematic structure of TEM [65]

TEM is operated in two basic modes- diffraction mode and imaging mode. An intermediate lens is used to switch between two modes. Formation of diffraction pattern (DP) and imaging can be explained by ray diagram from Figure 2.6. When electrons pass through the crystalline sample, a DP is created at the back focal plane (BFP) of the objective lens. In diffraction mode, imaging system lenses are adjusted in such a way that the back focal plane (BFP) becomes the object for the intermediate lens. Then, DP is projected for viewing onto the screen. Usually, A selected area aperture is used to reduce the direct beam intensity and also to select the electrons from a specific area, thus the DP is often called selected area DP (SADP). In the imaging mode, lenses are adjusted so that the image plane of the objective lens works as the object plane of the intermediate lens. A magnified image is projected on the screen by the projective/projector lens. The blue arrows show the orientation of the images formed in each lens. An objective aperture is used to perform bright field

(BF) and dark field (DF) imaging which can increase the contrast of the images. An objective aperture can be seen in Figure 2.6(b) inserted in the BFP.

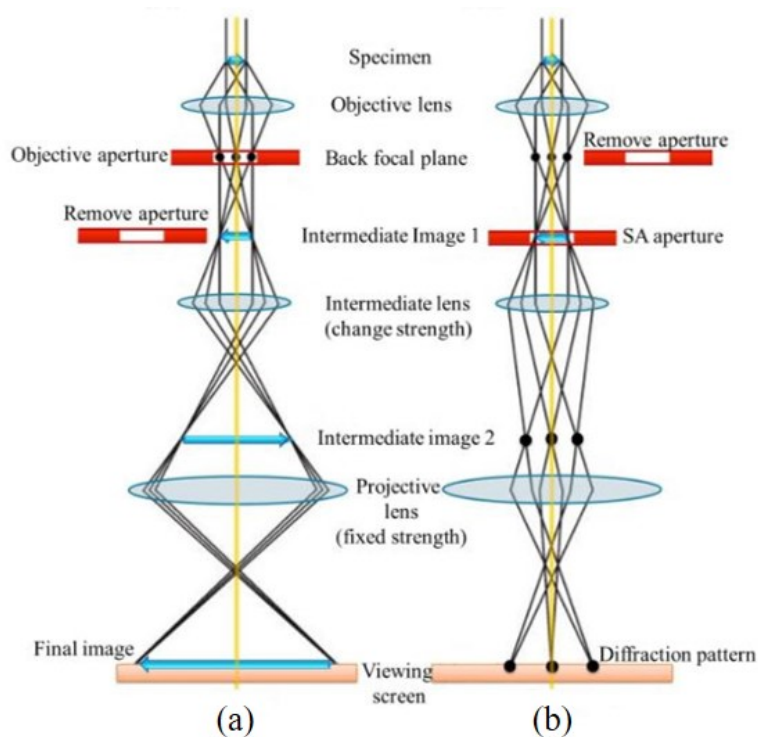


Figure 2.6: Ray diagram showing (a) imaging and (b) diffraction mode [70].

BF and DF images can be formed by simply choosing the specific electrons for the imaging. For BF imaging, a direct transmitted beam is selected for the imaging. This can be performed by placing the objective aperture around the central bright spot in the diffraction mode and then switching back to the imaging mode to capture the BF image. On the other hand, DF images are taken by placing the objective aperture in one of the diffracted spots i.e., scattered electrons are chosen for the imaging blocking the direct transmitted electrons. As mentioned earlier, BF and DF imaging are performed to enhance the contrast of the images. Crystalline, and heavy atoms (high Z), diffracts more strongly and appear as dark in BF mode due to blocking scattered electrons, but they appear bright in the DF. Also, DF mode can be used to image small crystalline features as the background will be dark due to preventing

transmitted electrons. Thus, image contrast can be increased by using either of the two modes.

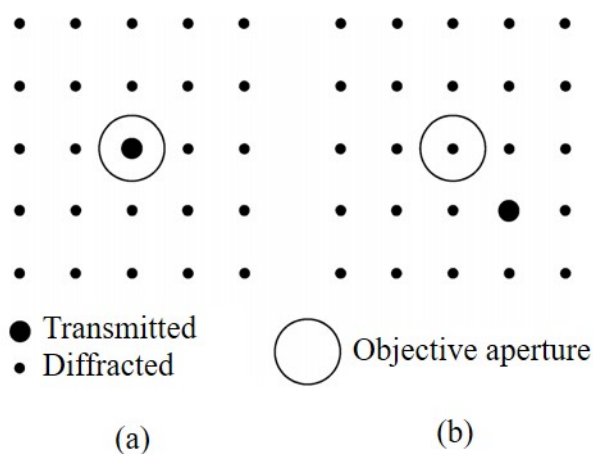


Figure 2.7: Selection of transmitted and diffracted spot for (a) BF and (b) DF imaging by using objective aperture shown as circles [65].

Obtaining strong contrast is very important for any imaging technique and analysis. Contrasts in TEM images are generated due to incident electron waves changing their amplitude and phase. Hence, two main types of contrast can be obtained, (i) amplitude contrast, and (ii) phase contrast. Amplitude contrast is created depending on the (a) mass and thickness of the specimens, and (b) diffraction through the specimen. The first one, mass-thickness contrast is generated due to incoherent elastic scattering that depends on atomic number Z and thickness, t . Keeping all factors constant, higher Z and t , will scatter more electrons compared to the other areas and create the contrast. This is most useful for imaging amorphous and biological samples. Diffraction contrast is generated due to coherent elastic scattering at Bragg angles. The major difference in mass-thickness and diffraction contrast is that diffraction contrast is highly sensitive to tilting. For DF imaging with mass-thickness contrast, any diffracted spot can be used. But to achieve strong diffraction contrast, the sample needs to be tilted so that one diffracted beam is stronger than others. Because of the two beams present (including the direct beam) in the DP, this is called two-beam

conditions [64].

Phase contrast in TEM is created due to phase differences of electron waves after scattering through the specimen. Whenever more than one beam is being used to generate the image, phase contrast can be seen as fringes. More beam results in higher resolution. A schematic image using multiple beams and diffraction patterns is shown in Figure 2.8. But it is to be noted that these fringes do not correspond to the atomic position in the lattice, but can provide information about the lattice spacing and orientation [64].

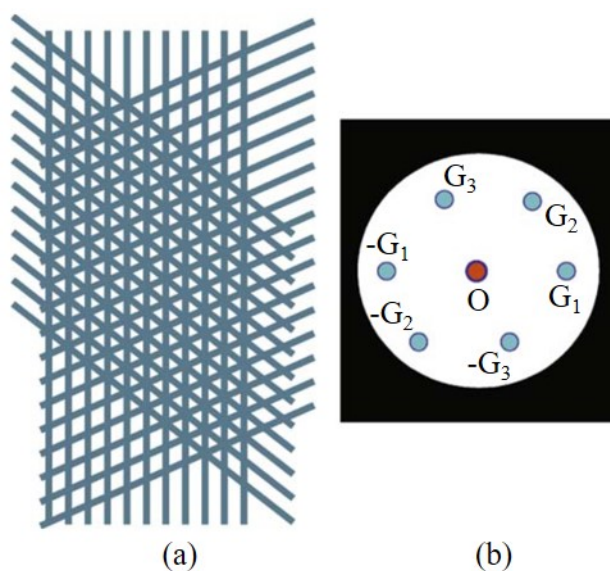


Figure 2.8: An example of fringes created by using many beams [64].

2.1.2.1 Methods of Obtaining DP, HRTEM Images and Indexing

To obtain HRTEM images, first, the sample is tilted to a lower zone axis, which is projected in the diffraction mode as the Kikuchi pattern. By changing the condenser lens, brightness is changed to obtain diffraction spots.

Camera Constant Equation

To analyze electron diffraction, the camera constant equation is used which is derived from Bragg's equation. From Bragg's equation, it can be written as follows,

$$\frac{\lambda}{d} = 2 \sin \theta \approx 2\theta \quad (2.3)$$

where d is the lattice spacing of the specimen. Camera length (L) can be defined as the distance traveled by electrons between the specimen and the viewing screen. L is not a physical distance but a calculated value and it depends on the lens settings in the microscope.

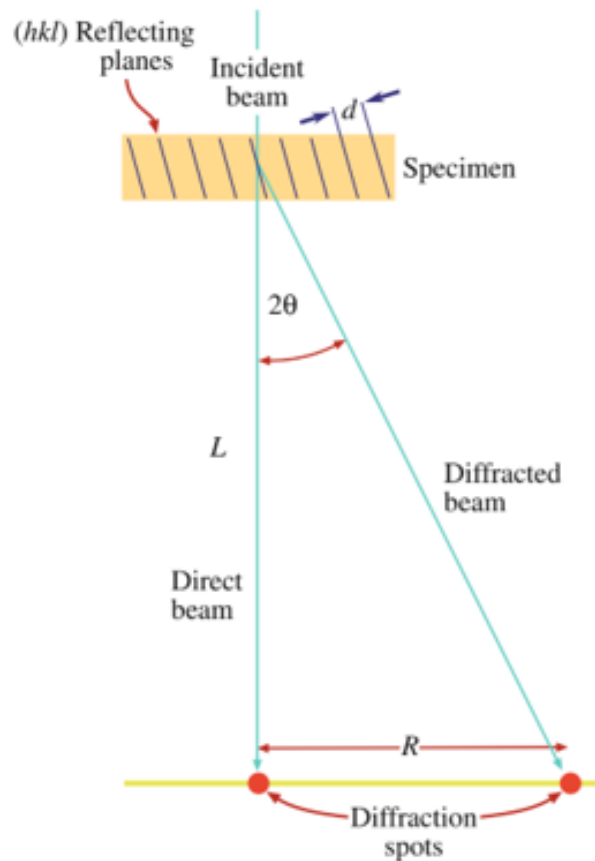


Figure 2.9: Schematic drawing of a direct beam and a diffracted beam showing the relationship between camera length, L , and distance between direct spot and diffracted spot, R . R represents the lattice spacing in the reciprocal plane. The figure indicates the electron ray paths in the imaging system but lenses are avoided for simplicity [64].

Figure 2.9 represents a schematic electron ray path of a direct beam and a diffracted beam and indicates the relationship between L and R . From the figure,

$$\frac{R}{L} = \tan 2\theta \approx 2\theta \quad (2.4)$$

From equation 2.3 and 2.4,

$$\begin{aligned} \frac{R}{L} &= \frac{\lambda}{d} \\ \lambda L &= Rd \end{aligned} \quad (2.5)$$

Equation 2.5 is known as the camera constant equation where the camera constant is indicated by λL . λ can be measured from the electron energy. This equation is used to calibrate the microscope for camera length. However, in modern TEM, λL is calibrated in such a way that the value is close to unity. Thus equation 2.5 can be used to determine d spacing from the DP by measuring R . But the magnitude of planar spacing d can be calculated by taking the reciprocal of reciprocal lattice vector r . So, in the equation 2.5, λL is a projection factor relating DP with the reciprocal lattice. The equation can also be used to compare the ratio of distances of two spots from the central undiffracted spot and the ratio of planar spacings of two planes.

Indexing

For indexing a DP, a table is created. The table shows an example of recording the data measured from DP and other calculations. From a DP, first, distances of four diffraction spots from the central spot (R) are measured, and taking the inverse of R , d is measured. After measuring, d spacing for the first two spots is compared with the ICDD file and hkl values are assigned for them tentatively. According to the vector addition, third spots can be assigned by adding the first two hkl values. Similarly, fourth spots can be assigned. After assigning, ratios are calculated and compared with the ratio of theoretical values.

Calibration of TEM

TEM alignment and calibration are important to do any analysis accurately using the images or DPs, especially, after maintenance or servicing of the equipment. Apart from the overall alignment of the lens, aperture, centering of current, and voltage, calibration of DP is important to validate any measurement from it. Another issue in our TEM is the configuration of the charge-coupled device (CCD) camera, which gives slightly different values while measuring in the horizontal and vertical directions. For example, a DP from a Silicon sample is presented in Figure 2.10 (a). Two equivalent spots $1\bar{1}1$ and $11\bar{1}$ are shown in the DP. Central bright spot due to direct transmitted beam is blocked by a beam stopper, as it may damage the camera. After measuring the distance of those two spots from the central spot (by measuring the total distance of four spots and dividing by four), $R_{1\bar{1}1}$ and $R_{11\bar{1}}$ provides slightly different values (3.2475 and 3.2150 1/nm respectively). This is because $1\bar{1}1$ and $11\bar{1}$ spots are at two different angles. So, all the measured data needs to be corrected using a standard calibration sample. Reference standards such as MAG*I*CAL[®] (Electron Microscopy Sciences) can be used for both magnification and camera constant calibration. In our case, to calibrate DPs obtained at different angles, a diffraction standard evaporated aluminum sample (Ted Pella, product no. 619) is used.

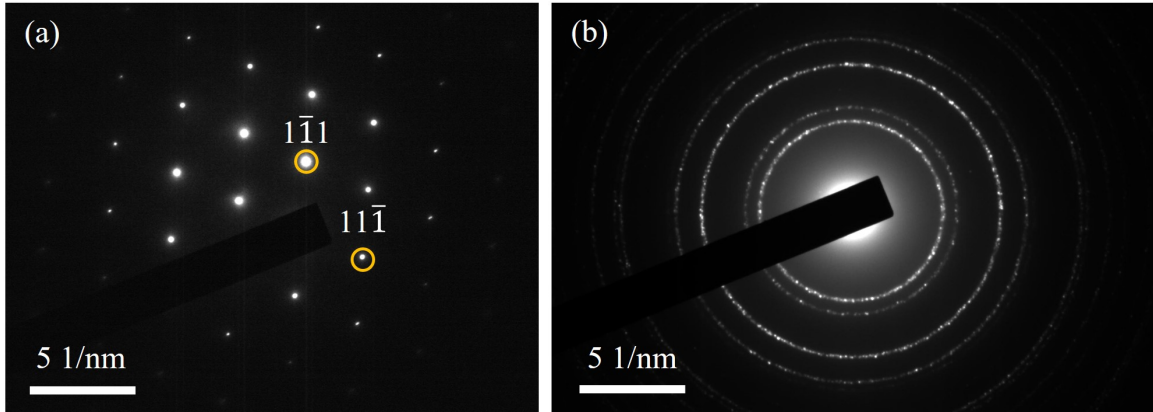


Figure 2.10: (a) Example of a DP from a Si sample showing two equivalent spots which provide slightly different values of R after measurement, (b) DP from a diffraction standard evaporated aluminum sample.

Diffraction standard aluminum sample provides DP as ring pattern because of having very small size crystallites [71]. To calibrate each spot in an experimental DP, first distance R is measured, the correction factor is calculated from the standard DP at the same angle as the spot of the experimental DP, then multiplied with the R value to obtain the corrected R value. Thus, before the examination of each sample, first, a DP is obtained from the calibration sample maintaining the same alignment procedure, electrical, magnetic conditions, and camera length, and calibration is performed.

For our work, a JEOL (model JEM-2100) TEM with a LaB_6 electron source was used at an acceleration voltage of 200 KV, and BF images, HRTEM images, and SAEDPs were collected from the boron carbide nanowire samples. To obtain SAEDPs and HRTEM images, samples were tilted to different zone axes using a JEOL double-tilt holder and a Gatan double-tilt holder. Large angle tilting (up to $\pm 30^\circ$) in both X and Y directions is possible using the two holders. First, individual nanowires and then, cross-sectional samples prepared from growth substrates were examined using TEM. The preparation of cross-sectional samples is discussed in section 2.3.

2.2 Energy Dispersive X-ray Spectroscopy (EDS)

Energy dispersive X-ray spectroscopy (EDS) is an analytical technique that utilizes characteristic X-rays emitted from the specimen to detect and identify constituent elements in the specimen. Integrated into SEM or TEM, the EDS system transforms the electron microscope into a more powerful system, named analytical electron microscope (AEM) [64]. Due to electron-matter interaction, different types of X-rays (characteristic, continuum, and fluorescent X-rays) are produced as shown in Figure 2.4. Among them, characteristic X-rays can be used to plot X-ray count versus X-ray energy spectrum that can provide different characteristic peaks for different elements.

The generation of characteristic X-rays can be explained in three steps (Figure 2.11). When the high energy electron beam is incident on the sample surface, it can knock out electrons from the inner shells of the atoms. That results in holes in those shells. Then, electrons from outer shells move to the holes in the inner shell releasing excess energy as characteristic X-rays. Depending on the inner shell where the hole is created and the outer shell from which an electron fills up the hole is used to annotate characteristic X-rays. For example, if the electron is knocked out from K-shell and the electron from L, M, or N shell moves to occupy the hole generated in K-shell, X-rays will be termed as $K\alpha$, $K\beta$ or $K\gamma$. Similarly, other possible X-rays are $L\alpha$, $L\beta$, $M\alpha$, etc.

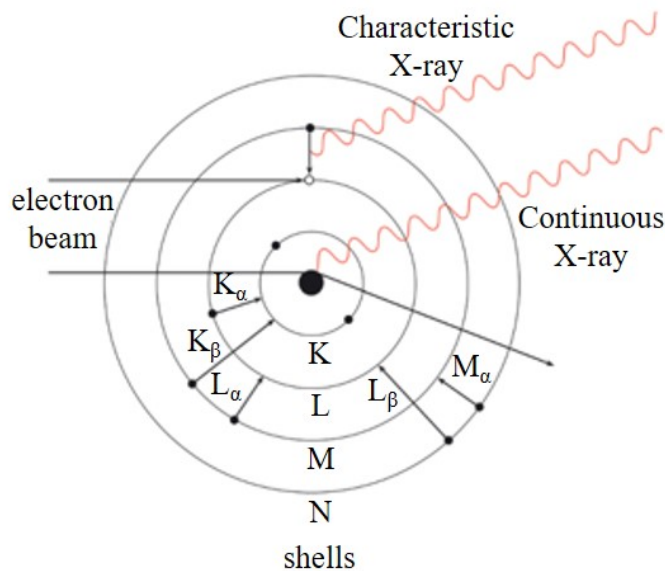


Figure 2.11: Generation of characteristic X-ray [72] by knocking out an inner shell electron, creating a hole and an outer shell electron filling up the hole releasing excess energy as characteristic X-ray. Also, the generation of continuum X-ray by the interaction of the incident electron with the nucleus is shown in the figure.

Semiconductor-based X-ray detectors are used for EDS. The most commonly used EDS detector is a lithium drifted Si or Si(Li) detector. Typically a detector consists of a collimator to collect X-rays generated only from the primary electron beam, an electron trap to prevent other signals or electrons from collecting, a semiconductor crystal for the detection, a window to keep the crystal separated from the SEM/ TEM chamber, and electronics for the detection of the electron charge, conversion of it to a voltage pulse and sending the pulse to the pulse processor [73]. The components of the detectors can be seen in Figure 2.12.

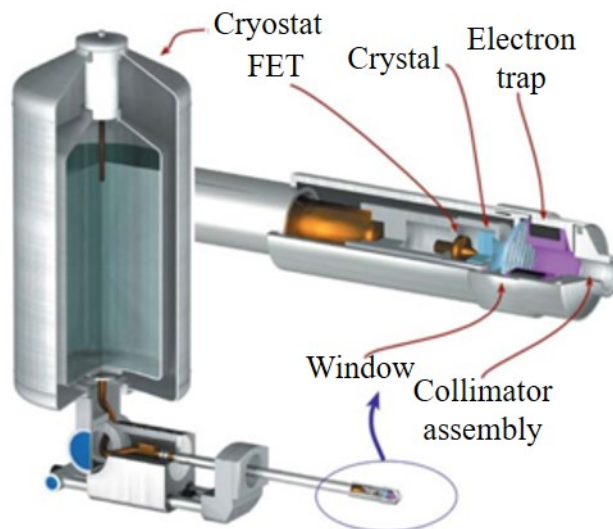


Figure 2.12: A blown up diagram of the Si detector showing different parts including cryostat (liquid nitrogen dewar) [64]

When X-rays hit semiconductor crystals, electron-hole pairs are created inside them. In Si(Li) detector, Li is added to make the Si intrinsic as commercial Si is usually p-type even in the purest quality. The front of the crystal is made p-type and the back is made n-type, thus creating a p-i-n device. When a reverse bias is applied, electrons and holes are separated and electrons are attracted to the back contact which is passed to the pulse processor of the electronics. The electron pulse measured at the rear contact is proportional to the X-ray energy detected at the semiconductor crystal, which is unique for each element. The detector is always kept in a liquid nitrogen environment to avoid the generation of electron-hole pairs due to thermal energy, thus reducing the noise level in the EDS spectrum [64]. As mentioned before, X-rays are needed to pass through a window to reach the semiconductor detector. Usually, a thin sheet of Beryllium ($\approx 10 \mu\text{m}$) is used as a window which allows most X-rays with little absorption [65]. But elements of $Z < 11$ are not possible to detect, as low energy X-rays from lighter elements get absorbed by the Be window. Be with $\approx 7 \mu\text{m}$ will be more suitable to detect lighter elements but that is more expensive. To solve the issue, modern EDS is equipped with ultra-thin polymer window detectors

or windowless detectors [64].

X-ray counts are plotted against X-ray energy which generates the EDS spectrum. First, all the elements in the sample are identified carefully by analyzing all the major peaks. Then, quantitative analysis is performed to calculate the relative weight or atom percentage of each element. However, some common artifacts can be generated in the EDS spectrum which can create errors in the identification of elements. Artifacts can be generated during signal detection and processing. For example, high-energy X-rays can fluoresce Si from the detector and it can escape from the intrinsic region, showing a small peak in the spectrum. This can be easily recognized and eliminated by the analysis software or user, as it is a low-energy peak. Another artifact, the sum peak occurs when two X-ray photons with different energies enter the detector coincidentally and are analyzed as the sum of the energy of two photons. This happens usually due to a high input count rate or dead time and can be eliminated by maintaining a reasonable count rate and lower dead time. But care must be taken while analyzing the EDS spectrum to avoid any artifacts [64].

In our work, two INCA EDS systems from Oxford Instruments were used and integrated with SEM and TEM respectively. It has a Si(Li) detector and a thin Be window that is able to detect boron and carbon. In TEM, the local composition could be determined from a small region such as in the nanowire core and sheath.

2.3 Preparation of Cross-Sectional Sample

TEM cross-sectional examinations were performed on samples such as SiO₂/Si substrates which were used to synthesize boron carbide nanowires, annealed substrates, and substrates with as-synthesized nanowires with different synthesis parameters. The general sample preparation techniques involve cutting the specimen into small pieces and bonding them, thinning the specimen by mechanical grinding and polishing using sandpapers and lapping films, dimple grinding, and precision ion polishing. In this section, the preparation of cross-sectional samples from a silicon wafer is dis-

cussed. The same procedure applies to the substrates with as-synthesized nanowires with an additional step in the beginning to protect the nanowires on the substrate surface.

2.3.1 Cutting and Bonding

To prepare the cross-sectional sample, at first two pieces ($3 \text{ mm} \times 1 \text{ mm}$) of Si wafer (University wafer, ID 783) were cut using a diamond scribing pen. The thickness of the Si wafer was 500 microns with a layer of 1-micron thermal oxide. Cutting and bonding of the pieces are shown using schematic drawing in Figure 2.13. Two pieces were bonded facing each other using m-bond 610 adhesives (Ted Pella, product no. 16039), and good mechanical bonding [74] was obtained by holding the pieces and applying some pressure with a clamp (Ted Pella, product no. 813-542). A clamp is shown in Figure 2.13(e) holding the sample. Specific temperature and time are required for curing of resin (for m-bond 610, the recommended temperature range is 163-190 °C for 2-1 hours [75]). Alternately, bonded pieces are allowed to sit for 24 hours at room temperature. The second method was used in our sample.

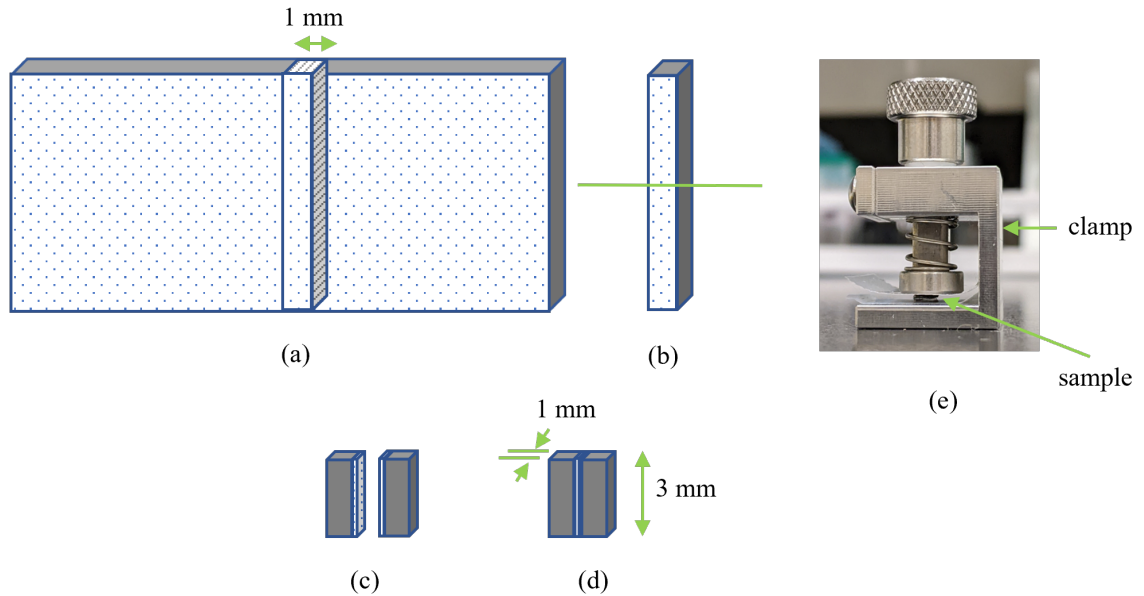


Figure 2.13: Schematic drawing of cutting and bonding process, not to scale. (a) A big piece of Si wafer (Dotted surface is to indicate thermal oxide layer), (b) a cut piece of 1 mm width from 2.1 (a), (c) two small pieces ($3 \text{ mm} \times 1 \text{ mm}$) obtained from 2.1 (b), (d) two pieces joined facing each other with m-bond, and (e) image of a clamp holding the joined pieces.

2.3.2 Mechanical Thinning by Grinding and Polishing

Grinding and polishing were performed in several steps. First, the sample was mounted on a tripod polisher (South bay technology, model 590) using a low melting point adhesive (crystalbond, Ted Pella, product no. 821-3) which melts at $121 \text{ }^\circ\text{C}$, and a hotplate. After that, the sample was ground using diamond/ aluminum oxide lapping films. Lapping films contain abrasive diamond/ aluminum oxide particles bonded with a resin onto a thin plastic film [76]. These films are available in the range of $30 \text{ }\mu\text{m}$ to $0.1 \text{ }\mu\text{m}$ particle sizes (Ted Pella) [77]. In our sample preparation, both types of films were used. Diamond films are more aggressive in grinding and have more longevity than aluminum oxide films [78].

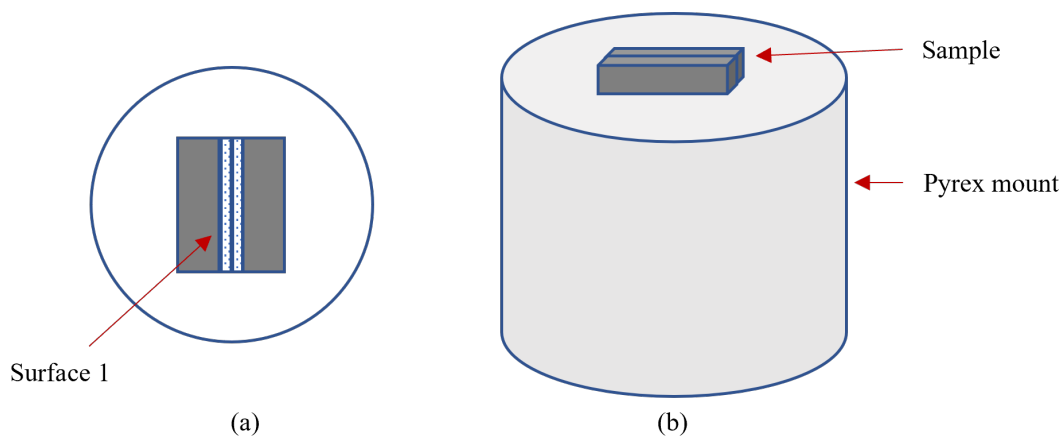


Figure 2.14: Schematic drawing (not to scale) of (a) top view of the sample on the mount of tripod polisher, and (b) the sample placed on top of a pyrex mount with crystalbond adhesive.

Only two cross-sectional side surfaces were required to be ground and polished. The red arrow in Figure 2.14(a) on the top surface indicates surface 1 and the opposite surface is defined as surface 2 here. Before grinding, both surfaces were rough and uneven from the slicing with the scribing pen. Surface 1 was ground with 30 μm lapping film to make that side flat. Then, the sample was taken off and flipped to grind surface 2 with 30, 15, 9, 6, 3, and 1 μm lapping films sequentially. After that, the sample was taken off from the tripod polisher, flipped, and attached on top of a pyrex specimen mount (Gatan, product no. 623.00082) to grind and reduce the thickness of the sample from the side of surface 1 (Figure 2.14(b)). Then the pyrex mount was placed on a disc grinder (Gatan, model 623). The sample was ground in the polishing wheel (Ecomet, model 250) using silicon carbide (SiC) sandpapers of 400, 600, and 800 grit sizes. The rotation speed of grinding was selected based on a trial and error method, starting with 130 rpm, and reducing the speed down to 100 and 80 rpm when the thickness of the sample reached close to 300 μm and 200 μm respectively. The disc grinder has a rotating knob with a scale that indicates the amount of grinding. Also, the thickness of the sample was approximately measured using the fine focus feature of an optical microscope (model Olympus BX51). When

the sample thickness is about 70-80 μm , the pyrex mount including the sample is taken off from the disc grinder and attached with the tripod polisher. Then, mirror polish of the sample was obtained by polishing with 9, 6, 3, and 1 μms lapping films and thickness was 60-70 μm . Grinding and polishing are very challenging when the sample thickness is below 100 μm . Therefore, it requires caution at each step of the processes mentioned above.

2.3.3 Dimple Grinding

The next step is dimple grinding in order to obtain a specimen thickness close to 20 μm . A dimple grinder (Gatan, model 656) was used for this purpose. Schematic drawing in Figure 2.15(a and b) shows the dimpling process and top view of the surface after dimpling. Pyrex cylinder including the sample was mounted on the stage of the dimple grinder and a grinding wheel (of phosphor bronze material) was mounted on the arm. To facilitate the grinding, a small amount of diamond polishing compound of particle size of 1 μm (Ted Pella, product no. 895-7-18) was applied on the specimen surface. Both wheel and specimen stage rotate in the directions as shown in Figure 2.15(a). Wheel rotational speed was set to the lowest setting and initially to avoid damage, 15 g of the load was applied to the specimen. Later, the load can be increased to 20 g. A dial indicator shows the amount of grinding, but it needs to be adjusted to zero before the start of dimpling [79]. After getting the desired thickness by grinding, polishing was performed by using a felt wheel, a diamond polishing compound of 0.5 μm particle size (Ted Pella, product no. 895-6-18), and at a higher speed than grinding for 20-25 minutes. At this step, scratches and other mechanical damages resulting from grinding could be removed and overall, a few microns of thickness reduction could be achieved by polishing. However, the micrometer and dial indicator cannot give a reading while using the felt wheel due to the softness of the felt. However, sample thickness could also be estimated using transmitted light because of the use of the transparent pyrex mount. The specimen

was observed at regular intervals using an optical stereo microscope associated with the dimple grinder. In the case of semiconductor materials, specimen thickness can be approximated easily by monitoring the color change of the specimen observed with transmitted light. For silicon, as thickness was being reduced, a small red color could be seen at the center of the dimpled area of the specimen, indicating thickness approaching $10\ \mu\text{m}$ [79]. It is essential to obtain this thickness with dimpling in order to optimize ion milling time. If it is thicker, ion milling takes a few hours longer than the estimated time. However, it required careful handling to prepare it for the next step, as the sample was too thin already. Figure 2.15(b) shows the top view of the specimen after dimple grinding. The dimpled area is specified using light gray color in the center of the specimen.

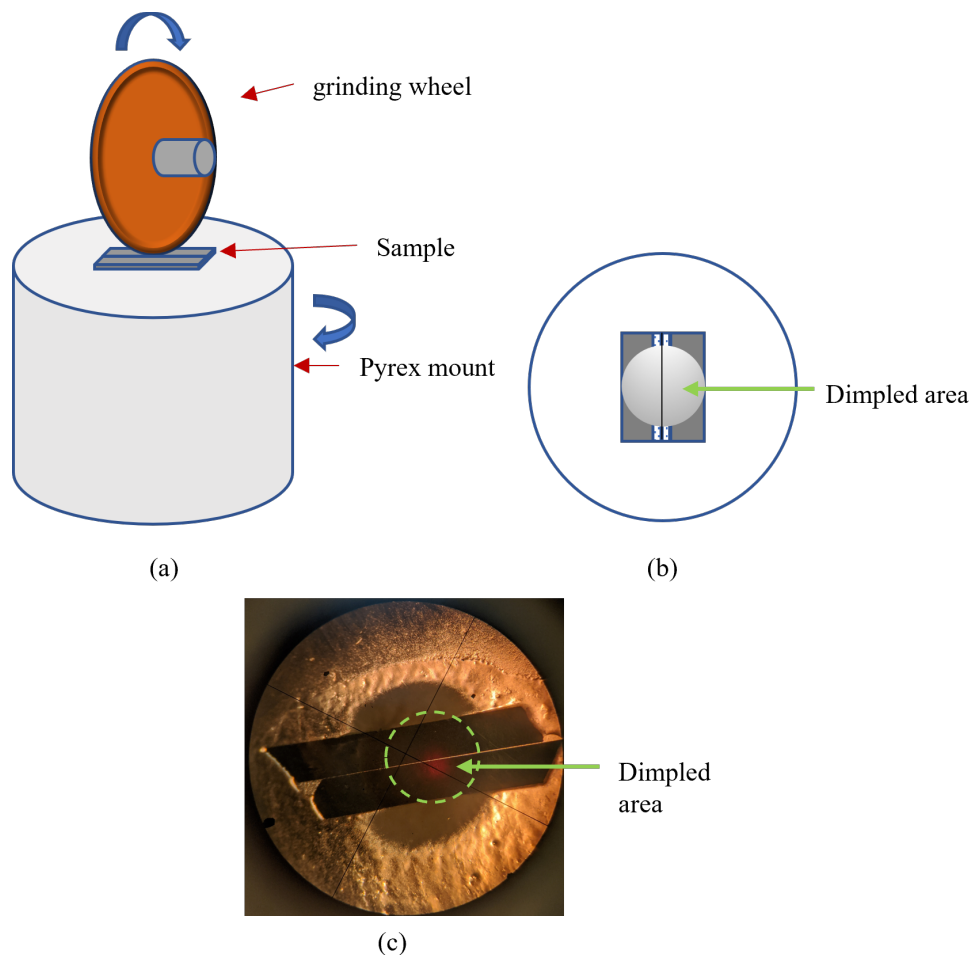


Figure 2.15: Schematic drawing of dimpling process. (a) Sample on the pyrex mount and a grinding wheel (blue arrows indicate the rotation direction of the sample stage and the grinding wheel), (b) top view of the sample after dimpling (light gray color in the center shows the dimpled area where thickness gradually reduces in the center), and (c) image of a sample after dimpling process taken from the eyepiece of the optical microscope (A small red color in the central dimpled area indicates sample thickness of about $10\ \mu\text{m}$. This can be observed using the transmitted light of the microscope.).

2.3.4 Precision Ion Milling

Ion milling is the final step of the sample preparation techniques. After dimpling was done, a molybdenum (Mo) ring was placed on top of the specimen surface using the m-bond and allowed to sit for curing (Figure 2.16(a)). After curing, the sample assembly was put into a beaker containing acetone. The acetone dissolved crystalbond in 10 minutes and separated the specimen (attached to Mo ring) from the pyrex

mount. Then the specimen was mounted on a holder and inserted in a precision ion polishing system (PIPS) (Gatan, model 691). In PIPS, Argon (Ar) ions were bombarded in the central area of the specimen from left (top) and right (bottom) ion guns alternately both at an angle of 5° . High voltage was kept at 5 keV to obtain a beam current of 20-25 μA , rotation of the sample mount was 3 rpm, and a dual beam modulator was selected to activate both ion guns. Due to ion bombardment, the center part of the sample started to lose atoms and became thinner. After starting milling, the specimen needed to be monitored after every 30 minutes. To monitor, there are two illuminators (reflection and transmission) associated with an optical stereo microscope in PIPS [80]. When a perforation was detected in the central region by the transmission illuminator, milling was stopped. After that milling parameters were changed: ion gun angle was reduced to 4° and the voltage to 3 keV to decrease the beam current to 10-12 μA and beam modulator was turned off, and a final polishing step for 5-10 minutes was carried out. This step helps to clean the specimen of any contamination or re-deposition. Figure 2.16(b) represents a schematic drawing of the top view of the specimen after milling. Small red arrows indicate the suitable spots for the observation in TEM.

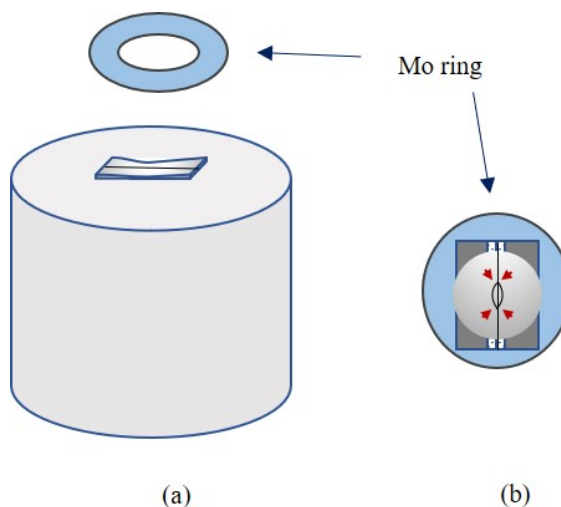


Figure 2.16: Schematic drawing of (a) attaching a Mo ring on top of the sample surface using m-bond, (b) top view of sample including Mo ring after ion milling. In an ideal case, a hole is created in the center due to ion milling. Four spots shown by red arrows are suitable for the TEM examination.

2.3.5 Challenges on Preparation of Nanowires-on-Substrate Cross-Sectional Sample

As mentioned above, mechanical grinding and polishing, and dimple grinding of the cross-sectional sample down to $\approx 10 \mu m$ is challenging. That is because the cross-sectional pieces are joined with m-bond adhesive. Although the adhesive has good strength and stability, it can disintegrate, and the pieces can be separated when the specimen is too thin and grinding is done at a relatively higher speed.

In the case of the nanowires-on-substrates, as an additional step, the surface is coated with a thin layer of m-bond to protect the nanowires from damage during slicing (Figure 2.17(a)). After that, the sample is prepared using the same techniques. However, due to this additional layer, the total thickness of the m-bond in the cross-sectional interface is relatively higher than the Si substrates without nanowires on it (Figure 2.17 (b) and (c)). That adds to the challenges during grinding, polishing, and dimple grinding. However, to solve the issue, the sample was coated with the m-bond to a minimum thickness by trial and error method. Also, the specimen was

ground and polished with a lower speed when it is thinner, and checked periodically to avoid over-grinding and polishing.

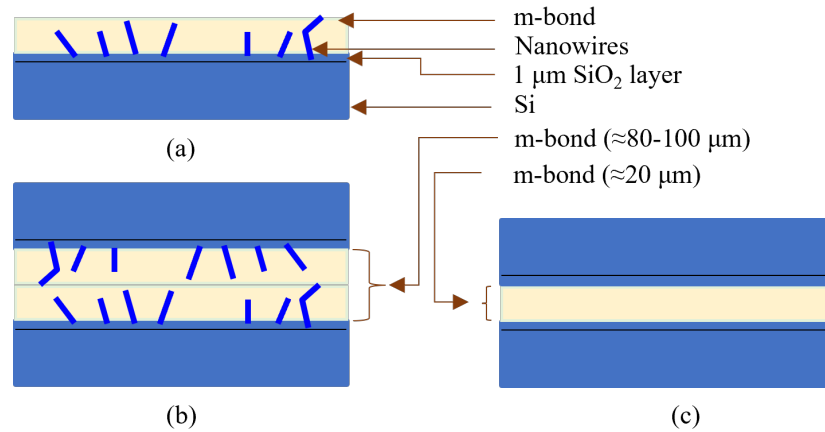


Figure 2.17: Schematic drawing (not to scale) (a) side view of a nanowires-on-substrate coated with m-bond, (b) side view of two pieces from (a) after joining them facing each other, and (c) side view of two pieces of substrates without nanowires on them. (b) has a thicker layer ($\approx 80\text{-}100\ \mu\text{m}$) compared to (c) ($\approx 20\ \mu\text{m}$) due to the initial step of coating to protect the nanowires on the substrates.

2.4 Software Tools

In this work, software tools such as CrystalMaker[®] and SingleCrystal[™], and imageJ were used. CrystalMaker[®] was used to construct the rhombohedral lattice structure of boron carbide and monoclinic structure of niobium selenide. For the construction, a crystallographic information file (CIF) or powder diffraction file (PDF) from International Centre for Diffraction Data (ICDD) database can be used. First, the new crystal was created manually by using the crystallographic information such as space group, lattice constants, and coordinates of atoms of a unit cell from PDF. After that bonds between atoms are specified, and crystal structure can be visualized using different models such as the polyhedral model, which is useful to see complex structures in a more comprehensible way.

SingleCrystal[™] was used to simulate electron DP in different zone axes/ viewing axes. Simulated DP could be compared with the experimentally obtained one. That

helped index the experimental DP as well as determine the feasibility of the same nanowire tilting to multiple zone axes. Also, using live rotation, both structure and DP can be viewed simultaneously from different viewing directions. Using ImageJ software, the dimension of nanowires was easily calculated, and DP was analyzed by measuring the distances of the diffraction spots from the central spot.

CHAPTER 3: MATERIALS CHARACTERIZATION OF NIOBIUM SELENIDE NANOWIRES

TEM analysis was performed to characterize niobium selenide (NbSe_3) nanowires to obtain structural information e.g., nanowire dimension, the thickness of the amorphous layer, preferred growth direction, etc. It was collaborative work with researchers from Vanderbilt University and Pennsylvania State University. The motivation was to understand the structure-property relationship such as the correlation between the lattice constants, dimension, and mechanical and thermal properties of the NbSe_3 nanowires.

3.1 Background Information

In this section, background information of the work, such as the importance of NbSe_3 crystal, crystal structure, preparation, and results from preliminary examinations, is discussed.

3.1.1 Significance of Niobium Selenide (NbSe_3) for Distinct Signatures of Electron-Phonon Coupling

Understanding the effect of electron-phonon (e-ph) interactions in solids is extremely important. Various physical phenomena such as superconductivity and charge density waves are attributed to such an effect. The effect of e-ph interaction on electrical conductivity has been extensively studied and contributes to the electrical resistance [81, 82]. A similar effect on thermal conductivity is also speculated, but quantitatively determining that consequence is very challenging because of electron- and phonon-dominant transport in metals and semiconductors respectively. To determine the effect of e-ph coupling on thermal conductivity, heavily doped semicon-

ductors have been investigated. However, it is extremely challenging to differentiate the contribution of e-ph interaction from the other types of scattering mechanisms at higher temperatures. To resolve this issue, a suitable material that demonstrates distinct signatures T^{-1} temperature dependence for Umklapp scattering is required. Yang et al. have demonstrated such evidence for NbSe₃ nanowires [81].

NbSe₃ is known as van der Waals (vdW) materials because of its molecular chains joined together via vdW force. Due to their chain-like structure, free electron density changes with temperature in a wave-like manner below a specific critical temperature (T_{CDW}). This phenomenon is called charge density waves (CDW). At the onset of the CDW, variation of electron density modulates the e-ph scattering strength and affects lattice thermal conductivity significantly [81]. For this purpose, niobium selenide quasi-one-dimensional nanowires were chosen to demonstrate the effect experimentally.

3.1.2 Crystal Structure of Niobium Selenide (NbSe₃)

NbSe₃ has a monoclinic crystal structure with lattice constants, $a = 10.008 \text{ \AA}$, $b = 3.4805 \text{ \AA}$, $c = 15.629 \text{ \AA}$ and $\beta = 109.47^\circ$. A simulated crystal structure of NbSe₃ is presented in Figure 3.1 as projections from two viewing directions. NbSe₃ is composed of trigonal prisms with six selenium (Se) atoms at the corners and a niobium (Nb) atom at the center of each prism. These prisms form infinite chains along the b axis by stacking on top of each other and sharing triangular faces as can be seen in Figure 3.1 (a) [83]. In a unit cell, NbSe₃ contains three types of chains based on the Se-Se bond lengths [84], type I, II, and III. Figure 3.1 (b) represents a projection of the unit cell of the crystal structure perpendicular to the b axis. So, the unit cell consists of six chains containing a pair of each type of chain. Type II chain is rotated by $\approx 180^\circ$ with respect to type I and type III chain is rotated by $\approx 40^\circ$ with respect to type II [83]. Due to this chain-like structure along the b axis, NbSe₃ exhibit anisotropy in most of their physical and chemical properties [84].

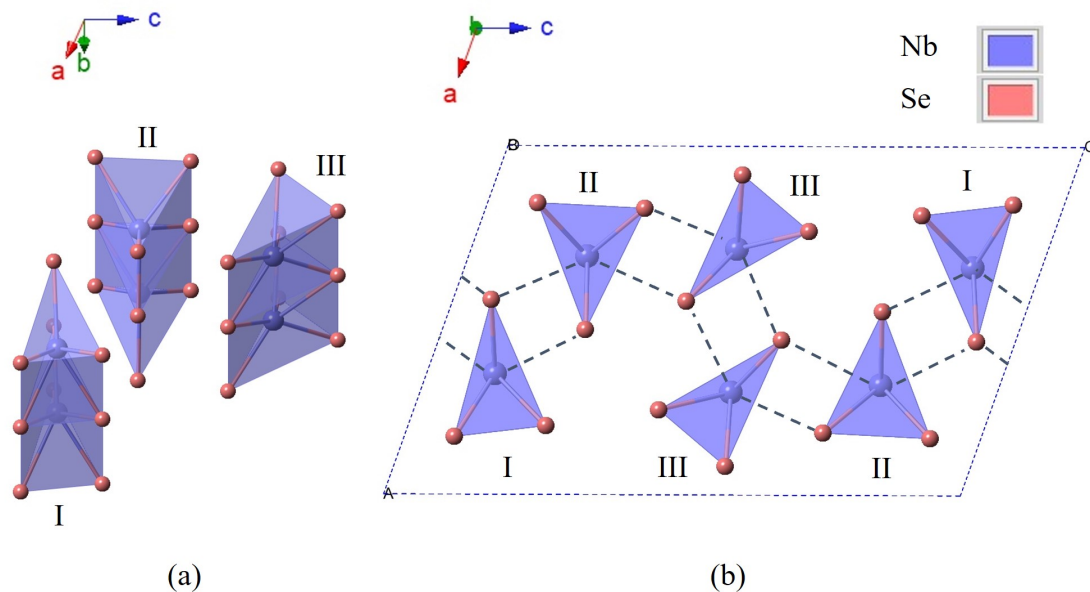


Figure 3.1: Simulated crystal structure of NbSe₃ using CrystalMaker[®] projected from two viewing directions (a) exhibiting chains of trigonal prisms along *b* axis, and (b) unit cell consisting of six chains projected perpendicular to the *b* axis.

As mentioned above, three types of chains are formed corresponding to different Se-Se bond lengths. Within the chains, Nb is bonded to six Se. These intrachain bonds are of covalent-ionic nature. Figure 3.2 is presented to better visualize the intra- and interchain bonding. Figure 3.2 (a) presents three chains along *b* axis and the length of the prism (same as the length of the unit cell) along this axis is indicated by *b*. From the figure, the prism of one chain is displaced by $b/2$ with respect to the prisms of the adjacent chains. This displacement results in additional Nb-Se bonds between neighboring chains along the *c* axis. The bond length of interchain Nb-Se is comparable to the average of the intrachain Nb-Se bonds and those bonds are also mostly of covalent-ionic type. Interchain Nb-Se bonds are specified as green dashed lines both in Figure 3.2 (a) and (b). Due to these interchain bonds, 2D infinite slabs are formed in the *bc* plane with the shortest dimension along the *a* axis (two chains thick) (Figure 3.2 (b)). Two adjacent slabs are connected together via van der Waals (vdW) bonds along the *a* axis. Because of this, NbSe₃ is also considered a layered or

2D compound [83].

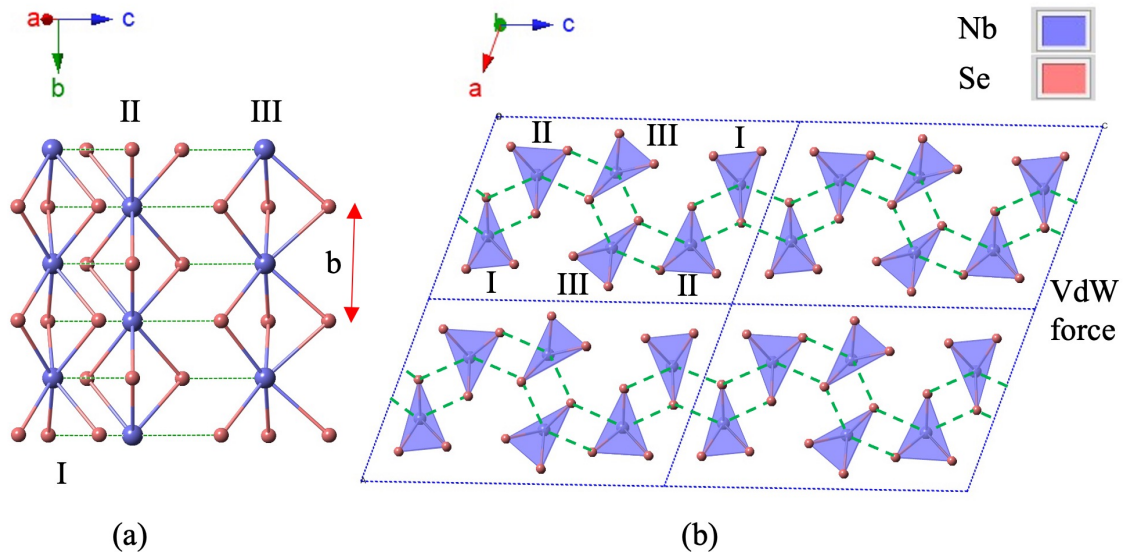


Figure 3.2: Simulated crystal structure of NbSe₃ using CrystalMaker[®].

Intrachain bonds are much stronger than vdW bonds between slabs and interchain Nb-Se bond lengths along the c axis vary in a large range compared to intrachain Nb-Se bonds, resulting in easy cleavages parallel to the ab and bc planes. Because of these easy cleavages, ultrathin NbSe₃ nanowires and fibers can be prepared easily [83].

Due to the above-mentioned structural anisotropy, NbSe₃ exhibits unusual electrical properties along the b axis. With the reduction of temperature, electrical resistivity reduces with two giant anomalies at 145 K and 59 K, where resistivity abruptly increases, reaches a maximum, and then continues to decrease with temperature showing metallic behavior. The anomalies are attributed to the formation of charge density waves (CDW). CDWs are formed because of the condensation of electron gas density into a superstructure with a different periodicity compared to that of the structure. The formation of CDWs has been confirmed by incommensurate superlattice spots in the electron diffraction experiment [83]. Condensation of electron density occurs due to structural distortion. For NbSe₃, the first CDW

formation at 145 K is assigned to the atomic displacements in the type III chain and the second CDW is assigned to the type I chain. Type II chain remains unaffected and is responsible for NbSe₃ to be partially metallic at low temperatures [85].

3.1.3 Preparation of NbSe₃ Nanowires

NbSe₃ crystal was synthesized by the collaborator at Pennsylvania State University. At first, bulk NbSe₃ single crystals were grown in a chemical vapor transport (CVT) system [81]. In this system, usually, a solid phase reactant is kept in one region (charge end) and is volatilized and transported by a gaseous reactant (transport agent) where crystallization occurs in another region (cold end). The process is carried out by creating a temperature gradient. Usually, a higher temperature is kept at the charge end to facilitate the volatilization of the reactants, and a relatively lower temperature is maintained at the cold end where the crystals are deposited [23].

A uniform mixture of Nb and Se powders was prepared by mixing in a stoichiometric ratio of 1:3 and grinding. The mixture was loaded into a quartz tube and sealed under a vacuum. The sealed tube was placed in a horizontal double zone furnace and temperatures at the charge and cold end were raised to 800 °C and 700 °C, respectively. Long ribbon-like NbSe₃ single crystals grew after two weeks at the charge end or in the center of the quartz tube [81].

As mentioned in the previous subsection, due to weaker inter-chain bonding strength than intra-chain bonds, NbSe₃ nanowires can easily be cleaved along the *bc* and *ab* planes. In our case, ultra-thin nanowires were prepared by liquid exfoliation. Reagent alcohol was used to immerse bulk NbSe₃ whiskers, and sonicating for three hours resulted in a nanowires suspension with various cross-sectional sizes. Finally, nanowires suspension was drop cast on a polydimethylsiloxane (PDMS) substrate, and individual nanowires were transferred from the PDMS to a TEM grid using a custom-built micromanipulator [81].

3.1.4 "Routine" Materials Characterization and Understanding of Electron-Phonon Interaction

The as-prepared NbSe₃ nanowires were subjected to structural characterization to understand the electron-phonon interaction of the material. Initially, individual nanowires were examined using TEM to obtain DP, HRTEM, and corresponding low-magnification images. A total of fifty nanowires were examined and the representative results are presented in Figure 3.3. Figure 3.3 (a) shows a low magnification image of a NbSe₃ nanowire on the TEM grid. The nanowire is indicated by a red arrow. The inset includes an intermediate magnification image from the location pointed by a red rectangle, which shows the width of the nanowire as ≈ 77 nm. HRTEM image from the same location is presented in Figure 3.3 (b) along with the corresponding DP in the inset. The molecular chain structure along with a thin amorphous layer (3.3 ± 0.3) is clearly visible from the HRTEM image. The DP indicates the single crystallinity of the as-prepared nanowires. DP was analyzed and the zone axis was determined to be [100]. Due to the easy cleavages as mentioned above, the preferred growth direction of most of the prepared NbSe₃ nanowires is perpendicular to the (020) planes and could easily be observed parallel to the *b* axis.

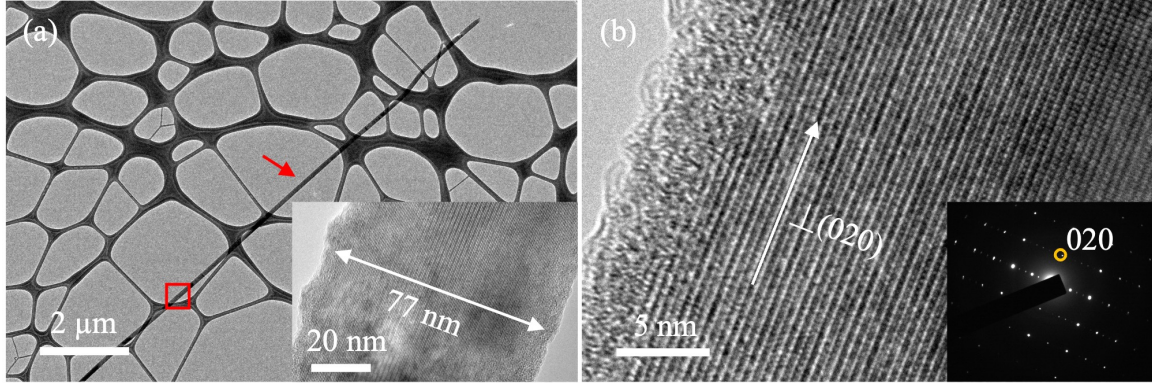


Figure 3.3: TEM results of a representative NbSe_3 nanowire. (a) The low-magnification image shows a nanowire on the TEM grid (indicated by a red arrow). The inset presents a zoomed-in TEM image of the location pointed by a red rectangle. (b) HRTEM image shows a single crystalline core with a 3.3 ± 0.3 nm thick amorphous layer. Inset includes corresponding DP along $[100]$ zone axis. The preferred growth direction of the nanowire is perpendicular to the (020) planes.

Electrical and thermal conductivity and Seebeck coefficients of the NbSe_3 were measured by the collaborator at Vanderbilt University using a microthermal bridge approach [81]. In this approach, nanowires were placed between two SiN_x membranes by locally depositing Platinum (Pt)/Carbon (C) via electron-beam-induced deposition. The membranes have integrated Pt resistance thermometers (which also act as a microheater) to measure thermal conductivity, and extra Pt electrodes to facilitate measuring electrical transport properties simultaneously. Nanowires prepared via liquid exfoliation tend to be of irregular cross-sections, which are examined using focused ion beam directly [86]. Nanowire size is defined by hydraulic diameter (D_h), (four times the reciprocal of the surface area to volume ratio), which has been shown to better characterize the size effects in case of irregular cross-sectional nanowires [87]. Figure 3.4 (a), (b), and (c) shows electrical resistance (R), Seebeck coefficient (S), and thermal conductivity (κ) measured from a NbSe_3 nanowire of $D_h = 135$ nm in the temperature range 15-300 K. From the measured data, R decreases with decreasing temperature above 145 K and shows anomalies starting at 145 and 59 K, where R increases with decreasing temperature, reaches maxima at 130 and 43 K respectively

and decreases again. This is due to the CDW phase transition as discussed in section 3.1.2. The amplitudes of the two maxima match with those reported for bulk NbSe₃ [81].

From Figure 3.4(b), measured S with temperature shows a similar trend as bulk NbSe₃ including the anomalies at the CDW transition temperatures. Based on the measured S , Lorenz number (L) is derived from the solutions to the Boltzmann transport equation and used in the Wiedemann-Franz law ($\kappa_e = LT\sigma$, where T and σ denote absolute temperature and electrical conductivity) to calculate electronic contribution to the thermal conductivity (κ_e). Lattice thermal conductivity (κ_{ph}) can be found by subtracting (κ_e) from the total thermal conductivity (κ_t). Figure 3.4 (c) shows κ_t , κ_e and κ_{ph} in the same plot [81].

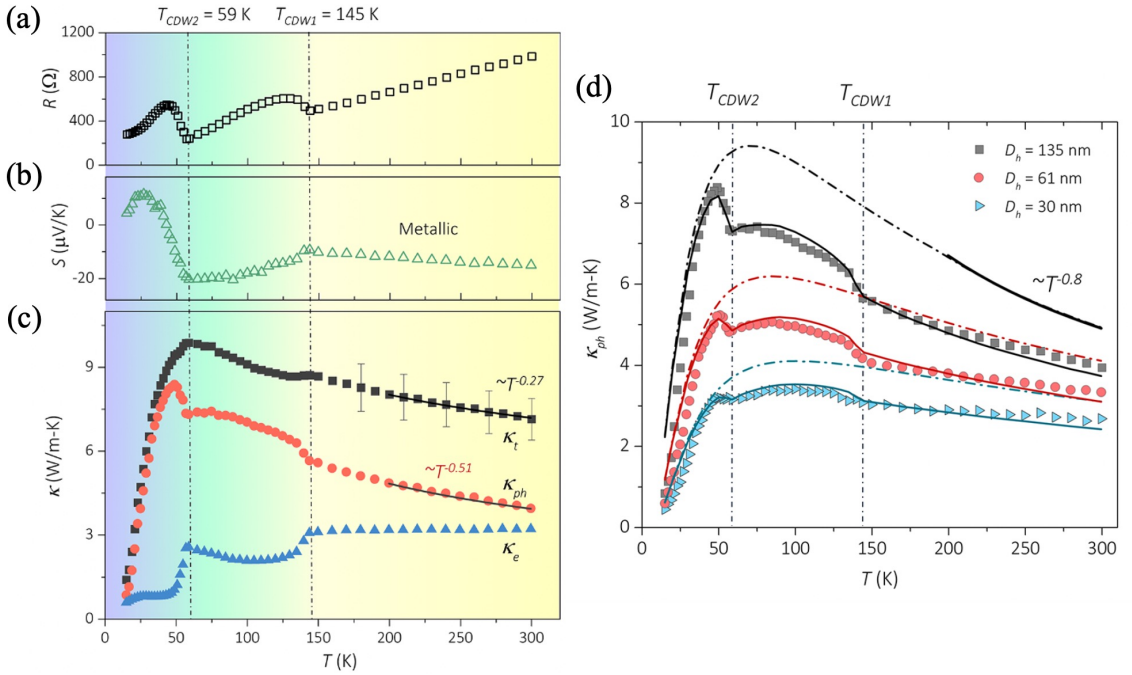


Figure 3.4: Results from electrical and thermal measurements. (a) Electrical resistance, (b) Seebeck coefficients, and (c) thermal conductivity against the temperature (15-300 K) measured from a 135 nm NbSe₃ nanowire. (d) Comparison between modeling results and experimental lattice thermal conductivity of NbSe₃ nanowires of three different sizes. Fitted results are represented by dashed and solid lines without and with considering the e-ph scattering effect respectively [81].

From Figure 3.4 (c), κ_t shows two local maxima at the CDW transition temperatures. κ_e drops at the two T_{CDWS} due to the electron condensation and contributes to the reduction of κ_t . κ_{ph} also shows abrupt changes but opposite trend than that of κ_e at the two T_{CDWS} . This coincidence of both κ_e and κ_{ph} at the transition temperature indicates the change in κ_{ph} is due to the change in free electron concentrations. The opposite trend in κ_e and κ_{ph} strongly suggests that e-ph scattering is responsible for the anomalies in κ_{ph} [81].

Despite having the quasi-1D structure of NbSe₃, a clear size dependence could be observed for electrical resistance, κ_e and κ_{ph} . For nanowires with D_h lower than the mean free path (MFP) of the electron, electrical resistance and κ_e both are reduced due to additional electron boundary scattering. Also, phonon boundary scattering increases for smaller-diameter nanowires. To further understand the effect of different factors on the κ_{ph} , first principle calculations were combined with phenomenological models and fitted with the experimental data. Modeling results (Figure 3.4(d)) show that without considering e-ph interaction, κ_{ph} shows a smooth profile in the entire temperature which is characteristic of bulk crystalline materials. But considering e-ph interaction the modeled κ_{ph} fit greatly with the distinct signatures in κ_{ph} in the experimental data [81].

3.1.5 Anomalous Thermal Transport in Ultrathin Nanowires

Further measurement revealed anomalous thermal conductivity in ultrathin NbSe₃ nanowires, which has been predicted for different types of ultrathin 1D and 2D lattices but without experimental validation. Measured κ and its size and temperature dependence is briefly discussed here (κ is used to denote total thermal conductivity in this section). First, κ measured at room temperature was analyzed with respect to D_h of each nanowire and presented in Figure 3.5 (a). For this analysis, the suspended length of all nanowires was kept to $\approx 15\mu\text{m}$. From the figure, a clear transition at $D_h=26$ nm can be seen. κ decreases with decreasing D_h until 26 nm due to increased

boundary scattering of 3D phonons. But further decrease results in a rapid increase in κ (≈ 25 -fold for nanowire with $D_h=6.8$ nm) [88].

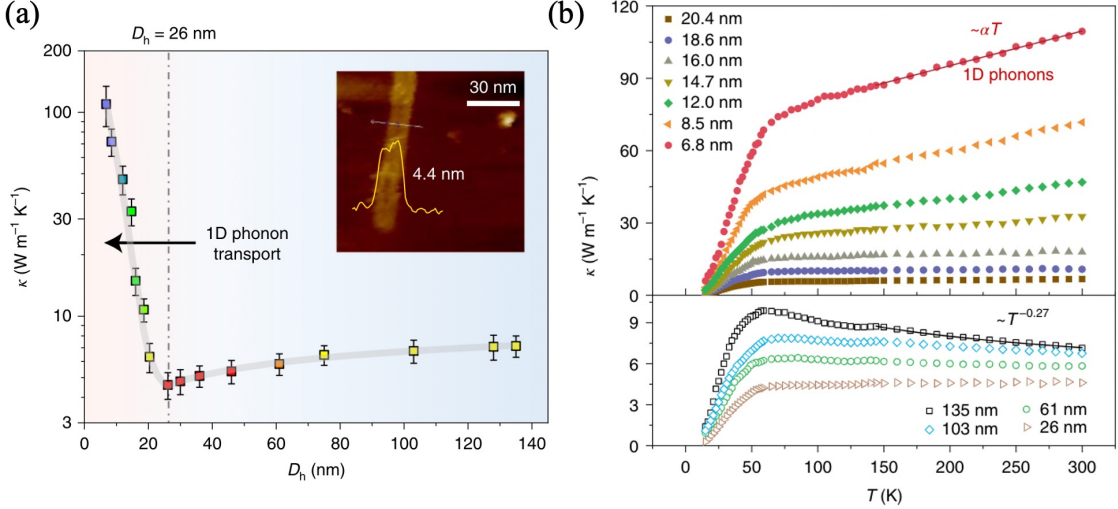


Figure 3.5: (a) Room temperature thermal conductivity, κ versus nanowire hydraulic diameter, D_h (b) κ versus temperature for different hydraulic diameter, D_h . The bottom panel in (b) shows the temperature dependence of thicker nanowires ($D_h \geq 26$ nm) and the top panel shows the results for ultrathin nanowires ($D_h < 26$ nm) [88].

As bulk NbSe_3 is metallic, thermal conductivity due to electron transport (κ_e) must be taken into consideration. κ_e was estimated using Wiedemann-Franz law as discussed in the previous section. The electronic contribution was found to be 42% for the nanowire with $D_h=24$ nm at 300 K. But with decreasing D_h , electronic contribution reduced rapidly to 3% for $D_h=10.8$ nm. This indicates that mainly phonons are responsible for the drastic enhancement of κ for ultrathin NbSe_3 nanowires [88].

Length dependence of κ was also measured by using the same nanowire with different suspended lengths (L). In case of thicker nanowires ($D_h > 26$ nm), κ increases with increasing L in the range ≈ 2 to $\approx 6 \mu\text{m}$. With a further increase of L , κ converges to a saturated value. This indicates the transition of phonon transport from a ballistic to a diffusive mechanism. The transition occurs because of L exceeding phonon MFP. But for even longer suspended lengths and thinner nanowires measured κ follows $1/3$ divergence law with increasing L . For phonons, a divergent κ is usually

associated with ballistic transport. But despite showing length dependence, ballistic transport does not follow the trend $\kappa \propto L^{1/3}$ for a large length range. Also, the length dependence of κ is consistent at two very different temperatures, 300 K and 100 K. If partially ballistic phonon transport was involved, the slope would be steeper at 100 K, as the MFP of phonon is larger at lower temperatures. This consistent 1/3 power-law length dependence at different temperatures indicates superdiffusive transport of 1D phonons [88].

The transition of phonon transport is also supported by the temperature dependence of κ for nanowires with different D_h (Figure 3.5(b)). For $D_h \geq 26$ nm, κ show temperature dependence varying from $T^{-0.03}$ to $T^{-0.27}$ in the range 50-300 K, indicating Umklapp scattering. But for $D_h < 26$ nm, κ shows an increasing trend in the same temperature range, and for $D_h=6.8$ nm wire, temperature dependence is linear. This trend is drastically different than the thicker nanowires and suggests that phonon modes must be different for ultrathin nanowires. Moreover, thickness dependence could also be observed for the measured Young's modulus (E). Below $D_h < 26$ nm, E increased significantly, and up to a fivefold increase was obtained for the nanowire of $D_h=8.9$ nm [88]. This substantial increase in E compels us to look into the structural parameters as E is correlated with the bond length which can be associated with lattice parameters and thickness of the nanowires [89].

To determine whether any correlation exists between anomalous thermal and mechanical properties and lattice constants of ultrathin nanowires, individual nanowires of different diameters were examined using TEM. Experimental details of TEM examination, calculation, challenges in the measurement, and results are discussed below.

3.2 Determination of Lattice Constants of NbSe₃ Crystal

Lattice constants of a crystal can be determined by solving the planar spacing equation for that specific crystal structure. In this section, the planar spacing equation for the monoclinic crystal structure, the necessity of results from multiple zones, issues

in obtaining the desired results, an approach to resolving the issues, and obtained results are discussed.

3.2.1 Solving Planar Spacing Equation for NbSe₃ Lattice

Theoretically, planar spacing, d of a monoclinic lattice can be measured by using the following equation for a specific plane (hkl).

$$\frac{1}{d_{hkl}^2} = \frac{1}{\sin^2 \beta} \left(\frac{h^2}{a^2} + \frac{k^2 \sin^2 \beta}{b^2} + \frac{l^2}{c^2} - \frac{2hl \cos \beta}{ac} \right) \quad (3.1)$$

Where, a , b , c , and β are four lattice constants for the monoclinic crystal. Using equation 3.1, lattice constants can be calculated from the experimentally obtained electron DPs. For this purpose, first, the DPs are required to be indexed as mentioned in subsection 2.1.2.1. To solve four unknown lattice constants, four equations are required. So, four sets of (hkl) and d values are required. As can be seen from equation 3.1, it is a non-linear equation. Due to the complexity of the equations obtained after plugging in the (hkl) values, four equations are solved using analytical methods.

3.2.2 The Need of Results from Multiple Zones and Challenges in Tilting

During TEM examination, it is essential to view the nanowires along the low-index zone axes. This allows the collection of more DP spots of low hkl values, which then helps to determine unknown lattice constants easily, especially for such a complex lattice as a monoclinic structure. Figure 3.6 (a) shows a schematic drawing of the monoclinic crystal structure of NbSe₃. In the figure, two shaded areas represent (001) and (100) planes. Within the (001) plane, two vector directions in red color are shown to indicate zone axes [100] and [110]; outside that plane, another zone axis [$1\bar{1}1$] is shown in blue color (to draw vector direction [$1\bar{1}1$], the origin is moved from o to o' , as the vector is in another plane). The schematic drawing helps to visualize the zone axes, which is required for the discussion in this section. As mentioned earlier, the

preferred growth direction and the molecular chain alignment in the NbSe₃ nanowires are along the y-axis. So, the lowest index zone axis obtainable from the NbSe₃ nanowires lies either in the (001) or (100) plane.

As discussed in section 3.2.1, four different sets of (hkl) values (i.e., four different diffraction spots) are required to calculate the unknown lattice constants of NbSe₃ monoclinic structure. After indexing an electron DP, usually, only two or three different diffraction spots can be obtained. This is demonstrated in Figure 3.6 (b), (c), and (d) using simulated DPs obtained from SingleCrystal™ software. All other diffraction spots represent symmetrically equivalent planes in the lattice, resulting in equivalent equations.

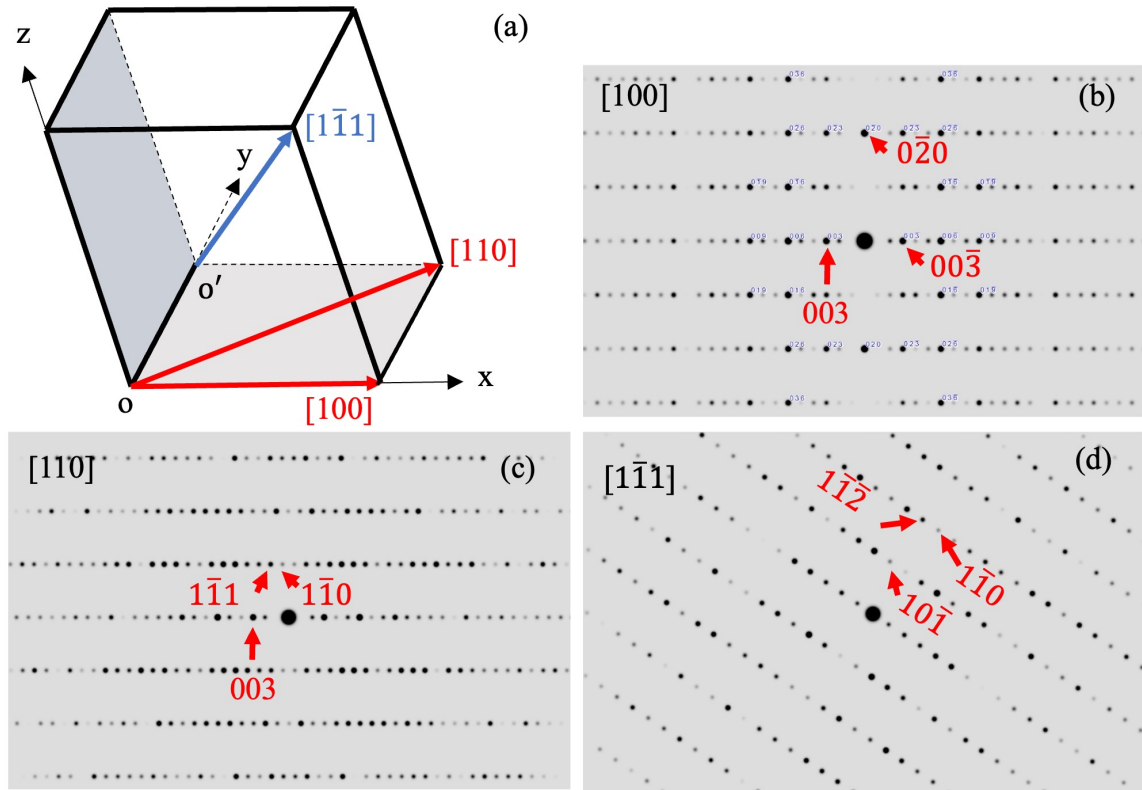


Figure 3.6: (a) Schematic drawing of monoclinic crystal structure. Two shaded areas represent (001) and (100) planes. Within the (001) plane, two zone axes are shown by red arrows. The blue arrow represents another zone axis outside the (001) plane. (b), (c), and (d) Simulated diffraction patterns from the zone axes $[100]$, $[110]$, and $[1\bar{1}1]$ respectively. From each zone axis, two or three different diffraction spots (hkl) can be obtained. All other spots provide equivalent equations because of the presence of symmetrically equivalent planes in the lattice.

For example, from Figure 3.6 (a), two different spots 003 and $0\bar{2}0$ can be obtained from the zone axis $[100]$. If the sample is tilted from this zone axis to $[110]$, three spots 003 , $1\bar{1}1$ and $1\bar{1}0$ can be obtained as shown in Figure 3.6 (b). If these hkl values are plugged into equation 3.1, three unique equations can be derived instead of four because of the repeated hkl values and nonlinearity of the equation. $[110]$ and $[100]$ directions are within the same plane (001) (Figure 3.6 (a)); hence, they are in-plane zone axes. To obtain unrepeated hkl values and four unique equations, two out-of-plane zone axes, such as $[100]$ and $[1\bar{1}1]$ or $[110]$ and $[1\bar{1}1]$, are required. Simulated DP along $[1\bar{1}1]$ is shown in Figure 3.6 (c).

However, it is challenging to obtain a pair of out-of-plane zone axes. Due to the crystal structure and easy cleavages along the ab and bc planes, as-prepared NbSe_3 nanowires can be easily tilted to the first low index zone axis such as $[100]$ or $[001]$. Tilting from that axis to an in-plane zone axis is easier than to an out-of-plane zone axis because of two main reasons. First, the tilting angle is limited in our TEM to $\approx 60^\circ$, which is comparable to most TEM holders. Secondly, the initial orientation of the nanowires is random before examining them using TEM. So, tilting from the random orientation to the first low zone axis, and then tilting to the out-of-plane zone axis require large-angle tilting. To overcome this issue, the initial orientation of an individual nanowire can be changed by picking it up from the TEM grid by using a micromanipulator probe and re-positioning the same nanowire onto the grid. This allows a full range tilting and obtaining of two out-of-plane zone axes for the same nanowires. However, this process is tedious if it needs to be repeated for each nanowire. An alternative approach was developed by Guan et al. [61] to estimate the tilting possibility to the desired zone axes for boron carbide nanowires using CrystalMaker[®] and SingleCrystal[™] software. A similar approach is developed and used for NbSe_3 nanowires, as discussed below.

3.2.3 Construction and Utilization of DP Roadmap

Inspired by the work done on the boron carbide nanowires [61], a roadmap is developed using simulated DPs from NbSe_3 nanowires as shown in Figure 3.7. A circle is divided with lines to indicate different zone axes. DPs are simulated based on the experimentally obtained zone axes, and theoretical angles between them are calculated and used to construct the roadmap. It helps us decide whether further tilting and obtaining desired out-of-plane zone axes is possible. For example, the angle between $[100]$ and $[1\bar{1}1]$ is 72.4° , which is beyond the tilting limit of our TEM. Therefore, it is not possible to tilt the nanowire from $[100]$ to the $[1\bar{1}1]$ direction. Similarly, samples cannot be tilted from $[110]$ to the zone axis $[1\bar{1}1]$ because of their

three different planes. As these angles are projected on the roadmap in Figure 3.7, the angle between $[110]$ and $[1\bar{1}1]$ seems smaller than that of $[100]$ and $[1\bar{1}1]$. Also, because of the same reason, the angle between $[100]$ and $[110]$ (19.2°) does not match with the calculated angle (5.3°) from the roadmap based on their corresponding angles with the $[1\bar{1}1]$.

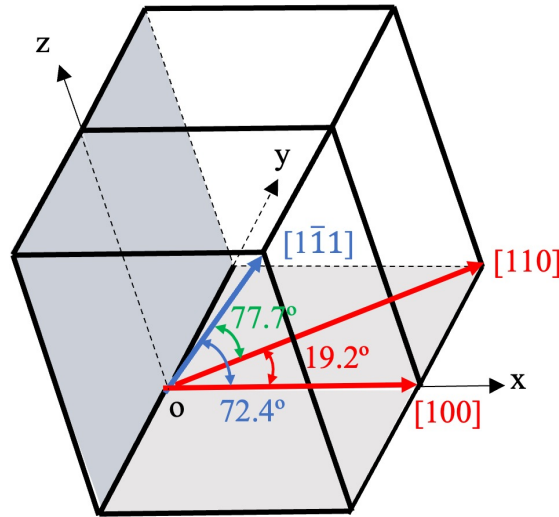


Figure 3.8: A schematic diagram for NbSe_3 monoclinic crystal structure consisting of two unit cells. Three vector directions are shown to indicate three zone axes from a common origin (o), and angles between them are shown to visualize the angles projected on the roadmap in Figure 3.7. As they are not in the same plane, it is not straightforward to calculate the angles based on the roadmap.

Despite the issue of the pseudo roadmap, it helps us determine the tilting possibilities and provide other available zone axes within the tilting limit during the TEM examination. As a result, it facilitates acquiring DP and HRTEM images from multiple zones, which is otherwise a tedious and lengthy process.

3.2.4 Results

As mentioned in the section 3.1.1, the goal is to correlate the lattice constants and the diameter/ width of the nanowires. The approach and challenges to obtaining four lattice constants have been discussed in the previous sections. Due to those challenges, four lattice constants could be determined from seven out of total of fifty

nanowires examined in several batches. Nanowire width can be measured from the TEM image as shown in Figure 3.3 (c). Usually, DP, HRTEM, and relatively lower magnification images (to fit the width of the nanowires) are recorded at the same location of the nanowires.

Four lattice constants are presented in Figure 3.9 against the nanowire width. Theoretical values of the lattice constants are also presented in each plot.

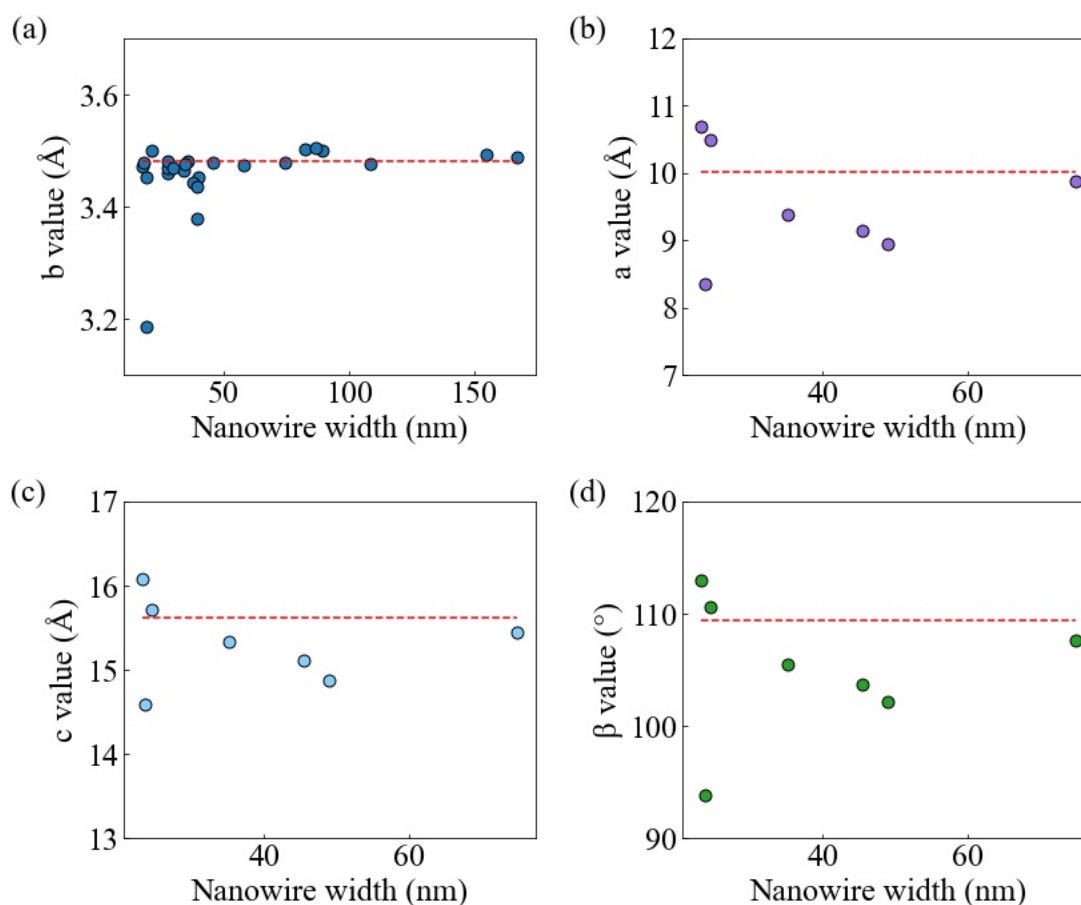


Figure 3.9: (a), (b), (c) and (d) Experimental lattice constants b , a , c and β with respect to the nanowire width measured from TEM images. The dashed lines represent theoretical values for bulk NbSe₃. Uncertainty of the lattice parameters and nanowire width can be correlated to the uncertainty in the d-spacings measured from the diffraction patterns, and TEM images respectively. Thus, uncertainties in the x and y axes were estimated to be <1% and <2%.

From Figure 3.9 (a), more data points could be obtained for b values. That is

because b values could be directly calculated from those zone axes that provide the spot 020.

From Figure 3.9 (a), (b), (c), and (d), no significant trend correlating the lattice constants and nanowire width can be observed. For example, based on the data plotted in Figure 3.9 (a), variation in nanowire width (difference between maximum and minimum value) of 150 nm results in variation in b value of 0.125 Å, and variation in b value around the mean b value is 3.6%. Horizontal dashed lines were plotted to represent the theoretical value of each parameter. Experimental data is close to the literature values. This also verifies the independence of the lattice constants with the nanowire width.

So, the change in lattice parameters is not significant enough to affect the superdiffusive phonon transport. Also, the positive and linear temperature dependence of κ for ultrathin nanowires (Figure 3.5(b)) cannot be explained by variation in phonon MFP or group velocity. As $\kappa \approx C\nu l$ (where C , ν , and l represent heat capacity, phonon MFP, and group velocity), the transition must be due to the change in heat capacity with temperature variation, and the phonon modes must also be different in case of ultrathin nanowires compared to those of the thicker nanowires. In section 3.1.5, 1D phonon modes were suggested from a 1/3 divergence trend in a large length range and at different temperatures. Positive temperature dependence of κ (Figure 3.5(b)) can be explained by the enhancement of 1D phonon modes along the molecular chains. This is possible only if the Debye temperature value increases. Higher Debye temperature results in increasing Young's modulus (E). This phenomenon is known as elastic stiffening. As mentioned before, E was observed to increase significantly for $D_h < 26$ nm. Individual nanowires were measured along the b direction using a three-point bending method with an atomic force microscope (AFM), and E was extracted from the obtained force-deflection curve [88]. Measured E versus D_h plot is presented in Figure 3.10.

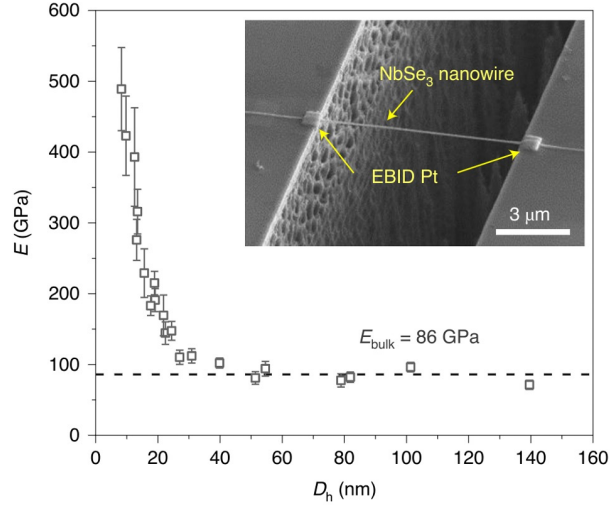


Figure 3.10: E is plotted against D_h with average bulk value (E_{bulk}) shown as dashed line. The inset shows an SEM image of a NbSe_3 NW bridging a Si trench. The NW is clamped to the substrate by locally depositing Pt at the two edges by electron beam induced deposition (EBID) [88].

From the figure, it can be seen that E is constant for nanowires with $D_h > 40$ nm. But for D_h below 26 nm, E increases sharply, and fivefold enhancement could be observed for the nanowire of $D_h = 8.9$ nm. Increased E value corresponds to a higher speed of sound, which is directly related to the κ_{ph} . Also, higher Debye temperature contributes to the reduction of Umklapp scattering by moving the phonon spectrum to a lower wave vector, and by extending the bandgap between acoustic and optical phonons. All these factors contribute to the superdiffusive transport by enhancing κ_{ph} [88].

3.3 Summary

Experimental evidence of the e-ph scattering effect on lattice thermal conductivity of quasi 1D NbSe_3 nanowires was demonstrated by Yang et al. [81]. Also, significant enhancement of the thermal conductivity for ultra-thin NbSe_3 nanowires was reported [88]. To correlate the enhancement of the property with the lattice constants, fifty NbSe_3 nanowires were characterized individually using TEM. Each nanowire was

tilted to multiple zone axes, and HRTEM images and DPs were recorded from each zone axes. The challenges to tilt the nanowire sample to the desired out-of-plane zone axes were resolved by constructing a DP roadmap. However, after data visualization and interpretation, no correlation between nanowire width and lattice constants could be established. So, the enhancement of the thermal conductivity was not due to the change in the structural parameters with decreasing diameter/ width of the nanowires. The major gains from completing this collaborative work are establishing the method to calculate lattice constants of a complicated monoclinic structure from DPs acquired from multiple zone axes, overcoming the challenge of obtaining desired data, and data validation by using the calibration sample. All these methods are reproducible and applicable to TEM analysis of other types of materials.

CHAPTER 4: GROWTH MECHANISM OF BORON CARBIDE NANOWIRES

TEM analysis was performed to explore the growth mechanism of boron carbide nanowires. The motivation was to obtain the rational synthesis of boron carbide nanowires with improved thermoelectric performance. This chapter discusses the background information of boron carbide nanowires and results from routine and cross-sectional examinations.

4.1 Research Status on Boron-Based 1D Structures

In this section background information, such as boron-rich materials, crystal structure, the current research status of boron carbide nanowires, synthesis, structural characterization, and thermoelectric properties are reviewed and discussed.

4.1.1 Bulk Boron and Boron Rich Materials

Boron is an intriguing element being the only nonmetal in group III of the periodic table. Also, boron and boron-based materials are unique due to their unusual structural complexity and exceptional bonding [90]. Bulk boron has up to sixteen possible polymorphs, however, only four of them are thermodynamically stable. Those are α -rhombohedral, β -rhombohedral, β -tetragonal and γ -orthorhombic boron [91]. Those polymorphs are often referred to as boron-icosahedral cluster solids (B-ICSs) because of having a common and unique building unit — B_{12} icosahedron. Within the icosahedron, boron atoms occupy twelve vertices and each of them is bonded to its five neighboring boron atoms. Figure 4.1 (a) shows an icosahedron labeled with numbers from 1 to 12. 1 to 6 indicate polar sites and 7 to 12 represent equatorial sites in the icosahedron [92]. These icosahedral units link with each other forming the unit cell of the different polymorphs mentioned above. For example, α -rhombohedral boron

consists of eight icosahedra located at the eight vertices of the rhombohedral unit cell shown in Figure 4.1 (b).

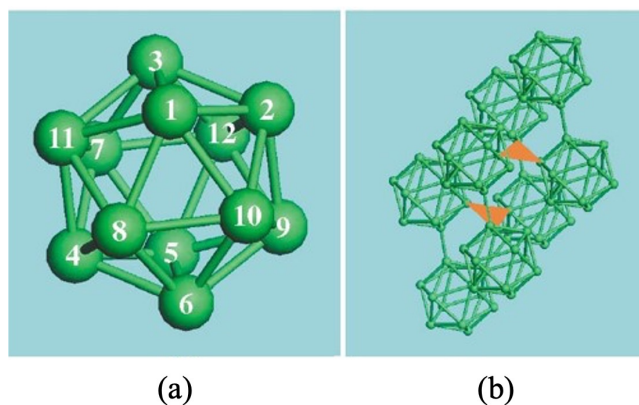


Figure 4.1: (a) B_{12} icosahedron labeled from 1 to 6 for the polar atoms and 7 to 12 for the equatorial atoms, and (b) crystal structure of α -rhombohedral boron showing eight B_{12} icosahedra in the rhombohedral unit cell and red triangles denoting three center bonds [92].

Exceptional bonding of boron arises because of having three valence electrons ($[He]2s^2 2p^1$). $2p^1$ state electron favors metallic behavior, but it is also sufficiently localized because of close proximity to the $2s$ orbital. Due to such electronic states, bulk boron shows highly diverse bonding features such as metallic-like three-center bonds and covalent two-center bonds within and between the icosahedra [91, 93]. In Figure 4.1 (b), three-center bonds are shown as red triangles for three equatorial atoms of neighboring icosahedra [92].

At high temperatures, these icosahedral units link with each other and combine with other impurity elements and form boron-rich compounds such as boron nitride, phosphide, silicide, arsenide, oxide, and carbide. These compounds have a similar structure and bonding features as elemental boron with additional two atoms or three atoms bonds in the inter-icosahedra chains [1].

Due to unusual structures and exceptional bonding, boron-based materials are known for their fascinating chemical and physical properties including low densities ($2.34\text{-}2.52\text{ g/cm}^3$), ultrahigh hardness, large bulk modulus ($185\text{-}227\text{ GPa}$), high melt-

ing points (>2000 °C) and neutron capturing capacity [90]. Boron-based materials are also known to have excellent thermoelectric properties [1].

4.1.2 Bulk Boron Carbide Structure and Properties

Among other boron-rich compounds, boron carbides have been investigated extensively. It is widely selected for the refractory application, ballistic armor, abrasive powders and coatings, and nuclear application. It is also potentially considered for novel high-temperature electronic and thermoelectric applications [94, 95]. Again, unique properties and useful applications of boron carbide materials stem from their atomic structure and bonding. With lattice parameters ($a = 5.16$ Å and $\alpha = 65.7^\circ$), boron carbide has a rhombohedral crystal structure of trigonal symmetry (space group $R\bar{3}m$). Like α -rhombohedral elemental boron as described in the previous subsection, boron carbide has eight icosahedra at the vertices and an additional three-atom chain along the longest body diagonal ([111] axis) of the rhombohedral unit (Figure 4.2(a)). Also, it is a compositionally disordered material with varying carbon percentages ranging from boron rich (8.8 at%) to carbon-rich (20 at%) boron carbide solid solution as can be seen in the phase diagram (Figure 4.2(b)).

Different boron carbide phases (B_xC) have different stoichiometric boron-to-carbon ratios (some B_xC phases are shown in the Figure 4.2(b)). Structural variation between these phases is very small and not easily discernible by XRD [96]. Based on theoretical and experimental studies, the possible structure consists of icosahedra such as B_{12} or $B_{11}C$, and chains for instance C-C-C, C-B-C, C-B-B, B-vacancy-B, and B-B-B. At the carbon-rich side of the homogeneity range, $(B_{11}C_p)C-B-C$ is preferred to $(B_{12})C-C-C$ because of low total energy from the theoretical calculation and high structural symmetry [94, 97] (C_p indicates carbon atom in the polar site of the icosahedron). The exact site occupancy of boron and carbon is still debated even within the same stoichiometry. Because of having similar electronic and nuclear scattering cross-sections, boron and carbon cannot be distinguished easily by most characterization techniques

such as XRD, neutron diffraction, and Raman spectroscopy [97, 95]. However, polarization and lattice distortion data, although not well-defined, indicate a trend of first replacing C-B-C chains by C-B-B chains, and $B_{11}C_p$ by B_{12} icosahedra [97]. In summary, the variation of the boron-to-carbon ratio in the homogeneity range and substitution between boron and carbon within the stoichiometry create compositional disorder as well as result in internal defects such as vacancies, twin boundaries, and stacking faults. This is particularly notable in as-synthesized polycrystalline boron carbides having more disordered structures than the ideal model [1].

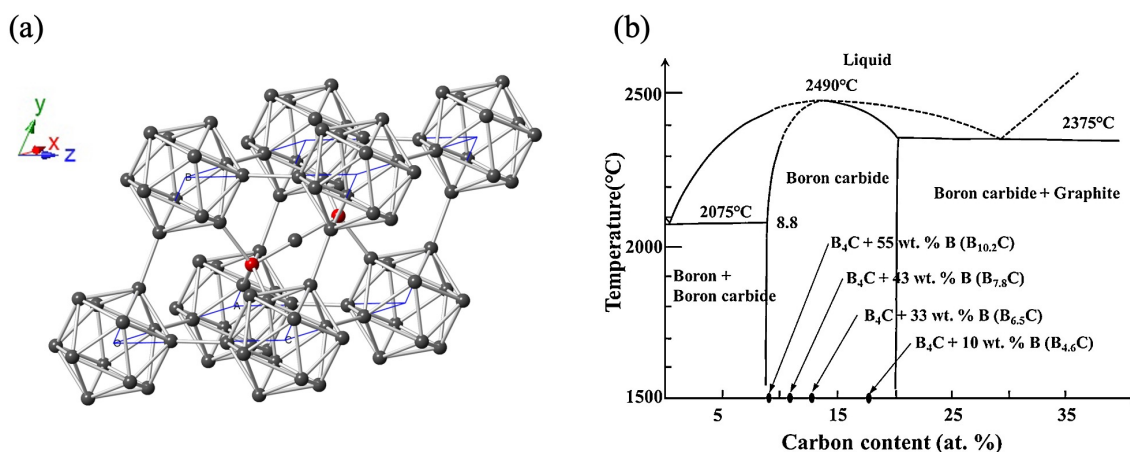


Figure 4.2: (a) Representative rhombohedral crystal structure of boron carbide where boron and carbon atoms are indicated by gray and red colors respectively. The chain here is shown as C-B-C. (b) Boron-carbon phase diagram indicating thermodynamically stable B_xC phases in the 8.8 at%-20.8 at% carbon composition range [97]

Apart from its application as a lightweight and super hard ceramic material, boron carbide has been extensively investigated for its excellent thermoelectric properties. Thermoelectricity is defined as the solid-state conversion between thermal and electrical energy. Thermoelectric (TE) devices can potentially be used to convert a large amount of low-grade waste heat generated in traditional heat engines to electricity, and contribute to reducing greenhouse gas emissions [98, 99]. Despite having potential, TE generators are not as widely used as other power converters (for example combustion engines) due to their low power conversion efficiency. The performance

of TE materials is characterized by two parameters: (i) figure-of-merit Z ,

$$Z = \frac{S^2 \sigma}{\kappa} \quad (4.1)$$

where S , σ , and κ represent the Seebeck coefficient, and electrical and thermal conductivity, respectively.

and (ii) power conversion efficiency η ,

$$\eta = \eta_c \frac{\sqrt{1 + ZT} - 1}{\sqrt{1 + ZT} + T_c/T_h} \quad (4.2)$$

where η_c is the Carnot efficiency, and T_c and T_h indicate temperatures at cold and hot sides of the TE devices. From equation 4.2, efficiency is proportional to the ZT value. Therefore, to maximize the TE performance of a material, a significant Seebeck coefficient S , high electrical conductivity σ , low thermal conductivity κ , and high T are required. However, those parameters are interdependent. Increasing the Seebeck coefficient results in a decrease in electrical conductivity. According to Wiedmann-Franz law, increasing electrical conductivity also increases the electronic contribution to thermal conductivity. This correlation makes it difficult to improve the TE performance significantly.

For semiconductor materials, total thermal conductivity κ arises from electron (κ_e) and phonon transport (κ_{ph}). Most of the research has been conducted to reduce the total thermal conductivity by reducing the κ_{ph} without significantly affecting other parameters.

The most commonly used TE materials include BiTe, PbTe, $\text{Si}_{1-x}\text{Ge}_x$ and their alloys but the current maximum ZT value is close to 1 at 300 k. Boron carbide has been extensively studied for three decades for potential thermoelectric application. This is because boron carbides have a high Seebeck coefficient ($\approx 300 \mu\text{VK}^{-1}$ up to 2000 K [95]), thermally activated electrical conductivity [100], and relatively low

thermal conductivity (as low as 5-12 W/mK) at high temperatures [1], and high-temperature stability. A ZT value of $\gg 1$ has been predicted for boron carbide at high temperatures.

4.1.3 Current Status of Boron Carbide Nanowires

In the past three decades, extensive research has been conducted to improve ZT value by nanostructuring. Nanostructuring can enhance the properties to a great extent due to the quantum confinement effect and increased phonon scattering. Bulk boron carbide is usually used as armors and neutron absorbers. It is also considered a potential candidate for high-temperature thermo-electric (TE) applications as discussed in the previous subsection. In the past decade, our group has successfully synthesized boron carbide nanowires and demonstrated that high TE properties can be obtained. Structure-properties relationship is also explored and found significant improvement for specific kinked nanowires. The growth and properties of boron carbide NWs are discussed briefly in the following.

4.1.3.1 Growth of Boron Carbide Nanowires

Boron carbide was synthesized by different groups using different methods such as plasma-enhanced chemical vapor deposition (PECVD), carbothermal reduction, thermal evaporation, pyrolysis, etc [101, 102, 103, 104, 105, 106, 107, 108, 109]. Based on the use of a catalyst, the growth mechanism is explained as a VLS or VS mechanism. Some boron carbide NWs were grown using oxygen assisted growth mechanism.

Boron carbide nanowires used in this work were synthesized by my previous group-mate, Zhe Guan. Details of the synthesis method can be found in references [62, 1]. Synthesis was performed in a home-built LPCVD system by co-pyrolysis of diborane (B_2H_6) and methane (CH_4) at high temperatures. A Schematic of the LPCVD system is shown in Figure 4.3. The right side of the system is the gas delivery system which has three cylinders for B_2H_6 , CH_4 and Argon (Ar) respectively. The flow rate of each

gas can be controlled independently using gas flow controllers and valves as shown in Figure 4.3.

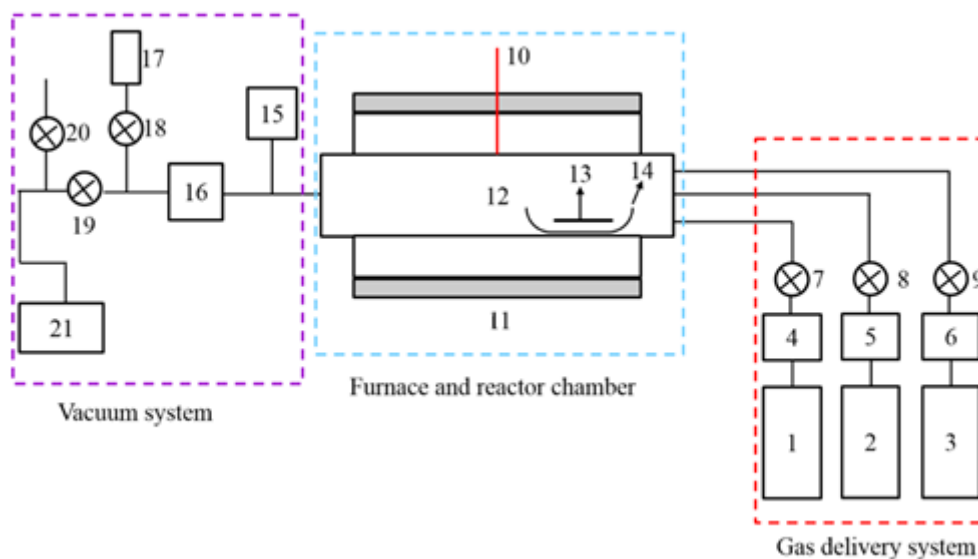


Figure 4.3: Schematic Diagram of the LPCVD system. On the right side, the gas delivery system contains gas cylinders for precursor gases (B_2H_6 and CH_4) and carrier gas (Ar) denoted by 1-3, gas flow controllers by 4-6 and valves by 7-9 for each gas. In the furnace and reactor chamber, 10-14 indicates thermocouple, furnace, quartz or alumina tube, substrate, and quartz or alumina boat respectively. On the left, pressure gauge (15), vacuum trap (16), bubbler (17), valves (18-20), and vacuum pump (21) make the vacuum system [1].

The central reactor chamber has a quartz or alumina tube that is heated by an electrical furnace. A thermocouple sensor (indicated by 10 in Figure 4.3) placed between the tube and heater provides the temperature outside the tube during the synthesis. To have a better understanding of the temperature during the reaction, a temperature profile is created by positioning one thermocouple inside the tube while keeping the other one outside. Inside the tube, temperatures are slightly lower than the set values and vary across the tube having the maximum temperature at the center and lowering near two ends as can be seen in Figure 4.4. The left side in Figure 4.3 has the vacuum system containing a mechanical pump to provide a vacuum, a vacuum trap to capture additional vapors, and a bubbler to release pressure during venting.

Silicon (Si) wafers with 1-micron thermally grown SiO_2 (University wafer, ID 783) were used as the substrates for the growth of the boron carbide nanowires. First, the substrates were cleaned thoroughly by ultrasonic cleaning, blow drying, and oxygen plasma cleaning. After that, the substrates were coated with a nickel film of 2 nm thickness by magnetron sputtering (model Denton Vacuum: Desk IV TSC). Three substrates were placed near the right side of the reactor chamber as shown in Figure 4.4. At three positions, temperature increases from the right side of the furnace towards the center. The concentration of the precursors also varies as shown by the dash-dot and dot curves. Diborane concentration is higher at the right inlet as it gets decomposed while entering the tube. On the other hand, methane concentration increases at higher temperatures away from the right inlet. This variation in temperature and concentration affects the morphology and crystal structures of the synthesized boron carbide nanostructures grown in those three positions.

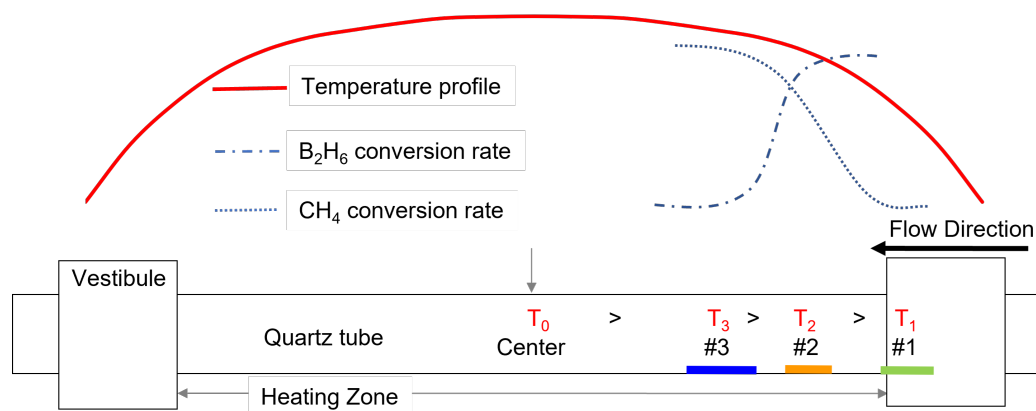


Figure 4.4: Schematic Diagram of the reactor chamber showing temperature profile, position of three substrates at three temperatures T_1 , T_2 and T_3 and concentration profiles of B_2H_6 and CH_4 [1].

The system was evacuated to a pressure of 7 mTorr. Ar gas was introduced at a flow rate of 15 sccm. The temperature was increased to 1050 °C which took 50 minutes. After that B_2H_6 and CH_4 gases were let in both at a flow rate of 15 sccm for

45 minutes. After that gas flow was terminated and the furnace was allowed to cool. The parameters described here are the typical condition for the growth of boron carbide nanowires. Controlled syntheses were also performed by varying different reaction parameters to investigate their effects on the synthesis and hypothesize the growth mechanism of boron carbide nanowires which will be discussed in the section 4.2.

After the synthesis, first, growth substrates were examined using SEM. After that individual nanowires were picked up using the micromanipulator and transferred to a TEM grid. Individual nanowires were characterized in detail for structural information and correlated with measured thermal conductivity.

Structural characterization is summarized briefly in Figure 4.5 [62]. Referring to the temperature profile in Figure 4.4, boron carbide NWs were grown in the T_2 temperature range and only in certain regions of the substrate, which is schematically shown in Figure 4.5(a). So, NWs with desired high aspect ratio were grown between 5-20 mm region from the low T end as shown in the schematic. For all other experiments in this dissertation, cross-sectional samples were prepared from this region from each experimental condition. Figure 4.5(b) presents an SEM image of as-synthesized NWs, with black arrows showing different straight and kinked NWs. From the intensive TEM examination, HRTEM images of the NWs were achieved showing planar defects clearly. Defects were classified as transverse fault (TF) and axial fault (AF) based on their perpendicular and parallel orientation to the growth direction respectively(Figure 4.5 (c) and (d)). Also, a model was developed to determine the fault orientation from those NWs which did not reveal defects from the tilt range available in TEM [61].

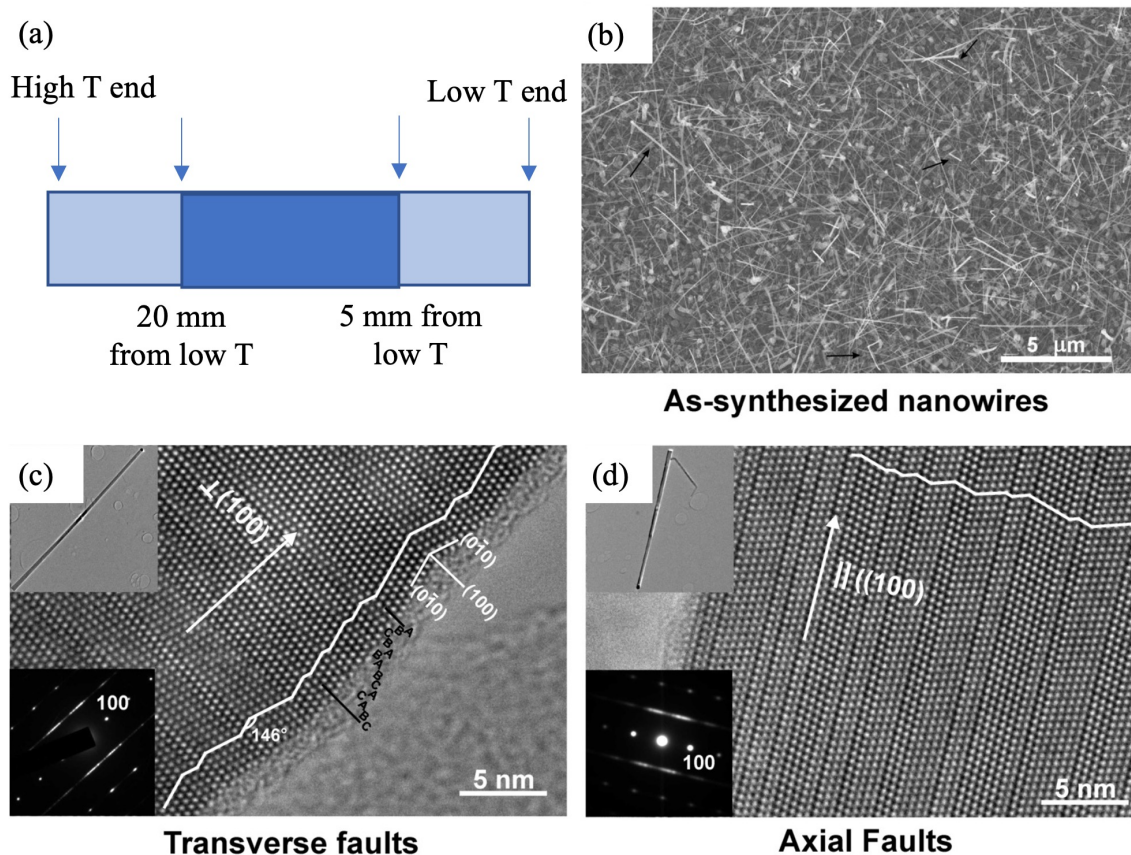


Figure 4.5: (a) Schematic diagram of the substrate showing the regions of interest between 5-20 mm from low T end, (b) SEM image of as-synthesized Nanowires, (c) and (d) HRTEM images of NWs with transverse and axial faults respectively. Insets include DPs and low magnification images of the NWs [62].

4.1.3.2 Properties of Boron Carbide Nanowires

The importance of the defects was clear from the preliminary thermal conductivity data. Significantly lower thermal conductivity was obtained for boron carbide nanowires than the bulk materials. Later on, further experiments were conducted to determine the effect of fault orientation, carbon concentration, and diameter on the thermal conductivity. And it was revealed that thermal conductivity increased with increasing carbon percentage and diameter but did not show significant change due to fault orientation.

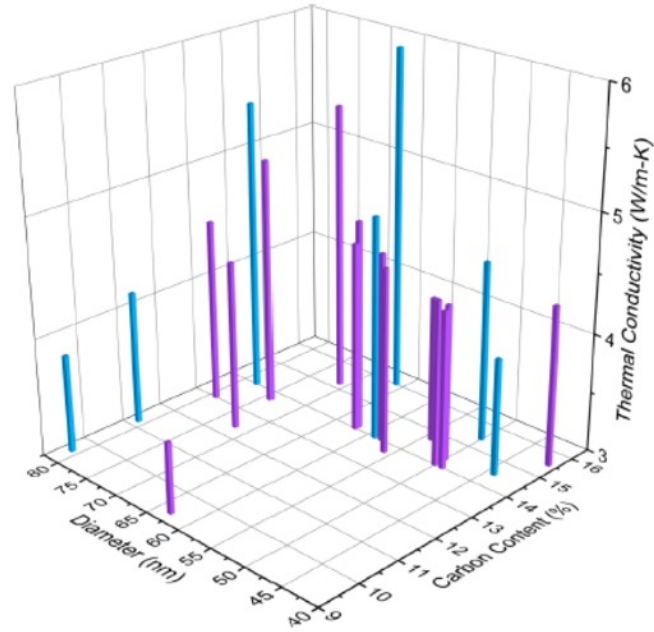


Figure 4.6: Dependence of thermal conductivity on diameter, carbon concentration, and fault orientation. Nanowires with different fault orientations, i.e., AF and TF nanowires are represented by cyan and purple colors respectively [63].

Further work was performed on boron carbide kinked nanowires [63]. Different types of kinked nanowires such as TF-TF, and AF-TF were analyzed using TEM and thermal conductivity were measured. The data showed further reduced thermal conductivity for the kinked nanowires.

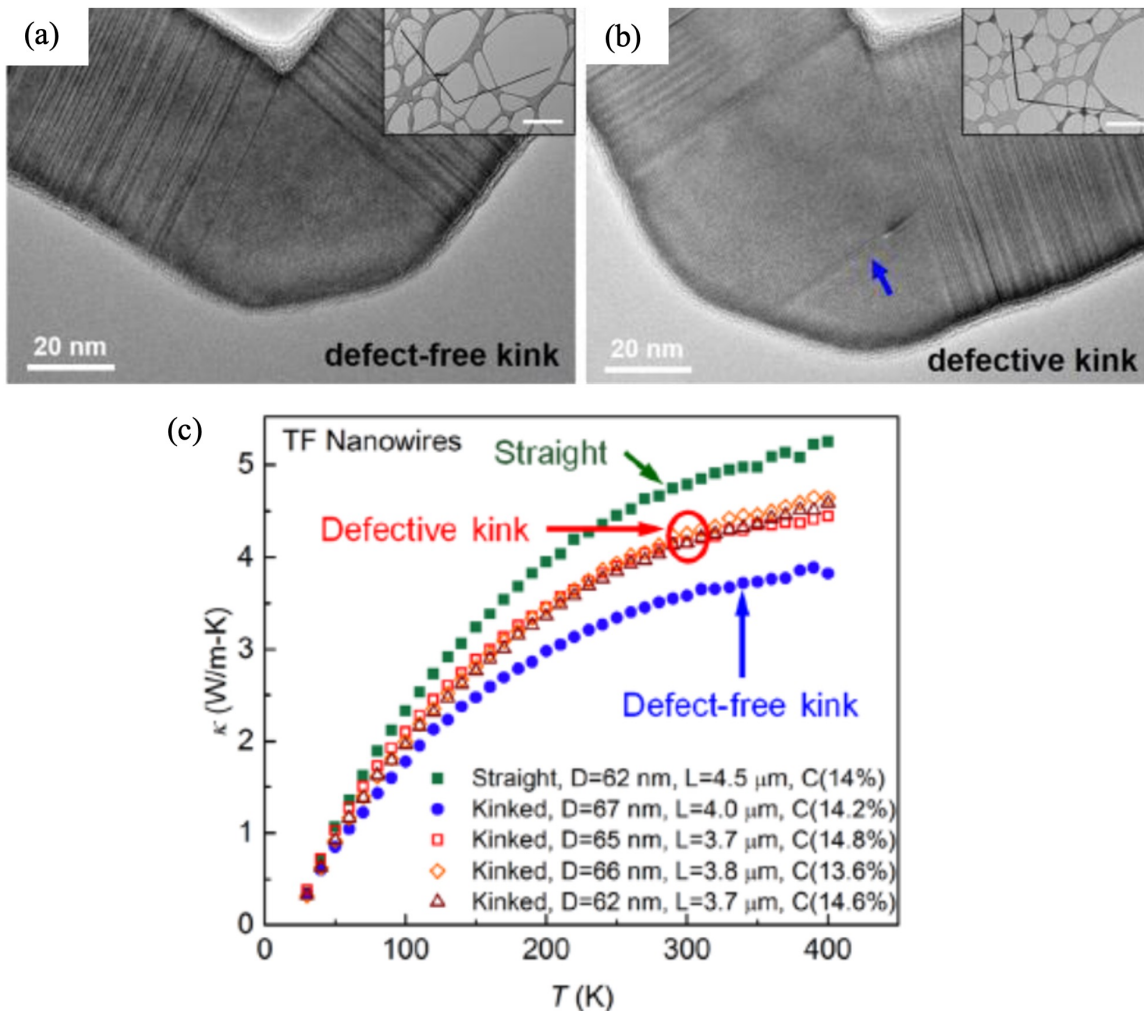


Figure 4.7: Different types of kinked nanowires and thermal conductivity [63].

Structural characterization and thermal properties of boron carbide nanowires were obtained successfully. However, boron carbide NWs with different defect orientations and kinks grew within the same synthesis condition. That leads us to the question, is it possible to rationally synthesize specific boron carbide nanowires with desired thermoelectric properties? To answer the question and obtain more control over the synthesis, a thorough understanding of the growth mechanism is crucial. The routine examination for growth mechanism study was performed by Guan et al. [62], which is briefly summarized here.

4.1.3.3 Routine Examination

Results from routine examination show information about catalyst shape, composition, crystal structure, and migration of the catalyst. In the case of TF nanowires, the catalyst shape is semicircular which indicates their molten state during synthesis. Whereas in AF nanowires, the catalyst interface is faceted, indicating solid status during synthesis. Catalysts on TF nanowires have a new hexagonal Ni-B phase with a melting temperature lower than TF nanowires (1050°C) and composition (Ni wt.% of 72%). Catalysts on AF nanowires have three different phases, all having a melting temperature above 1000°C , more than the common synthesis temperature of AF nanowires. Ni wt.% in the catalyst on AF nanowires is 50-59%.

As mentioned before, the routine examination cannot provide all the information, specifically about the interaction between the substrate, catalyst, and precursors. As a continuation, further experiments were conducted to prepare samples with varying reaction conditions, and cross-sectional TEM examinations were performed on the prepared samples. Approaches for those experiments and obtained results are discussed in the following section.

4.2 Experimental Results from Cross-Sectional Examination

To have a better understanding of the growth mechanism, cross-sectional TEM examinations were performed on a few samples. As mentioned earlier in section 2.3, cross-sectional TEM examination requires a tedious sample preparation technique. Table 4.1 shows the list of experimental conditions to run in the CVD. Samples obtained from those conditions were prepared using the cross-sectional preparation technique. The main goal of performing cross-sectional analysis is focused on understanding the interaction between catalysts, substrates, and other precursors for the VLS growth of boron carbide NWs. As it is not possible to see the growth dynamically without the in-situ technique, the strategy is to perform post-analysis of

the samples and for this purpose, the original Si/ SiO₂ substrate was treated in the reaction chamber by varying the reactant parameters. For example, in the case of the first sample, Si/ SiO₂ substrate was treated only in the Ar gas without any Ni coating, and reaction gases (B₂H₆ and CH₄). Similarly, other samples were prepared by varying reactant parameters to see the effect of each parameter to form the catalytic particles during the initial growth stage.

Table 4.1: List of experimental conditions of varying reactants keeping substrate (Si/ SiO₂), temperature (1050 °C) and reaction time (45 minutes) same.

Condition	Ni (nm)	B ₂ H ₆ (sccm)	CH ₄ (sccm)	Ar (sccm)
1	0	0	0	15
2	2	0	0	15
3	2	15	0	15
4	2	0	15	15
5	0	15	15	15
6	2	15	15	15

4.2.1 Reference Cross-sectional Sample

Before starting cross-sectional preparation of the samples listed in Table 4.1, the original Si/ SiO₂ substrate was used as a dummy sample to (i) learn and practice the technique and (ii) use the results as a reference for the other samples. The aforementioned challenge of the cross-sectional sample preparation technique can be indicated here by mentioning that the first successful sample was obtained after sixteen trials of dummy samples. After preparation, the samples were examined under TEM. The images of the dummy sample are presented below.

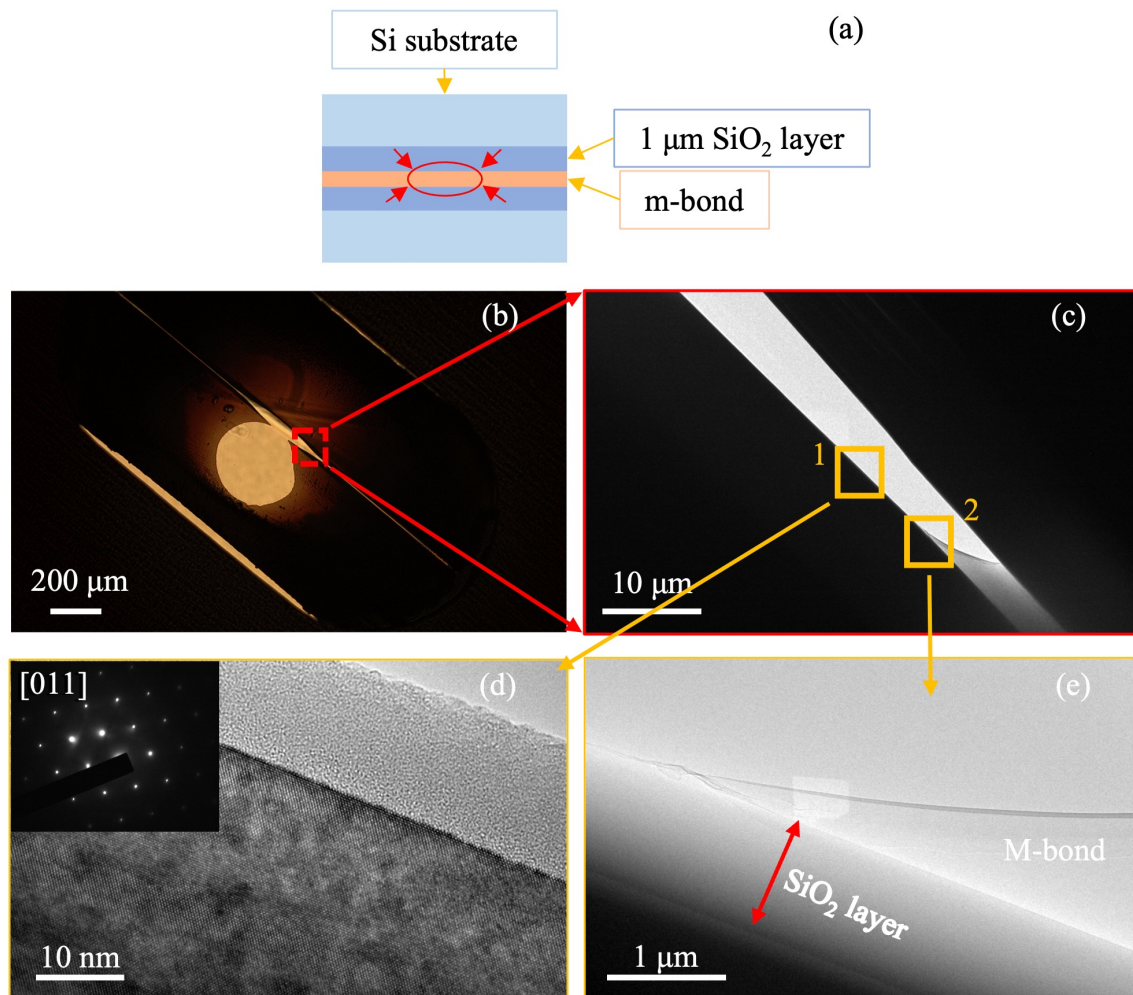


Figure 4.8: (a) Schematic drawing of the cross-sectional view from the dummy sample, showing Si, 1 μm SiO₂ layer and m-bond (thicknesses are not to scale), (b) optical micrograph of the dummy sample at a low magnification, (c) cross-sectional TEM images from the red square marked in (b) at a low magnification, (d) HRTEM image and DP (in the inset) from the position 1 in (c), and (e) low magnification TEM image from the position 2 in (c). The scale bar is indicated in each image.

In Figure 4.8 (a), a schematic drawing of the cross-sectional view from the dummy sample is presented where Si substrate, 1 μm SiO₂ layer, and m-bond are clearly indicated. Before TEM examination, a low magnification image was taken from an optical microscope which shows the interface between two pieces joined by m-bond. A large round hole can be seen near the interface. Ideally, a small perforation in the interface is expected. In this case, during the milling process, perforation was

initiated afar from the interface. As it was required to have the interface region electron transparent, the milling time was increased which resulted in a large hole. A red rectangle is drawn in Figure 4.8 (b), to indicate a location that is examined using TEM. A low magnification TEM image from that location is shown in (c) with two more positions designated by 1 and 2, and magnified images from those positions are included in Figure 4.8 (d) and (e).

HRTEM image and corresponding DP (in the inset) from position 1 can be seen Figure 4.8 (d). HRTEM image reveals single crystalline silicon with a thin SiO₂ amorphous layer. DP corresponds to the zone axis of [011] for Si. Due to ion milling, and perforation created in the interface, m-bond and most of the SiO₂ layer is damaged in this position. Position 2 in Figure 4.8 (c) is magnified in (e) (but with much lower magnification than (d) as indicated by the scale bar). From this image, m-bond, 1 μm SiO₂ layer along with the Si substrate can be seen clearly. However, due to the high thickness in this position, HRTEM images cannot be obtained.

Figure 4.9 shows another dummy sample location and obtained EDX result. From Figure 4.9 (a), A red rectangle indicates a location in the ion milled area where the EDX data were acquired, and obtained EDX result from this location is presented in (b). From the EDX spectrum, it can be found that the strongest peak is from Silicon (Si). O peak is present as expected, however, some other peaks (Copper (Cu), Molybdenum (Mo), Aluminum (Al), Magnesium (Mg), and Chromium (Cr)) can also be found. Those are most likely artifacts during the examination. For example, the prepared cross-sectional sample is attached to the Mo ring, which can contribute to the spectrum. Cu can be detected from the pole piece of the electromagnetic lens and the sample holder. Cu and Cr X-rays can also be generated in the specimen chamber, column, and apertures by Rutherford backscattered electrons [110]. Al and Mg could have been detected due to contamination either during sample preparation or in the TEM specimen chamber. If those artifacts are removed from the EDX results, wt.%

of Si and O can be obtained as shown in the inset of Figure 4.9 (b). The obtained elemental composition can be compared with the theoretical wt.% of Si and O in SiO_2 . It can be seen that obtained Si wt.% is much higher than the composition of SiO_2 . That indicates the location contains Si and the amorphous SiO_2 layer.

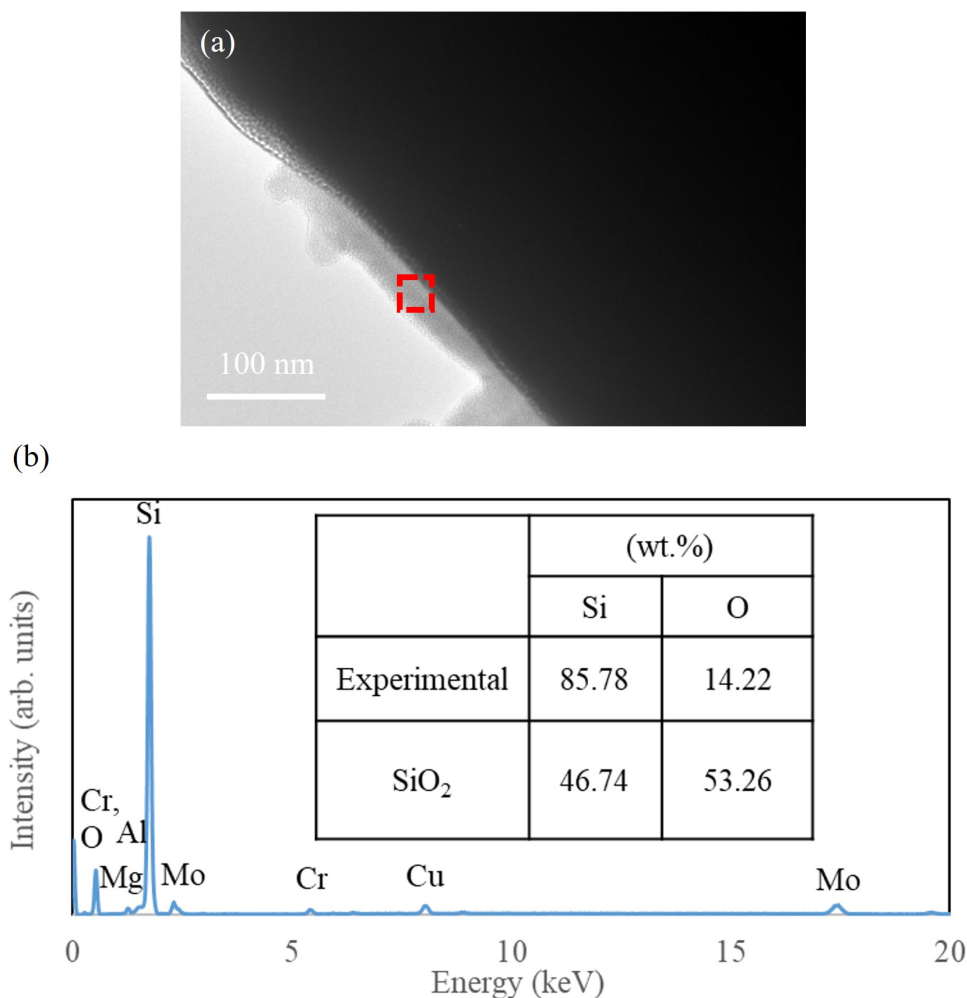


Figure 4.9: (a) TEM image showing a location near the perforation of another dummy sample where EDX data were acquired, (b) EDX result showing the compositional information within the indicated location. The inset shows experimental wt.% of Si and O from the obtained data and theoretical wt.% of those elements in the SiO_2 .

Thus, TEM images and EDX results of the dummy samples can be used as the reference for other cross-sectional samples. It helps to find easily the Si substrate from the same zone axis [011] and single crystalline HRTEM image, and 1 μm SiO_2 layer and m-bond from relatively low magnification images. After identifying the above,

further examination is done to obtain images of other features based on different types of samples.

4.2.2 Effect of Annealing

Referring back to Table 4.1, condition 1 was prepared by annealing the Si/ SiO₂ substrate in the Ar gas environment. The purpose is to see the effect of annealing on the substrate, consequently in the growth process. Representative images from condition 1 are presented below.

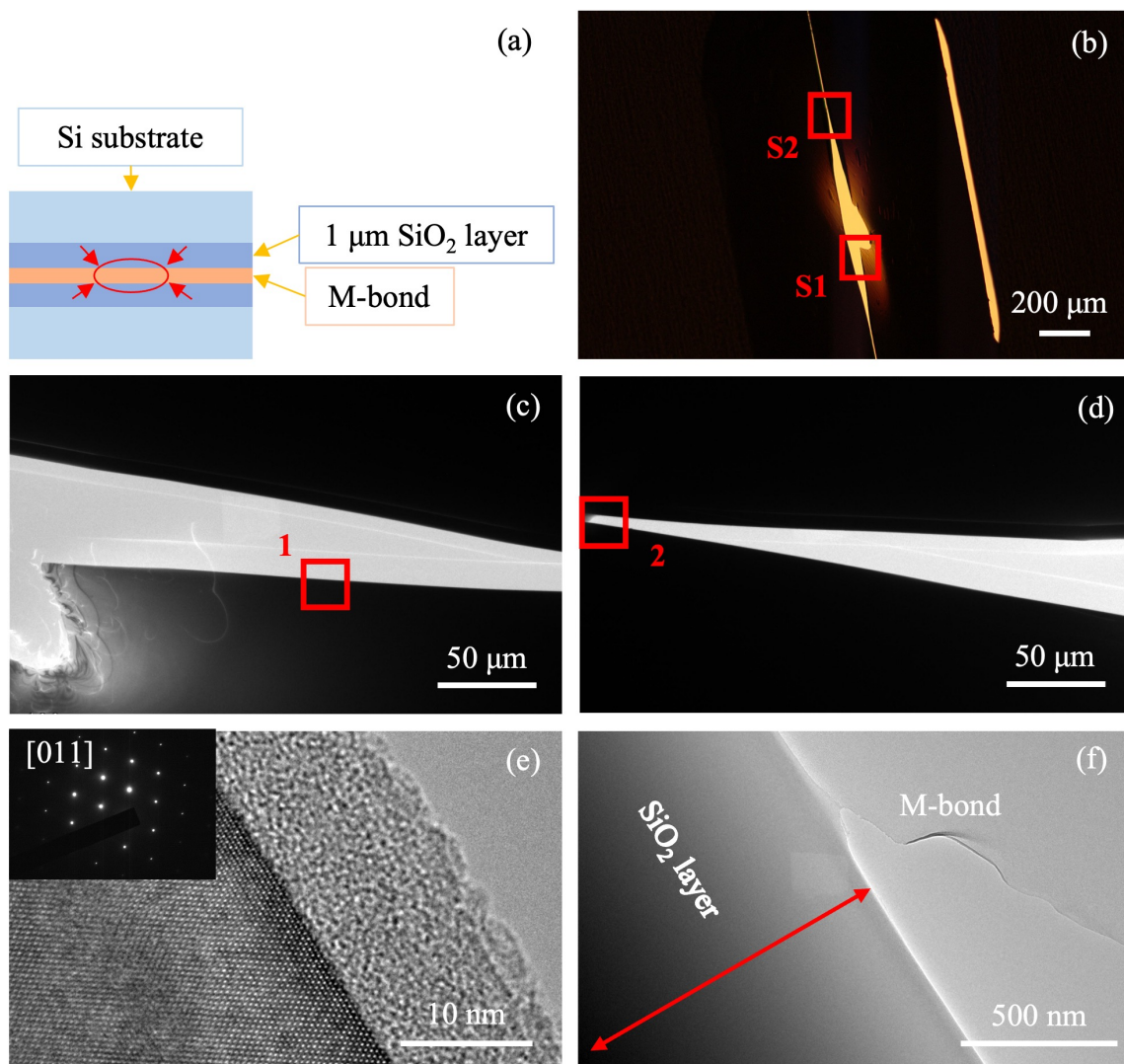


Figure 4.10: (a) Schematic drawing of the cross-sectional sample from condition 1, showing Si, 1 μm SiO₂ layer and m-bond (thicknesses are not to scale), (b) optical micrograph of the cross-sectional sample at low magnification, showing two sites S1 and S2 in the red squares, (c) and (d) cross-sectional TEM images from S1 and S2 in (b) at low magnification, (e) HRTEM image and DP (in the inset) from the red square shown in (c), and (f) TEM image from the red square in (d). The scale bar is indicated in each image.

Figure 4.10 (a) shows a schematic drawing of the cross-sectional sample and indicates the possible sites for observation by red arrows. (b) shows an optical micrograph of the cross-sectional sample using the transmitted light after ion milling. As mentioned above in subsection 4.2.1, a small perforation is desired after ion milling. However, obtaining that is challenging because of the two small pieces of the samples

being joined using the m-bond adhesive. Despite having good stability of the m-bond, it starts to disintegrate after some time in the PIPS, and instead of obtaining a small perforation, a relatively bigger region can be achieved as shown in Figure 4.10 (b) and that is the case for most of the cross-sectional samples. Two sites S1 and S2 are indicated in this figure which is examined using TEM.

Figure 4.10 (c) and (e) shows a low magnification TEM image and HRTEM image and DP respectively from S1 in (a). Similar to the dummy sample, HRTEM and DP corresponds to the Si as both m-bond and SiO₂ layer are damaged in this location. Low magnification TEM image and relatively higher magnification of a location from S2 in (a) are presented in Figure 4.10 (d) and (f). A broken m-bond layer and 1 μm SiO₂ layer can be seen in Figure 4.10 (f). Overall, compared to the dummy sample, a significant change could not be observed from the TEM images due to annealing in the Ar gas.

4.2.3 Catalyst Formation and Effect of Temperature

In condition 2, Si/ SiO₂ substrate was coated with 2 nm Ni film via vacuum sputtering and annealed in the Ar gas. Two different regions are indicated from the low temperature (T) end as shown in the schematic drawing in Figure 4.11 (a). Samples from 5-8 mm and 15-18 mm away from the low T end were prepared for the cross-sectional examination. Figure 4.11 (b) and (c) show low magnification TEM images of those samples. The temperature range measured by thermocouple for the substrate in the T₂ region (Figure 4.4) is 908-931 °C. So, the temperature difference between two regions of our interest can be estimated to be $\approx 20^\circ\text{C}$.

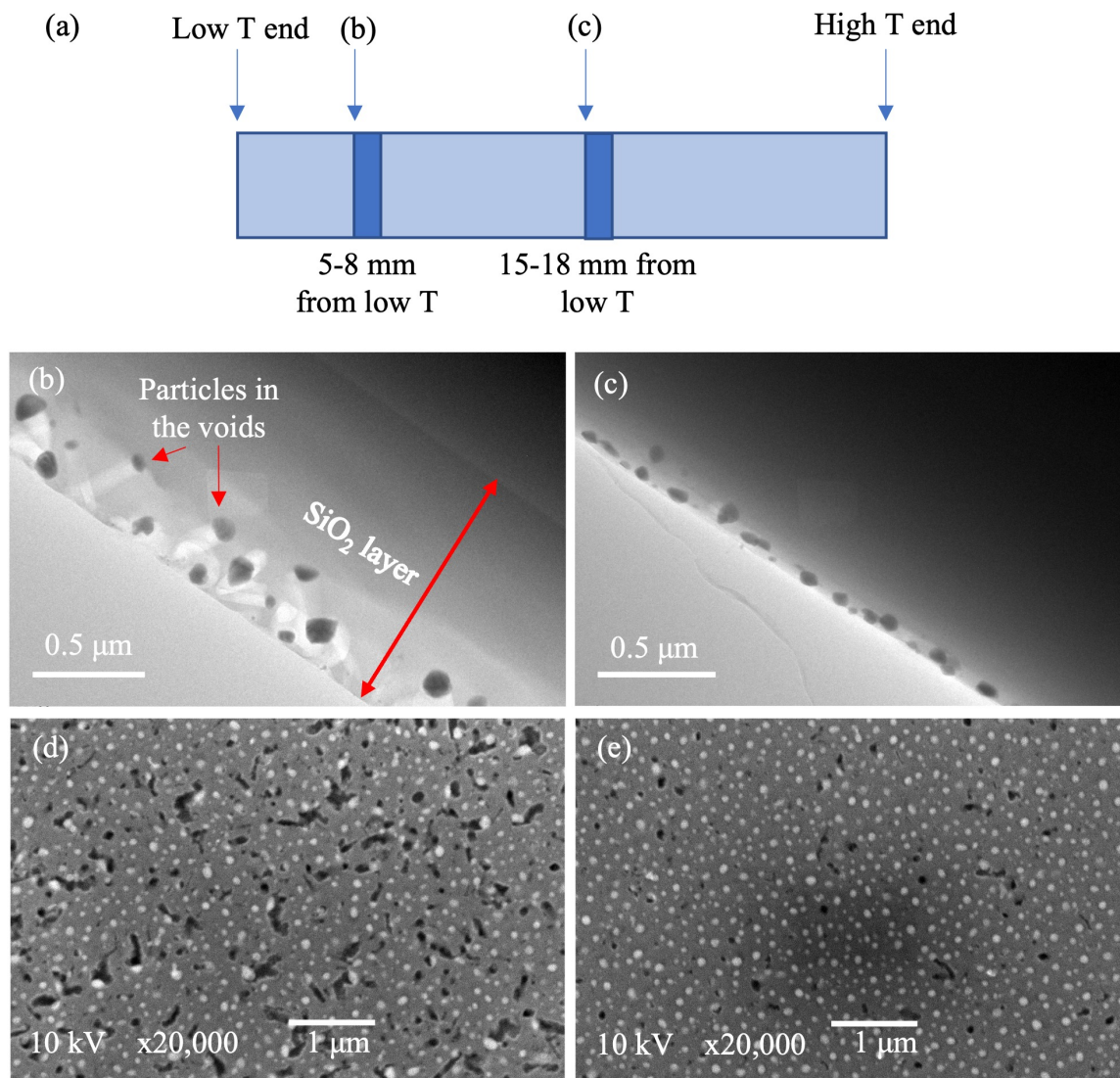


Figure 4.11: (a) Schematic drawing of the growth substrate showing two regions that were used for the cross-sectional sample preparation and examination (not to scale), (b) and (c) cross-sectional TEM images from two regions shown in (a), and (d) and (e) top view SEM images from 10 mm and 15 mm away from low T end. The scale bar is indicated in each image.

Both (b) and (c) show that continuous Ni film agglomerates and forms particles of different sizes and shapes in the growth environment. Between the two regions, the only variable is localized temperature. From Figure 4.11, (b) shows some larger particles than (c). So, seemingly different particle sizes and size distribution can be observed due to small temperature differences as mentioned before. Also, in both

cases, particles diffused in the SiO_2 layer, with a higher diffusion depth for the relatively low temperature than that of the other (based on the Figure 4.11 (b) and (c)), which is counter-intuitive and is discussed later.

Before preparing the cross-sectional samples, growth substrates were examined and top-view images were recorded using SEM. Figure 4.11 (d) and (e) show SEM images from 10 mm and 15 mm away from the low T end, which can be compared with the cross-sectional images in (b) and (c) to have a better understanding of the agglomeration and diffusion of the particles. In both SEM images, bright particles can be seen on top of the darker surface along with groove/hole-like features. If (b) and (c) are compared with (d) and (e), bright particles in SEM images correspond with the darker particles in the TEM images. The contrast in both TEM and SEM images is due to the higher atomic number of Ni compared to Si. One prominent difference that can be seen between Figure 4.11 (d) and (e) is the higher void density at the relatively lower temperature region. The TEM image in (b) is consistent with this observation where some particles can be seen in the voids (one particle is shown by a red arrow). In contrast, voids are less observed in (c), which is in agreement with the SEM image in (e). However, the higher diffusion depth of the particles and higher void density in the relatively low-temperature region both are contradictory to the literature. Before we jump into the possible reasoning behind this, particle size and distribution are analyzed in the histograms and presented below.

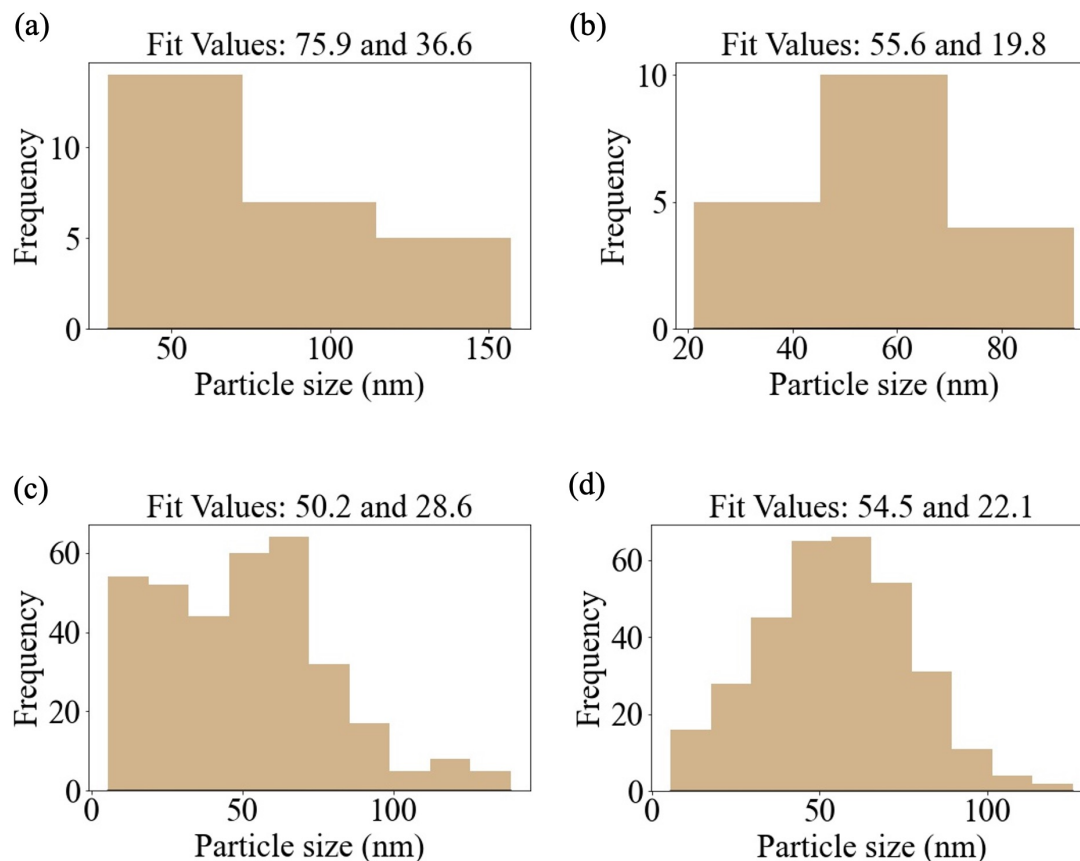


Figure 4.12: Histograms plotted from the TEM and SEM images from Figure 4.11 and presented in the same sequence. So, histograms in (a), (b), (c), and (d) correspond to figure 4.11 (b), (c), (d), and (e) respectively.

Histograms from TEM and SEM images in Figure 4.11 (b-e) were plotted and presented sequentially in Figure 4.12 (a-d). Histograms from TEM images are not representative here as the sample size is small for the analysis. That is because many particles are overlapping and their sizes cannot be calculated accurately. However, histograms from the TEM images are still presented for the purpose of comparison. From Figure 4.12 (a), in the 5-8 mm region, the average particle size is relatively large (75.9 ± 36.6 nm), but the histogram shows more particles are of smaller sizes. Histogram from SEM image (Figure 4.12 (c)) also shows a similar pattern, i.e., the number of smaller size particles is higher than that of larger particles, although average particle size is lower than that of (a). Again, two issues with the analyzed data,

less sample size for the TEM image and lower resolution of the SEM image compared to the TEM image. On the other hand, a relatively more uniform size distribution can be observed in the 15-18 mm region (Figure 4.12 (b) and (d)). Higher annealing temperature results in the coalescence of the particles as seen for other metallic thin films [111]. More uniform size distribution observed in the 15-18 mm region may be the result of the coalescence of particles at the slightly higher annealing temperature.

The above results formed in condition 2 of the experiments are due to the thermally activated process of Ni thin film dewetting the substrate and forming particles, also known as agglomeration. Different factors such as film-substrate interfacial energy, and stresses within the film can drive/activate the agglomeration process. Kwon et al. discussed two mechanisms for agglomeration of Cu and Au thin films: grain boundary grooving, and void nucleation and its subsequent growth respectively [112]. The first mechanism is explained by the tendency of forming a depression at the triple point of the grain boundary with either film surface or film-substrate interface. The depression formation tendency is justified by the force balance at the triple point. With annealing, the triple points become the preferred sites for the nucleation of voids. Those voids grow with further annealing, resulting in a partially continuous film, and finally, form isolated islands/ particles of the film material. In the other mechanism, void nucleates in the areas with excessive defects/ high stress and grows laterally into an irregular shape with void branches. This branched structure is called a fractal. With annealing, these fractals coalesce and cover the whole area and eventually form isolated islands/ particles similar to the first mechanism [112, 111]. Peterson et al. discussed the agglomeration behavior of Ni film on SiO₂ as the grain boundary grooving mechanism [113]. However, Thron et al. presented an argument that void nucleation is the more dominant mechanism for Ni film as instability in the grain boundary and film-substrate interface is greater than that of grain boundary and film-surface interface [114].

Now, why the diffusion depth and void density are higher in the relatively low-temperature zone? Is there any reaction between Ni and SiO₂ layer which dominates the agglomeration in the low-temperature region? Dewetting behaviors of metal films such as Cu, Au, Ru, Pt, and Ni on amorphous SiO₂ layer are explored previously and presented mostly by top-view SEM and TEM images [112, 111, 113]. For example, SEM images of annealing of 5 nm Ni film on ≈ 500 nm SiO₂ for 1 hour at different temperatures are presented by Petersen et al. (Figure 4.13) [113]. Before annealing, Ni film is polycrystalline and continuous on the substrate. At higher temperatures, little holes/voids form and grow which results in exposing the substrate and piling up the film material. However, starting at 300°C, the number of holes decreases due to the coalescence of adjacent holes, and thus, Ni film becomes discontinuous and forms islands. From this example, it can be concluded that void formation in the Ni film can start at below 100 °C, and with higher annealing temperature, voids coalesce/reduces to form particles [113]. But void formation in the SiO₂ layer (similar to our case) cannot be confirmed from top-view images and also, the annealing temperature, in this case, is much lower than our experimental condition.

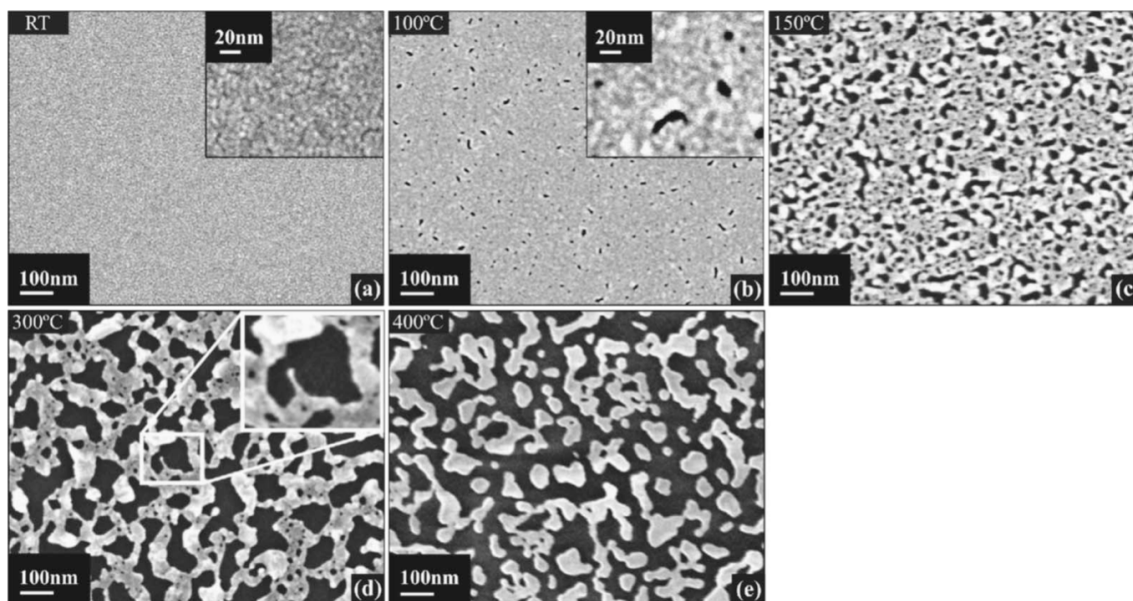


Figure 4.13: Annealing of 5 nm Ni film on ≈ 500 nm SiO_2 layer for 1 hour at different temperatures: (a) before annealing at room temperature, (b) 100°C , (c) 150°C , (d) 300°C , and (e) 400°C [113].

Banno et al. predicted a reaction between SiO_2 layer and Ni film during agglomeration based on the cross-sectional TEM image, where the particles penetrated onto SiO_2 surfaces, and also EDS data showed Si content in the particles [115]. The reaction between Ni and SiO_2 and generation of Ni_3Si was observed for prolonged heating at 577°C in a hydrogen atmosphere [116]. On the contrary, Thron et al. showed two different mechanisms during in-situ annealing, (i) Ni diffusion through native SiO_2 thin layers and formation of supply-limited NiSi_2 layer in the SiO_2/Si interface, and (ii) dispersion and agglomeration of Ni islands in the SiO_2 layer, but no reaction layer between Ni and SiO_2 was observed [117]. Ni diffusion through native or ultra-thin SiO_2 layer (a few nm) without reaction has been demonstrated by other researchers [118, 119], but thicker SiO_2 acts as a diffusion barrier for Ni [118, 120].

Void formation in SiO_2 layer by Ni and other similar noble and quasi-noble metals was discussed as a dominant mechanism for oxide decomposition by Dallaporta et al [119]. Their hypothesis claims that thermodynamically favorable reaction products do not exist for these metals with SiO_2 , and bulk diffusivities of these metals are

also relatively low to explain their transport through the SiO_2 . However, thermal oxide films like SiO_2 always have pre-existing microchannels/defects which can be the source of void nucleation. Also, the stress in the metal film/ SiO_2 interface can enhance the void nucleation during high-temperature annealing due to their different thermal expansion coefficients. Furthermore, metal particles can diffuse through the microchannels easily and reach the Si/ SiO_2 (for ultrathin SiO_2 layer) and react with Si to form silicides. The energy released from this reaction can assist to the decomposition reaction ($\text{Si} + \text{SiO}_2 \rightarrow \text{SiO} \uparrow$), which is known to happen at high annealing temperature ($\approx 750^\circ\text{C}$ for 1 nm thick oxide [121], but the higher temperature is required for thicker oxide layer for this reaction [120]). This is a hypothesis, but the decomposition reaction enhances because of the interaction of metals. The decomposition reaction and desorption of SiO can eventually speed up the void growth [119]. However, this mechanism of void nucleation, metal diffusion, and decomposition reaction depends on oxide thickness, annealing time, and temperature. For thick SiO_2 layer (>50 nm), the rate of Ni diffusion through microchannels is slow and requires a higher temperature for the diffusion and subsequent reaction [118]. Our experimental data shows voids near the surface of the SiO_2 . The thickness of the SiO_2 layer in our experimental condition is $1 \mu\text{m}$ and the temperature range is $\approx 908\text{-}931^\circ\text{C}$. So, it can be hypothesized that despite the thicker oxide layer, the annealing temperature is high enough to initiate the void nucleation mechanism, at least near the surface of the SiO_2 layer.

We can roughly summarize the void nucleation mechanism by the schematic diagram shown in Figure 4.14. Figure 4.14 (a) shows Ni/ SiO_2 /Si substrate stack including microchannels in the SiO_2 before annealing. A number of events may occur during annealing as shown in Figure 4.14 (b). (i) void nucleation in the SiO_2 due to microchannels and stress between Ni/ SiO_2 interface, (ii) agglomeration of Ni film by grain boundary grooving/ void nucleation and growth mechanism, (iii) Ni particles

diffusion through the void, (iv) decomposition reaction of SiO_2 and excess Si due to higher annealing temperature and absence of oxygen environment and desorption of SiO. Some Si may transport through the microchannels into the SiO_2 layer and excess Si near the voids has been reported previously. As mentioned before, void formation and Ni diffusion through the SiO_2 occur without any reaction between them [118]. At the current stage, the composition of the particles observed in the TEM image is not known. If the particles contain Ni_xSi_y , even in the surface layer of the Ni particles, it would indicate that some Si diffusion occurs through the microchannels/defects in the SiO_2 layer.

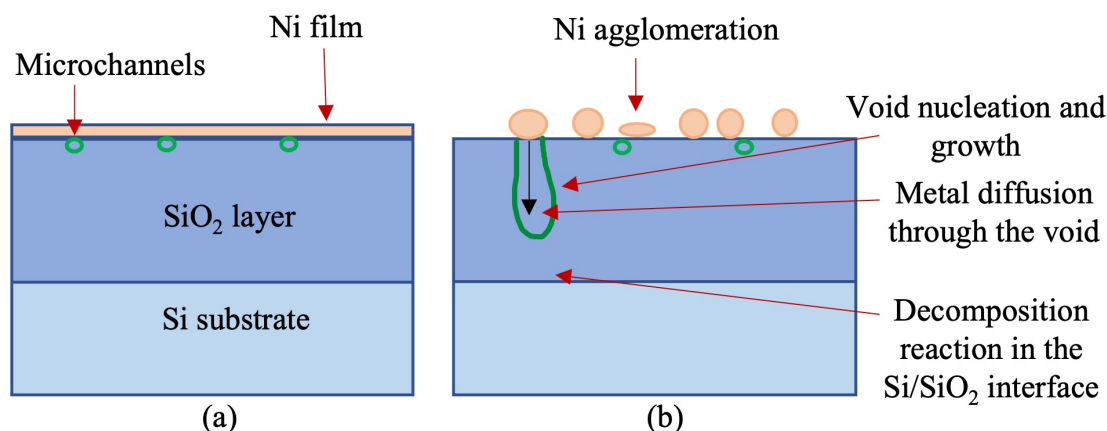


Figure 4.14: Schematic diagram (not to scale) of void formation in the SiO_2 layer, (a) before annealing and (b) during annealing.

However, it is still not clear why higher void density and diffusion depth were observed in the relatively low-temperature zone. If we look at the temperature profile in the CVD chamber again, temperature increases from the right side towards the center of the quartz tube. When the temperature outside the tube is 1050 °C, measured temperatures at T_1 , T_2 , and T_3 are approximately 630-750 °C, 908-931 °C, and 964-977 °C.

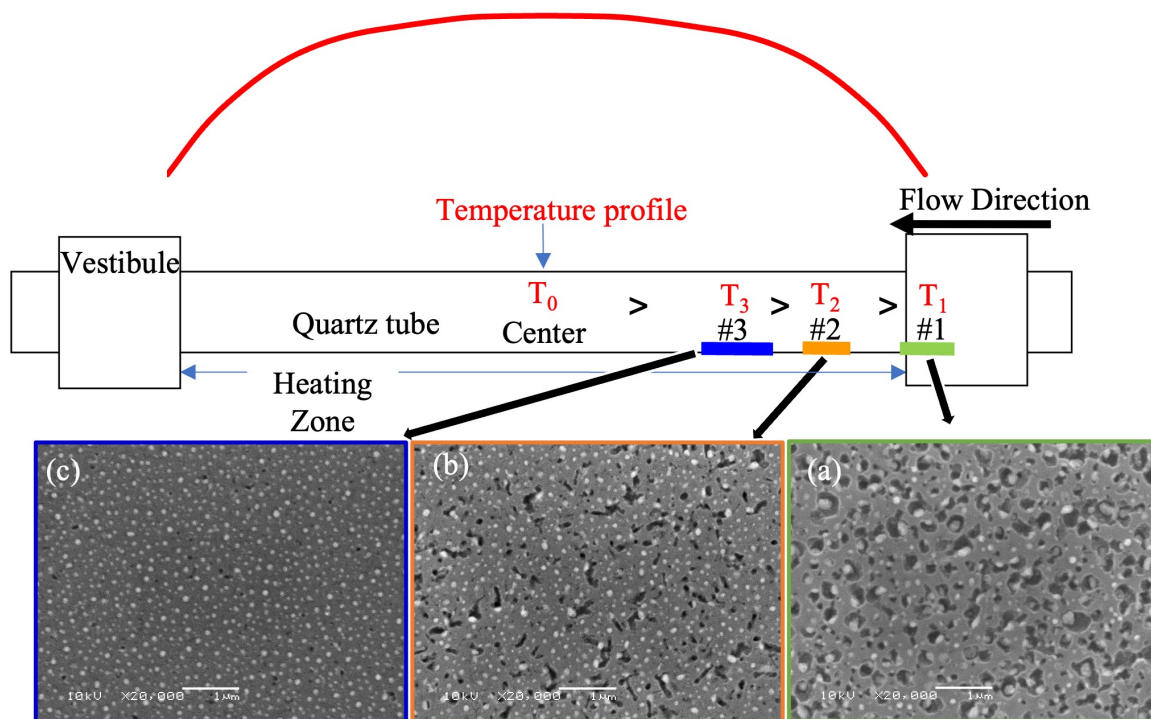


Figure 4.15: Temperature profile along with SEM images from the different regions of the reaction chamber, (a) T_1 ($\approx 630 - 750$ °C), (b) T_2 ($\approx 908 - 931$ °C), (c) T_3 ($\approx 964 - 977$ °C)

Figure 4.15 presents SEM images from three temperature zones. It was observed that with increasing temperature, dewetting behavior is significantly different between the three images. As the temperature is increasing, void density and sizes are decreasing and particle sizes are changing from non-uniform to more uniform distribution. This change or temperature effect is similar to the small temperature variation (≈ 20 °C) observed for two regions in the T_2 region in Figure 4.11 (d) and (e). However, the reason behind this behavior is not known at the current stage and further investigation is required. Based on the finding, a small variation in the localized temperature can influence Ni dewetting and voids in the SiO_2 layer, which can eventually be more significant along with the effect of other reactant parameters.

During cross-sectional TEM examination, some EDX spectra were collected from the 15-18 mm region to determine the elemental information. Another low magnifica-

tion TEM image showing different locations for data collection is presented in Figure 4.16 and wt.% of elements from those locations are presented in Table 4.2.

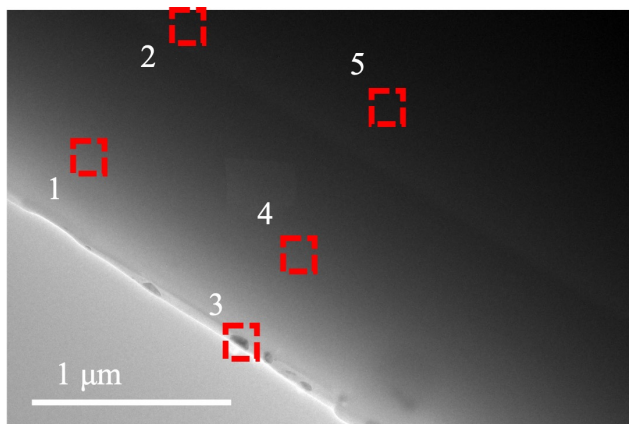


Figure 4.16: Cross-sectional TEM image of a sample from 15-18 mm away from Low T end showing locations of acquired EDX spectra.

Table 4.2: Wt.% percentage of Si, O, and Ni (after extracting artifacts from the EDX spectra) from different locations shown in Figure 4.16.

Location	Si (wt.%)	O (wt.%)	Ni (wt.%)
1	62.81	37.19	0.00
2	100.00	0.00	0.00
3	60.70	36.10	3.20
4	71.72	27.02	1.26
5	99.86	0.14	0.00

EDX spectra were collected near the interface of the cross-sectional sample. Point 1 indicates SiO₂ layer. EDX result from the particle (in location 3 Figure 4.16), shows the presence of Ni along with Si and O. Ni can also be detected from location 4. Location 2 and 5 show almost 100% Si, and indicates that those two locations are in the Si substrate and beyond the Si/SiO₂ interface. However, further EDX spectra collection and DP analysis on the particles are required to confirm the composition. That can help with the hypothesis regarding the reaction of Ni film and SiO₂.

4.2.4 Effect of Diborane

In condition 3, diborane gas was added to the growth environment but methane gas was absent, therefore, nanowire growth was not seen. Samples were prepared from two regions, 5-8 mm and 15-18 mm away from the low T end which is presented in Figure 4.17. Two sets of cross-sectional TEM images from two regions are presented in (b), (d), and (c), (e) respectively, and corresponding top-view SEM images can be seen in (d) and (e). Due to the pyrolysis of diborane, highly reactive boron (B) containing species (such as $\cdot\text{BH}_3$, B_4H_{10} , B_5H_{11} , $\text{B}_{10}\text{H}_{14}$, etc.) [122] and hydrogen (H) are generated that reacts with the SiO_2 layer and forms porous structure as shown in Figure 4.17 (b-e). Catalytic particles can also be seen here. However, compared to condition 2, particle sizes are small and diffusion depth into the SiO_2 layer is higher. The diffusion of the particles may have been facilitated due to the porous structure.

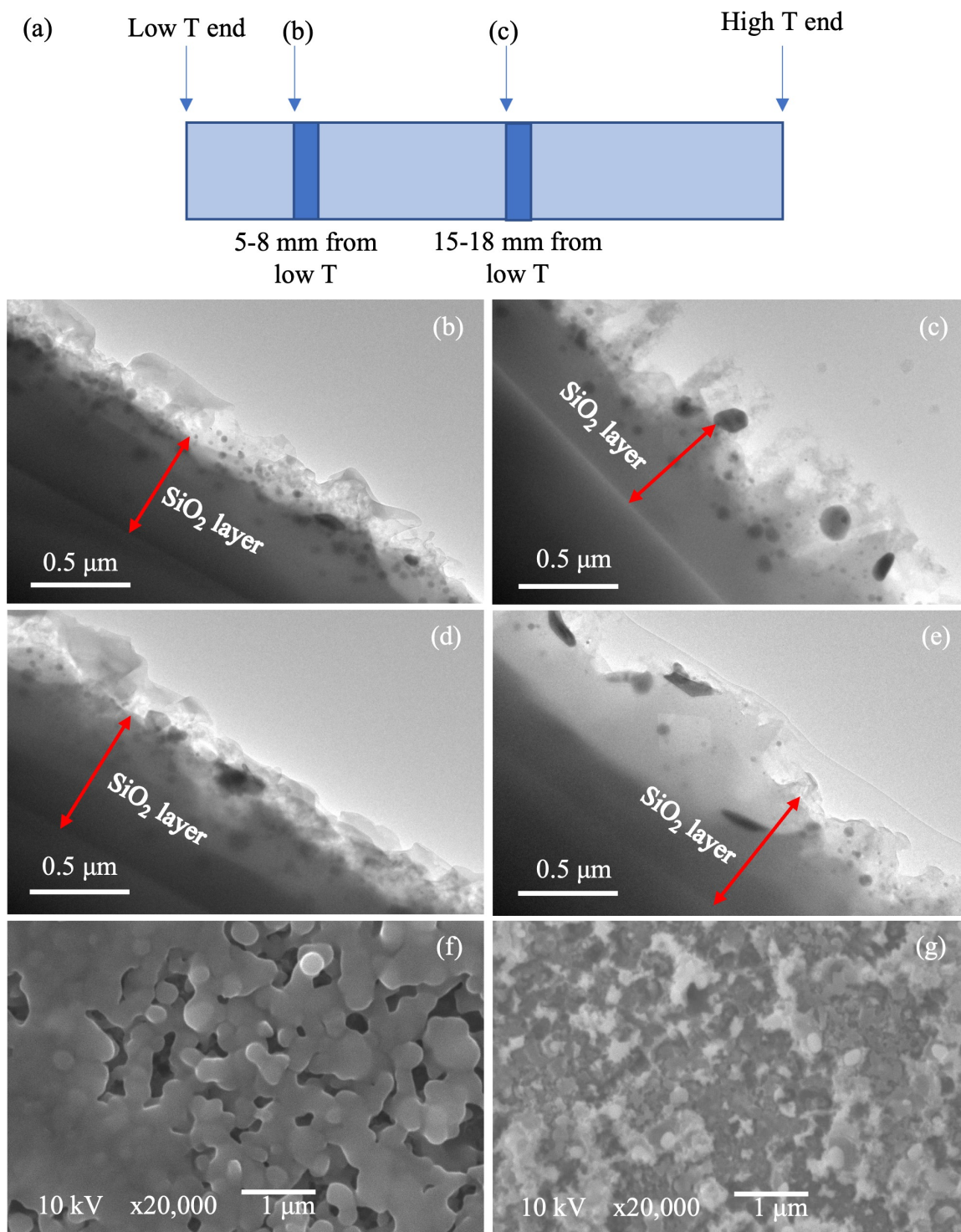


Figure 4.17: (a) Schematic drawing of the growth substrate showing two positions that were used for the cross-sectional sample preparation and examination (not to scale), (b), (d) and (c), (e) two sets of cross-sectional TEM images from two regions shown in (a), and (f) and (g) top view SEM images from the same positions as (b) and (c). The scale bar is indicated in each image.

As mentioned in the previous subsection, a temperature gradient exists between samples prepared from the 5-8 mm and 15-18 mm away from the low T end. When diborane gas is introduced, most of it gets decomposed at the entrance of the heated tube. So, at the inlet, boron-containing reactants are in the higher concentration and decrease towards the higher temperature substrate in the tube as shown in the schematic diagram in Figure 4.4. Thus, Figure 4.17 (b) and (d) are slightly different than (c) and (e). Samples at higher temperatures are more porous and particles are more diffused into the SiO₂ layer compared to the sample at 5-8 mm away from the low T end.

4.2.5 Effect of Methane

Referring back to Table 4.1, condition 4 includes all the parameters except for B₂H₆. Similar to the other conditions, multiple cross-sectional samples were prepared from two regions, 5-8 mm and 15-18 mm away from the low T and as shown in the schematic drawing in Figure 4.18 (a). Representative cross-sectional TEM images from two regions are presented in Figure 4.18 (b) and (c). Nanostructures (marked with white arrows) and dark catalyst particles can be observed from both regions. Also, some particles can be seen diffused into the SiO₂ layer (marked by orange arrows). Particles are associated with nanostructured channels/voids as seen from the contrast with the SiO₂ layer. Those channels can also be indicative of nanowires as their diameters are equivalent to the sizes of the particles.

As discussed for condition 2, deposited Ni film agglomerates, and possibly reacts with SiO₂ layer. Diffused particles with nanostructures/voids can be the result of the reaction between Ni and SiO₂. However, the number of diffused particles is much less than that of condition 2, which indicates that the reaction between Ni and SiO₂ is not dominant after adding methane. Also, unlike condition 3, the porous structure could not be observed in the SiO₂ layer. The composition of the particles is likely to be Ni_xSi_y, and nanostructures could be carbon-rich or silicon-rich. Further analysis

with EDX is required to confirm their compositions.

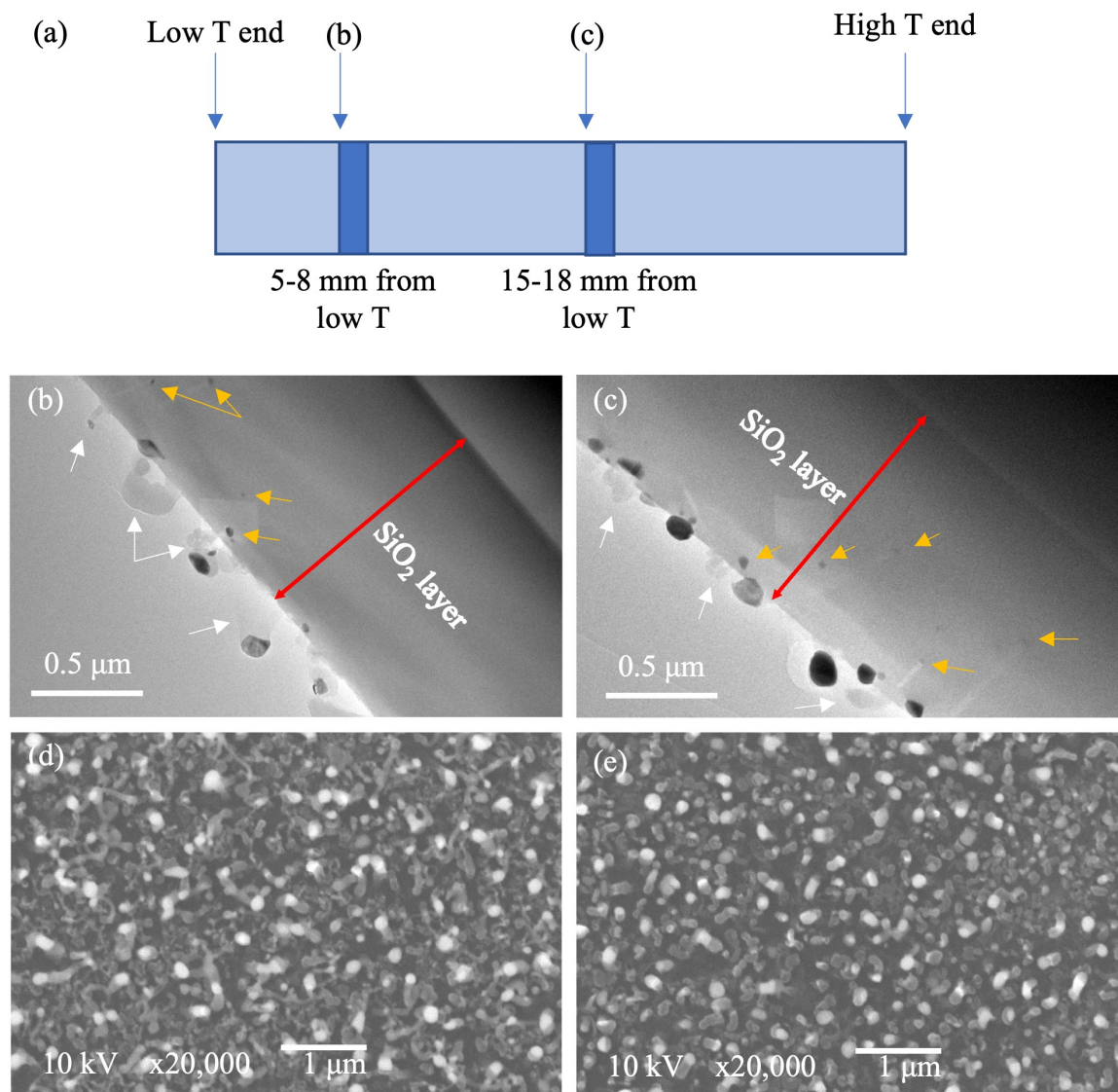


Figure 4.18: (a) Schematic drawing of the growth substrate showing two positions that were used for the cross-section sample preparation and examination (not to scale), (b) and (c) cross-sectional TEM images from two positions shown in (a), and (d) and (e) top view SEM images from the similar positions as (b) and (c). The scale bar is indicated in each image.

Top-view SEM images in Figure 4.18 (d) and (e) correspond with TEM images, and a contrast between the bright particles and dark nanostructures can be clearly seen. However, both SEM and TEM images are similar in both regions. In other words, not much difference could be observed due to small temperature variation as

seen for conditions 2 and 3.

4.2.6 Boron Carbide Nanostructures Without Catalyst

In condition 5, samples were prepared with both B_2H_6 and CH_4 gas flow but in the absence of Ni. Similar to the other samples, cross-sectional TEM images and top-view SEM images from two regions (5-8 mm and 15-18 mm away from the low T end) are presented in Figure 4.19 for comparison. From Figure 4.19 (b) and (c), thin films and nanostructures can be observed in both samples. SiO_2 layer is indicated approximately which matches with the SiO_2 layer thickness from other previous samples, and a clear contrast exists between SiO_2 layer and thin films. Thin films and nanostructures are most likely to be boron carbides (B_xC_y). B_xC_y film and nanostructures in the first image are thicker in width than that of the second one. As mentioned before, temperature and concentration gradients exist between the two regions. Pyrolysis of diborane occurs at the inlet of the reaction chamber, resulting in a decrease in B concentration from the inlet towards the center of the reaction chamber. On the other hand, pyrolysis of methane increases with temperature. Based on the temperature and concentration variation, film and nanostructures can be assumed to be as boron rich and carbon-rich B_xC_y respectively in the relatively low temperature (5-8 mm from low T) and high temperature (15-18 mm from low T). EDX analysis is required to confirm this hypothesis.

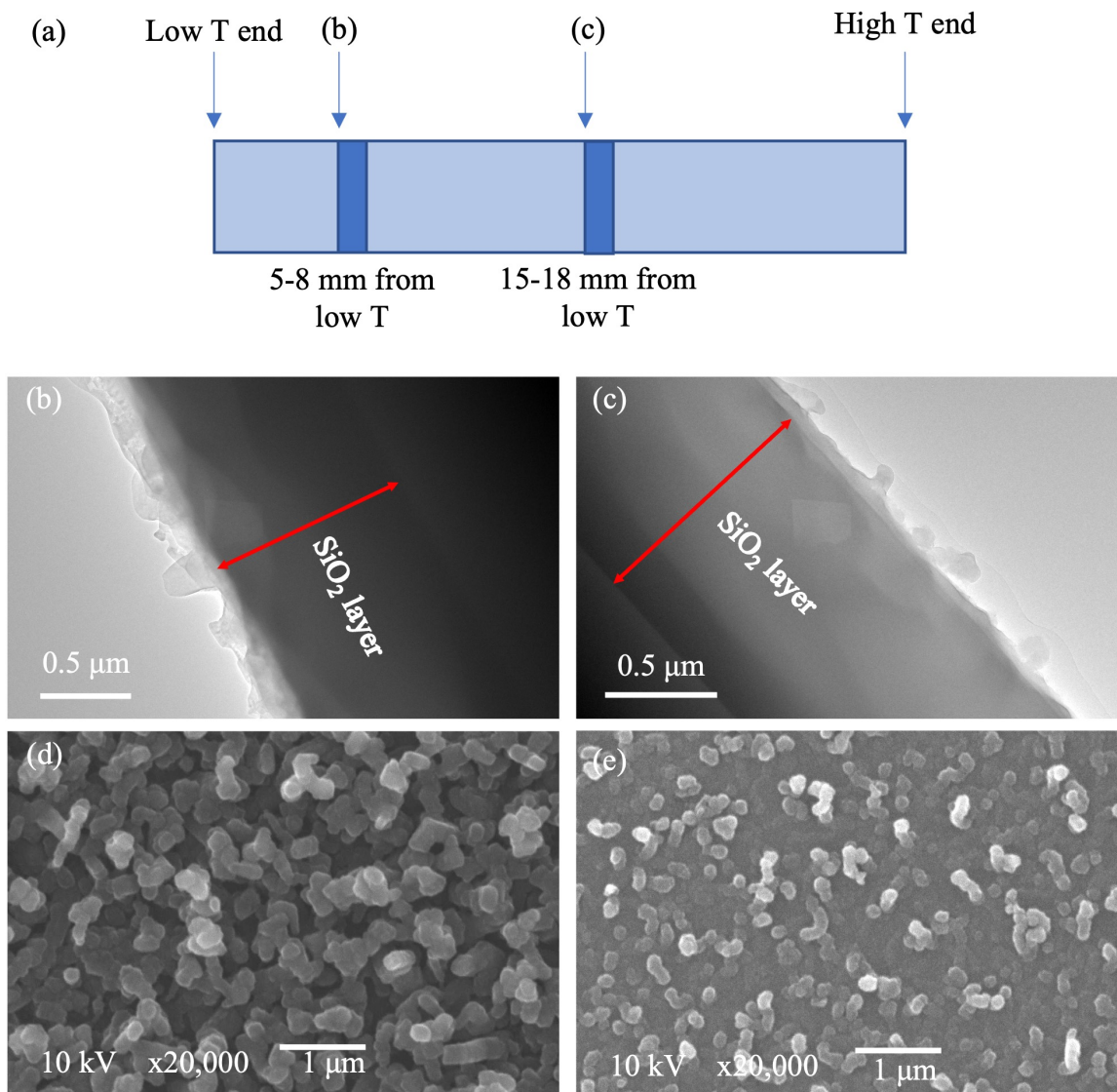


Figure 4.19: (a) Schematic drawing of the growth substrate showing two positions that were used for the cross-section sample preparation and examination (not to scale), (b) and (c) cross-sectional TEM images from two positions shown in (a), and (d) and (e) top view SEM images from the same positions as (b) and (c). The scale bar is indicated in each image.

High magnification images were obtained for the nanostructures in Figure 4.19 (b) and (c) and presented in Figure 4.20. From Figure 4.20 (a), both polycrystalline and amorphous structures can be seen in the nanostructure and confirmed by the diffraction pattern in the inset. From Figure 4.20 (b), the amorphous structure can be seen at high magnification. So, based on the current findings, in the absence of the

catalyst (Ni), single crystalline boron carbide could not be observed in both regions.

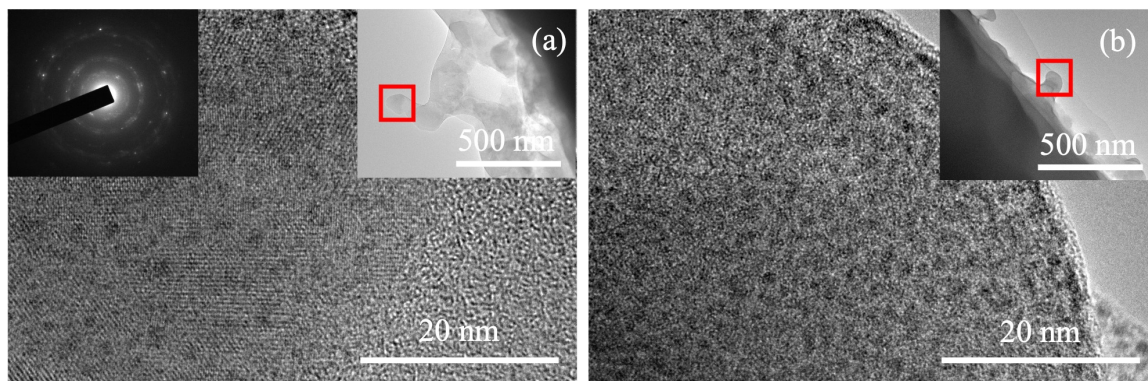


Figure 4.20: (a) High magnification TEM image from the first sample (5-8 mm away from the low T end) with DP and low magnification image in the inset, (b) high magnification TEM image of the second sample (15-18 mm away from the low T end) with low magnification image in the inset.

4.2.7 Cross-sectional Examination of Nanowires

In condition 6, cross-sectional samples were prepared from three regions of the substrate which was prepared with all the reactants. Cross-sectional TEM images and corresponding SEM images are presented in Figure 4.21. Nanostructures generated in different locations have different morphology due to the temperature and concentration gradients as mentioned before. From Figure 4.21 (b) and (e), column-like and relatively large structures can be seen while the width/ diameter of the nanostructures reduces towards the higher temperature end (Figure 4.21 (d) and (g)).

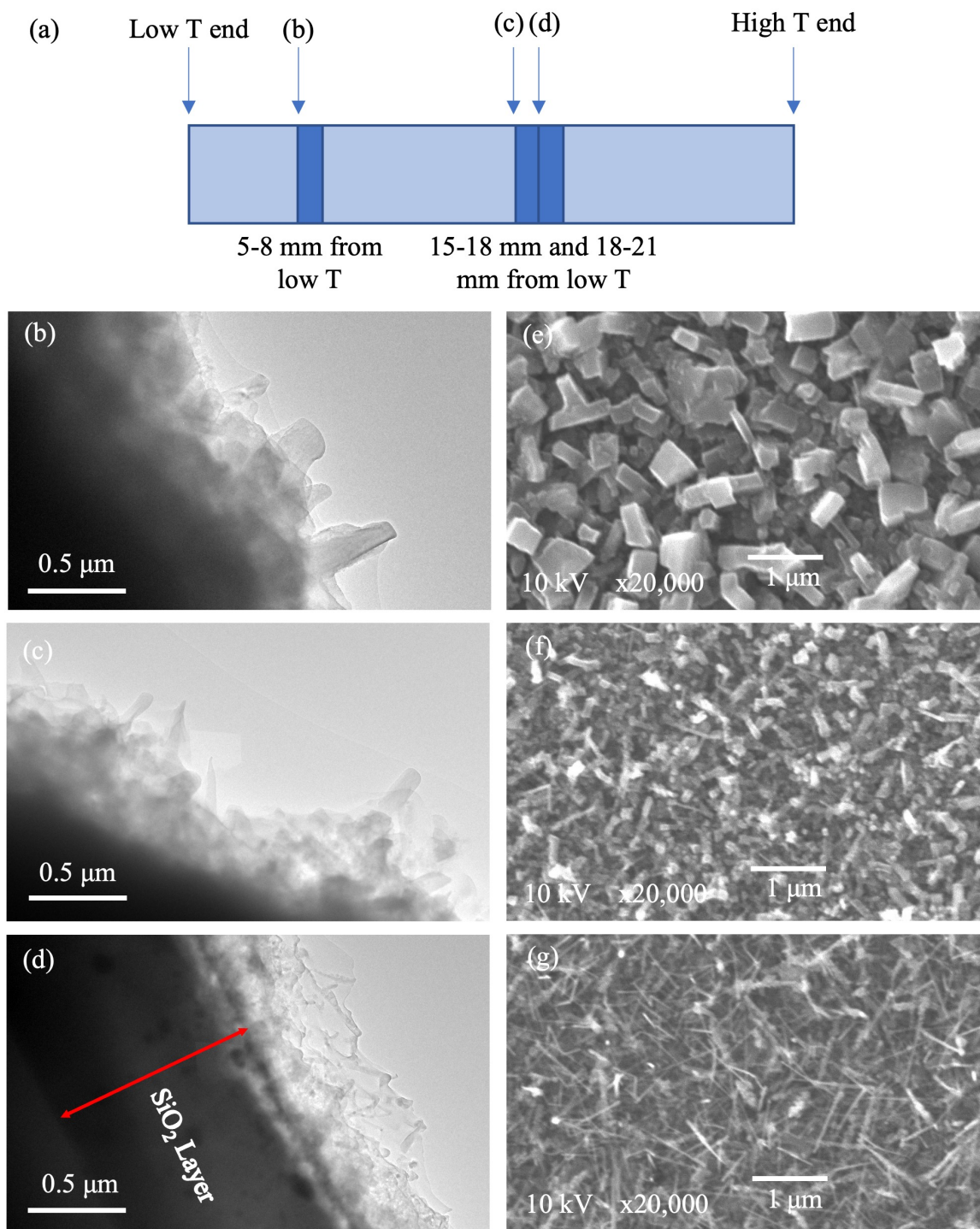


Figure 4.21: (a) Schematic drawing of the growth substrate showing three positions that were used for the cross-section sample preparation and examination (not to scale), (b), (c) and (d) cross-sectional TEM images from the three positions shown in (a), and (e), (f) and (g) top view SEM images from the same positions as (b), (c) and (d). The scale bar is indicated in each image.

One of the major goals of the cross-sectional examination was to study the nanowire-substrate interface. However, from Figure 4.21 (d), 1 μm SiO_2 layer can be clearly seen and nanowires grow on this layer. Also, due to the overlapping nanowires, the interface cannot be observed clearly at a higher magnification. Thus, the epitaxial relationship between nanowire and substrate could not be studied. Catalytic particles can be seen diffused into the SiO_2 layer.

High magnification images from the above samples are presented in Figure 4.22. From the first sample, large column-like structures could be tilted to a low zone axis and high-resolution images could be obtained as shown in Figure 4.22 (a). After indexing the DP, it matches with the $[01\bar{3}]$ zone axis of boron carbide.

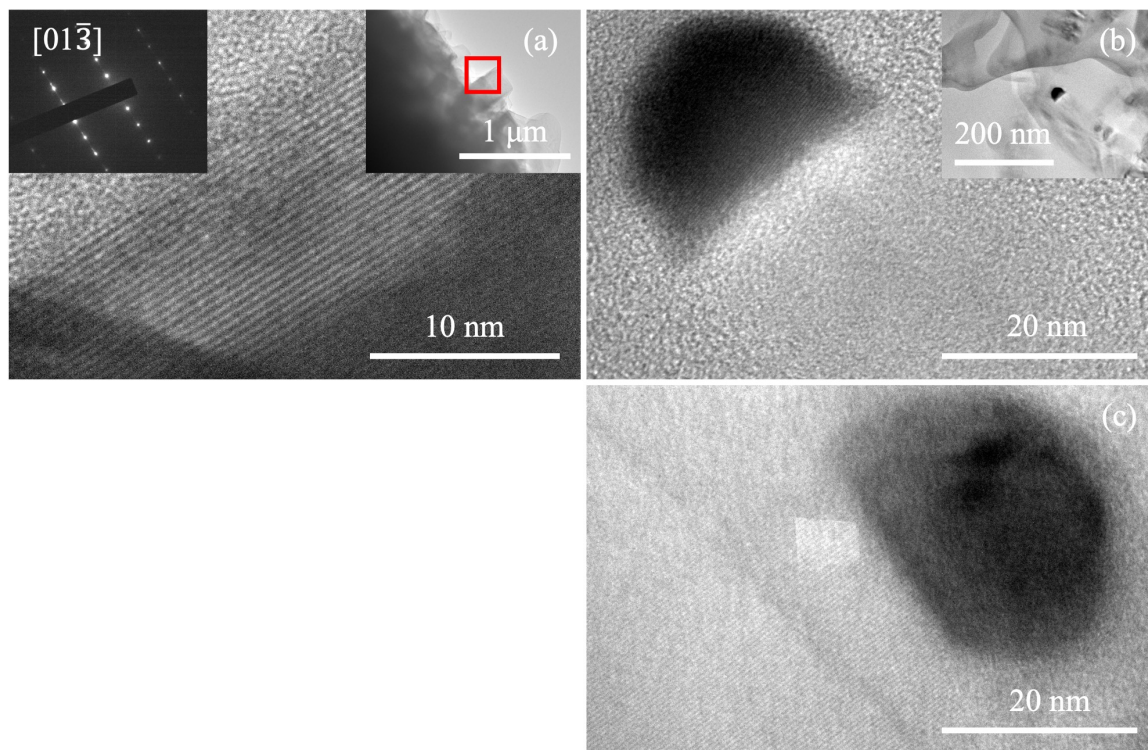


Figure 4.22: (a) HRTEM image, DP and low magnification image of a column-like structure from the first sample (5-8 mm away from the low T end), (b) and (c) high magnification images of two nanowires from the third sample (18-21 mm away from the low T end).

Another goal of the cross-sectional examination was to study the nanowire-catalyst interface. Two nanowires at high magnification are presented in Figure 4.22 (b) and

(c). From (b) nanowire-catalyst interface could be seen clearly, however, NW cannot be focused at the same time. On the other hand, the interface is not clear for the second nanowire in the (c). Also, these nanowires are too thin (≈ 30 nm), and m-bond in the background, and sometimes, overlapping nanowires pose it as more challenging to obtain DP and HRTEM images.

4.2.8 Effect of Reaction Time

Table 4.3: List of experimental conditions of varying reaction time and with other parameters (substrate (Si/ SiO₂), temperature (1050 °C), reaction gases (15 sccm B₂H₆, 15 sccm CH₄), and carrier gas (15 sccm Ar)) as constants.

Condition	Reaction time (minutes)
1	5
2	15

Table 4.3 presents two conditions of different reaction times and with other reaction parameters as constants and Figure 4.23 presents images collected from samples prepared in those two conditions. Figure 4.23 (a) and (b) represent samples prepared in five minutes of reaction time. From (a), short NWs can be seen with catalyst particles. Even for this short reaction time, catalyst migration and kink formation can be observed as indicated in Figure 4.23 (a). Such information could not be obtained from the SEM image (Figure 4.23 (b)), because formed NWs and kinks are too small at this condition.

Figure 4.23 (c) and (d) presents TEM and SEM images from the other condition. From TEM images, NWs can be observed (marked with white arrows). High-resolution images could not be obtained because of the higher thickness of the sample. Inset in Figure 4.23 (c) shows a kinked NW with catalyst. From the SEM image (Figure 4.23 (d)) NWs can be observed but kinks are not clearly visible.

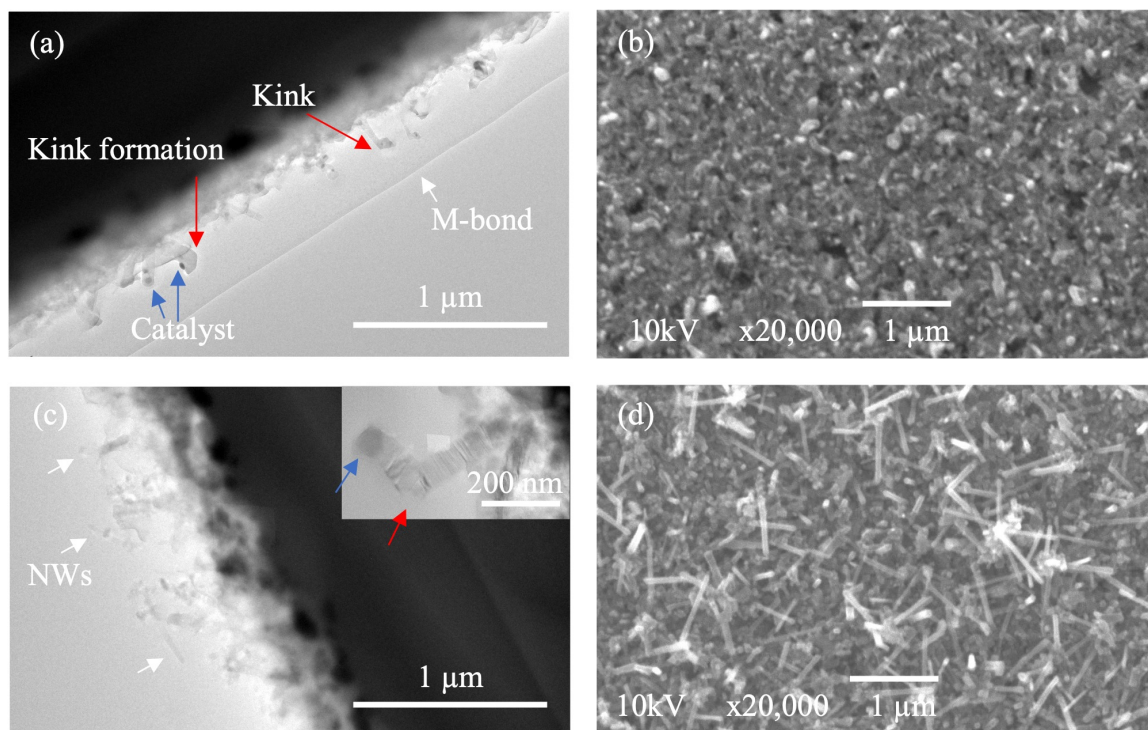


Figure 4.23: Cross-sectional TEM images and top-view SEM images from two conditions of varying reaction time and other reaction parameters as constants. (a) and (b) represents images from samples prepared in five minutes of reaction time, and (c) and (d) are images from samples prepared in fifteen minutes.

4.2.9 Summary and Hypothesis of Growth Mechanism

To summarize all the conditions discussed above, Figure 4.24 and 4.25 are presented with cross-sectional TEM images from the relatively low and high-temperature regions.

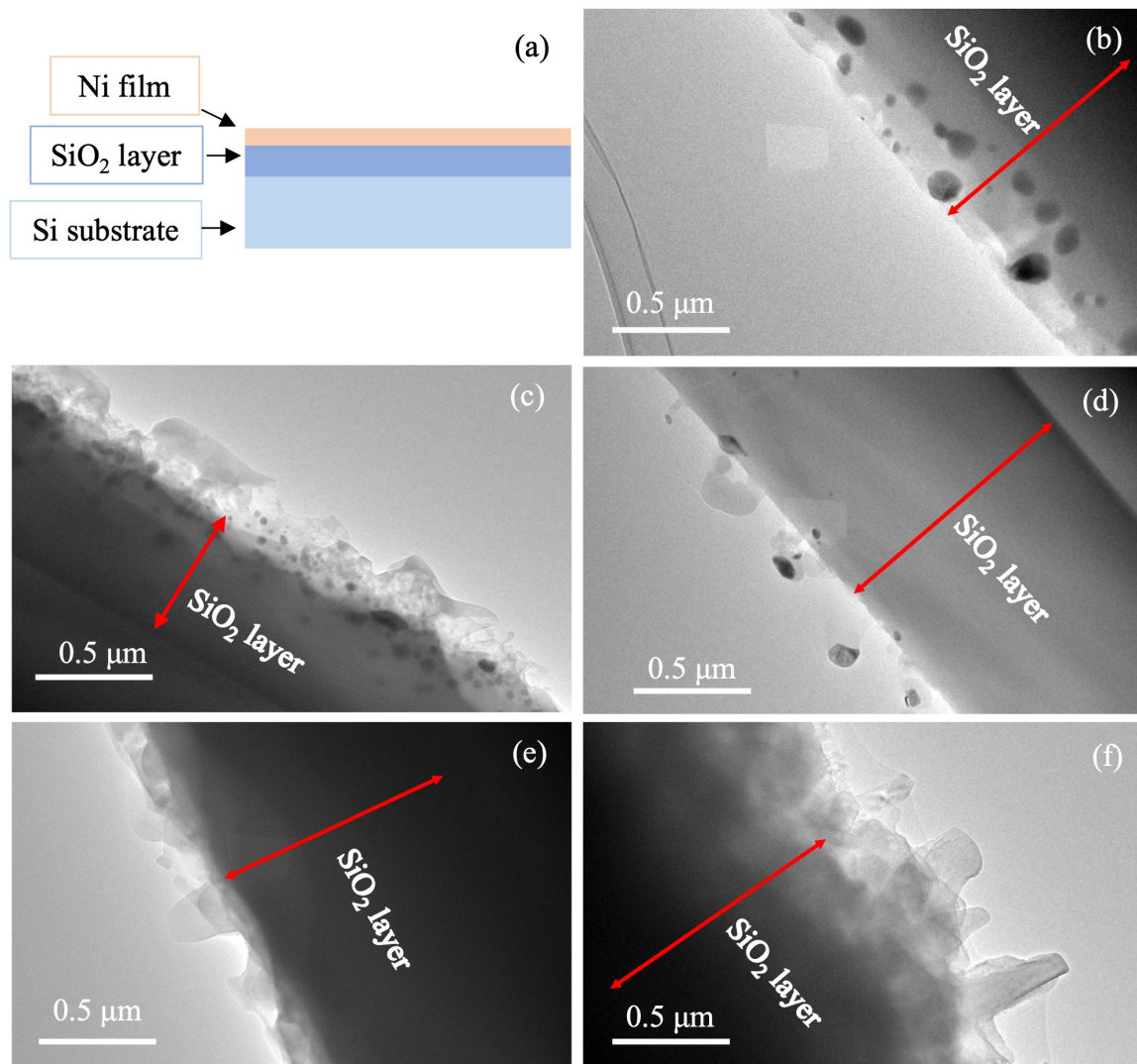


Figure 4.24: Summary of all conditions from the relatively low-temperature region. (a) Schematic drawing (not to scale) of the Ni/SiO₂/Si stack before annealing, (b) cross-sectional TEM image after annealing of (a), (c) After annealing of (a), while adding diborane to the reaction chamber, (d) After annealing of (a) while introducing methane to the reaction chamber, (e) After annealing of SiO₂/Si substrate with diborane and methane flow but without Ni film, (f) After annealing of (a) with both diborane and methane flow. A scale bar is included in each image.

Figure 4.24 (a) represents a schematic of the Ni/SiO₂/Si layers before annealing. As mentioned before, annealing temperature range for T₂ region in Figure 4.4 is ≈ 908 - 931°C . We can assume that in the 5-8 mm region from low T, the annealing temperature is $\approx 908^\circ$ for the purpose of comparison. Annealing was performed on the Ni/SiO₂/Si stack in all the conditions except for Figure 4.24 (e). After annealing,

agglomeration of Ni film into particles and diffusion of those particles in the SiO₂ with void formation could be seen in Figure 4.24 (b) (details were discussed in section 4.2.3). Particles could also be seen in other conditions (Figure 4.24 (c), and (d)). Due to the overlapping layers, particles could not be seen in Figure 4.24 (e). The assumption is that particles would be visible if a better-quality sample could be prepared. From Figure 4.24 (c), diborane seems to etch the SiO₂ layer, which might have facilitated the diffusion of the particles. More particles are diffused and diffusion depth is higher in this case. On the other hand, Methane flow generated catalyst-assisted nanostructures, and as a result, suppressing/reducing the number of particles that diffused into the SiO₂ layer (Figure 4.24 (d)).

Thicknesses of SiO₂ layer observed in all the images were measured for the comparison (TEM images are not calibrated with standard calibration samples, so measured thicknesses are not absolute, but can be used for comparison with each other). SiO₂ layers shown in the Figure 4.24 (b-f) are comparable and close to 1 μm except for the (c), where thickness varied and significantly lower than 1 μm . This could be caused due to the etching of SiO₂ by diborane.

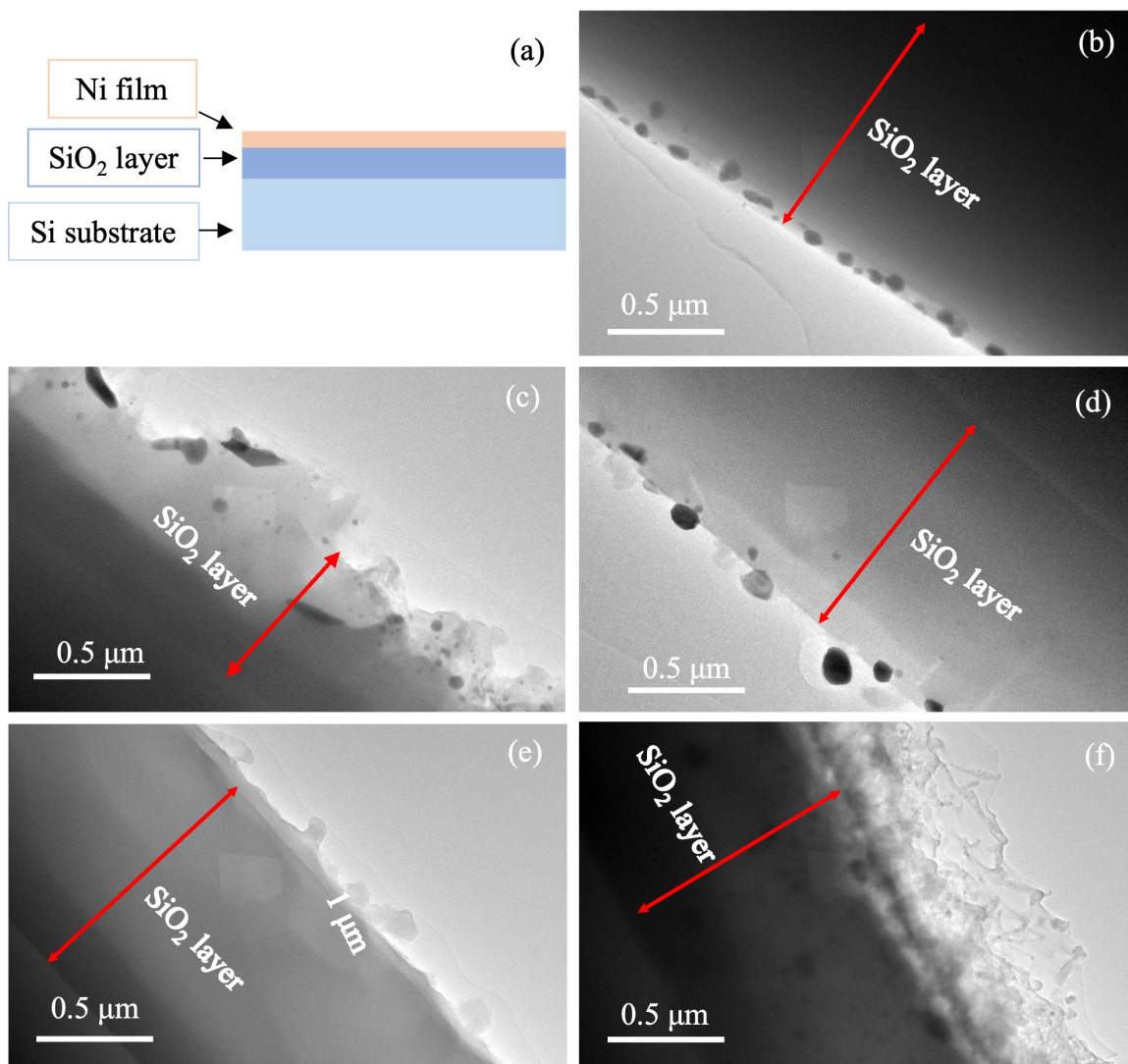


Figure 4.25: Summary of all conditions from the relatively high-temperature region. (a) Schematic drawing (not to scale) of the Ni/SiO₂/Si stack before annealing, (b) cross-sectional TEM image after annealing of (a), (c) After annealing of (a) while adding diborane to the reaction chamber, (d) After annealing of (a), while introducing methane to the reaction chamber, (e) After annealing of SiO₂/Si substrate with diborane and methane flow but without Ni film, (f) After annealing of (a) with both diborane and methane flow. A scale bar is included in each image.

Similar to Figure 4.24, Figure 4.25 is presented by combining all the conditions from the relatively high-temperature region. Again, we can assume that the annealing temperature in this region is $\approx 931^\circ\text{C}$. The effect of reaction parameters is mainly similar between the two regions. But as mentioned in section 4.2.3, due to small temperature variation, differences in the diffusion depth of the agglomerated particles

and void density could be seen between two regions (Figure 4.24 (b) and 4.25 (b)). The effect of diborane and methane is similar to the ones mentioned previously. Also, particles could be seen diffused into the SiO₂ layer in Figure 4.25 (f) where all reaction parameters are present.

Layer thicknesses were comparable except for the Figure 4.25 (c) due to etching of SiO₂ by diborane. Based on the above and previous discussion, a hypothesis for the growth mechanism of boron carbide nanowires can be formulated. Three major steps: (i) reaction of the catalyst with the precursor, (ii) diffusion of the catalyst into the SiO₂ (iii) formation of B_xC_y film and nanowires. Pyrolysis of diborane generates B and H₂. If B or H₂ were responsible for the etching of the SiO₂, etching would occur in condition 5 as well. So, it can be hypothesized that reactive species generated due to the catalyst cause the etching of the SiO₂. In the case of condition 4, fewer defects/microchannels and particle diffusion could be observed. This implies that catalyst-assisted nanostructure formation is more favorable in the presence of CH₄ than defect formation and particle diffusion. Both precursor gases and the catalyst are present in condition 6 and dominant reactions determine the end product. Etching due to the reaction of Ni and diborane is possible but cannot be seen. This indicates that etching is suppressed because the reaction between diborane and methane is preminent in the presence of the catalyst and quickly forms the B_xC_y films. But particle diffusion can still be seen in this condition. Further investigation is required to verify the hypothesis. For example, would etching occur in the presence of diborane but without a catalyst on the substrate? Determination of the composition of the particles could establish the nature of the reactions and strengthen the hypothesis based on the dominant reactions.

Between relatively low and high-temperature regions, there are also gradients of boron and carbon concentrations. Boron concentration starts to decrease from the low T end towards the high T zone. On the contrary, carbon concentration increases

towards higher temperatures. These temperature and concentration gradients caused the following differences: (i) in condition 3, film-like nanostructures can be seen on top of the porous structure in the low-temperature region (Figure 4.24 (c)) as opposed to the other. This might be caused due to slightly higher boron concentration in this region. (ii) In conditions 5 and 6, nanostructures formed on the thin film are column-like in the low-temperature region (Figure 4.24 (e-f)) as opposed to the other where nanostructures are of higher aspect ratio (Figure 4.25 (e-f)). This could be due to the high concentration of boron in the low temperature predominantly forming B_xC_y thin film first and growing column-like nanostructures from it. On the other hand, in the relatively higher temperature region, higher aspect ratio nanostructures could form due to a relatively lower concentration of boron.

CHAPTER 5: CONCLUSIONS

5.1 Conclusions

In this dissertation, 1D NWs were examined using TEM-based techniques to develop a structure-property relationship and explore the growth mechanism of the NWs. First, as a part of the collaborative project, lattice constants of ultra-thin NbSe₃ NWs were determined to correlate them with the dimension and unusual thermal properties of the NWs. From the obtained results, such a correlation could not be obtained. Thus, the structural effect was eliminated from the superdiffusive phonon transport observed in the ultra-thin NWs, and it led to considering other factors for such properties.

Secondly, TEM-based structural characterization was performed extensively to understand the growth mechanism of boron carbide NWs. The effect of different reaction parameters such as catalyst, precursors (diborane and methane), annealing temperature, and time was explored. Catalyst-substrate interaction could be observed during the annealing of 2 nm Ni film on the SiO₂/Si substrate. Ni film agglomerated into particles and diffused into SiO₂ layer. The contrast in the TEM images shows that some of the particles are inside the voids. It was hypothesized that during high-temperature annealing, diffusion of Ni occurs through the microchannels in the SiO₂ and nucleates the voids. However, with increasing temperature, agglomeration and void nucleation and growth show counter-intuitive behavior. The reason behind this is not known yet.

In the next step, when the Ni-coated substrate is annealed, diborane is added to the chamber, which results in a highly porous structure and increases the diffusion of the particles in the SiO₂ layer. Temperature and concentration gradient impacts the

two regions of the same substrate and a more porous structure could be observed at the slightly higher temperature. On the other hand, with high boron concentration in the relatively lower temperature region can be re-deposit as a thin film on top of the porous structure. Separately, the effect of methane introduction to the chamber during annealing of the Ni-coated substrate shows the opposite effect compared to the diborane. Some nanostructures grow with catalytic particles on top of them but no porous structure could be seen. Some voids and diffusion of particles still could be seen but in a less number. Because of the opposite effect, when methane and diborane are added simultaneously (without Ni film), a thin film along with nanostructures could be found. The nanostructures are polycrystalline or amorphous structures. Lastly, from the cross-sectional examination of the NW sample, a thin film can be seen to grow between the NW and SiO₂ layer which could be due to a reaction between diborane and methane, and from this film, NWs could be growing. Although some information is lacking to verify the hypothesis, cross-sectional TEM images of multiple conditions presented in this dissertation provide useful data and insights that fill the gaps in the knowledge and generate more unanswered questions.

5.2 Future Works

Future works are recommended for the growth mechanism of boron carbide NWs. Side-view cross-sectional TEM images and SEM images of samples from different conditions provide helpful information but fail to provide a complete picture. Further investigation is required to validate the hypothesis presented in the previous chapter.

The first recommendation is to obtain EDX data in the particles/films observed in different experimental conditions as mentioned in Chapter 4. Elemental information along with HRTEM and DP analysis could help to narrow down the chemical composition of the particles and specify predominant reactions that lead to the B_xC_y film formation and NW growth. Thus, it would verify the validity of the hypothesis or can lead to other directions currently not considered. Secondly, additional sam-

ple preparation in the CVD chamber and their cross-sectional examination can be performed to obtain the necessary data. For example, samples from adding diborane and methane gases in the chamber without the catalyst on the substrate can show how the precursor gases react with the substrate.

Thirdly, the NW-substrate interface is not clear from the current NW sample grown on SiO_2/Si substrate and no epitaxy could be observed in the interface. Cross-sectional samples can be prepared from NWs grown on sapphire (Al_2O_3) substrate. NW-substrate interface for sapphire might be relatively clean and epitaxial growth is also possible. This can be predicted because sapphire is crystalline whereas SiO_2 is amorphous. However, it is worth mentioning that preparing cross-sectional samples from the sapphire substrate by mechanical grinding, dimpling, and ion milling is extremely challenging compared to the SiO_2/Si substrate because of the high hardness of sapphire.

REFERENCES

- [1] Z. Cui, *Characterization of individual straight and kinked boron carbide nanowires*. PhD thesis, The University of North Carolina at Charlotte, 2016.
- [2] C. M. Lieber, “One-dimensional nanostructures: chemistry, physics & applications,” *Solid state communications*, vol. 107, no. 11, pp. 607–616, 1998.
- [3] J. N. Tiwari, R. N. Tiwari, and K. S. Kim, “Zero-dimensional, one-dimensional, two-dimensional and three-dimensional nanostructured materials for advanced electrochemical energy devices,” *Progress in Materials Science*, vol. 57, no. 4, pp. 724–803, 2012.
- [4] P. I. Dolez, “Nanomaterials definitions, classifications, and applications,” in *Nanoengineering*, pp. 3–40, Elsevier, 2015.
- [5] Y. Xia, P. Yang, Y. Sun, Y. Wu, B. Mayers, B. Gates, Y. Yin, F. Kim, and H. Yan, “One-dimensional nanostructures: synthesis, characterization, and applications,” *Advanced materials*, vol. 15, no. 5, pp. 353–389, 2003.
- [6] R. Wagner and W. Ellis, “Vapor-liquid-solid mechanism of single crystal growth,” *Applied physics letters*, vol. 4, no. 5, pp. 89–90, 1964.
- [7] E. Garnett, L. Mai, and P. Yang, “Introduction: 1d nanomaterials/nanowires,” *Chemical reviews*, vol. 119, no. 15, pp. 8955–8957, 2019.
- [8] P. Yang, R. Yan, and M. Fardy, “Semiconductor nanowire: what’s next?,” *Nano letters*, vol. 10, no. 5, pp. 1529–1536, 2010.
- [9] A. L. Roest, M. A. Verheijen, O. Wunnicke, S. Serafin, H. Wondergem, and E. P. Bakkers, “Position-controlled epitaxial iii–v nanowires on silicon,” *Nanotechnology*, vol. 17, no. 11, p. S271, 2006.
- [10] M. Kwiat, S. Cohen, A. Pevzner, and F. Patolsky, “Large-scale ordered 1d-nanomaterials arrays: Assembly or not?,” *Nano Today*, vol. 8, no. 6, pp. 677–694, 2013.
- [11] N. P. Dasgupta, J. Sun, C. Liu, S. Brittman, S. C. Andrews, J. Lim, H. Gao, R. Yan, and P. Yang, “25th anniversary article: semiconductor nanowires—synthesis, characterization, and applications,” *Advanced materials*, vol. 26, no. 14, pp. 2137–2184, 2014.
- [12] N. Wang, Y. Cai, and R. Zhang, “Growth of nanowires,” *Materials Science and Engineering: R: Reports*, vol. 60, no. 1-6, pp. 1–51, 2008.
- [13] J. Hannon, S. Kodambaka, F. Ross, and R. Tromp, “The influence of the surface migration of gold on the growth of silicon nanowires,” *nature*, vol. 440, no. 7080, pp. 69–71, 2006.

- [14] C. Kuo and C. Gau, "Vapor–solid–solid growth of crystalline silicon nanowires using anodic aluminum oxide template," *Thin solid films*, vol. 519, no. 11, pp. 3603–3607, 2011.
- [15] S. V. Thombare, A. F. Marshall, and P. C. McIntyre, "Kinetics of germanium nanowire growth by the vapor-solid-solid mechanism with a ni-based catalyst," *APL Materials*, vol. 1, no. 6, p. 061101, 2013.
- [16] C. B. Maliakkal, M. Tornberg, D. Jacobsson, S. Lehmann, and K. A. Dick, "Vapor–solid–solid growth dynamics in gaas nanowires," *Nanoscale Advances*, vol. 3, no. 20, pp. 5928–5940, 2021.
- [17] M. Mittal, S. Sardar, and A. Jana, "Nanofabrication techniques for semiconductor chemical sensors," in *Handbook of Nanomaterials for Sensing Applications*, pp. 119–137, Elsevier, 2021.
- [18] L. Xia, "Importance of nanostructured surfaces," in *Bioceramics*, pp. 5–24, Elsevier, 2021.
- [19] M. Pant, R. Singh, P. Negi, K. Tiwari, and Y. Singh, "A comprehensive review on carbon nano-tube synthesis using chemical vapor deposition," *Materials Today: Proceedings*, 2021.
- [20] D. Wang and H. Dai, "Low-temperature synthesis of single-crystal germanium nanowires by chemical vapor deposition," *Angewandte Chemie International Edition*, vol. 41, no. 24, pp. 4783–4786, 2002.
- [21] H. O. Pierson, *Handbook of chemical vapor deposition: principles, technology and applications*. William Andrew, 1999.
- [22] A. C. Jones and M. L. Hitchman, *Chemical vapour deposition: precursors, processes and applications*. Royal society of chemistry, 2009.
- [23] P. Schmidt, M. Binnewies, R. Glaum, and M. Schmidt, *Chemical vapor transport reactions–methods, materials, modeling*. InTech Rijeka, Croatia, 2013.
- [24] K. Ikejiri, J. Noborisaka, S. Hara, J. Motohisa, and T. Fukui, "Mechanism of catalyst-free growth of gaas nanowires by selective area movpe," *Journal of Crystal Growth*, vol. 298, pp. 616–619, 2007.
- [25] B. B. Salzman, M. M. van der Sluijs, G. Soligno, and D. Vanmaekelbergh, "Oriented attachment: From natural crystal growth to a materials engineering tool," *Accounts of chemical research*, vol. 54, no. 4, pp. 787–797, 2021.
- [26] Z. Tang, N. A. Kotov, and M. Giersig, "Spontaneous organization of single cdte nanoparticles into luminescent nanowires," *Science*, vol. 297, no. 5579, pp. 237–240, 2002.

- [27] S. Barth, F. Hernandez-Ramirez, J. D. Holmes, and A. Romano-Rodriguez, "Synthesis and applications of one-dimensional semiconductors," *Progress in Materials Science*, vol. 55, no. 6, pp. 563–627, 2010.
- [28] D. Rawtani, T. Sajan, A. Twinkle R, and Y. Agrawal, "Emerging strategies for synthesis and manipulation of nanowires: a review.," *Reviews on advanced materials science*, vol. 40, no. 2, 2015.
- [29] C. Jia, Z. Lin, Y. Huang, and X. Duan, "Nanowire electronics: from nanoscale to macroscale," *Chemical reviews*, vol. 119, no. 15, pp. 9074–9135, 2019.
- [30] X. Duan, Y. Huang, Y. Cui, J. Wang, and C. M. Lieber, "Indium phosphide nanowires as building blocks for nanoscale electronic and optoelectronic devices," *nature*, vol. 409, no. 6816, pp. 66–69, 2001.
- [31] Y. Huang, X. Duan, and C. M. Lieber, "Nanowires for integrated multicolor nanophotonics," *Small*, vol. 1, no. 1, pp. 142–147, 2005.
- [32] Y. Huang, X. Duan, Y. Cui, L. J. Lauhon, K.-H. Kim, and C. M. Lieber, "Logic gates and computation from assembled nanowire building blocks," *Science*, vol. 294, no. 5545, pp. 1313–1317, 2001.
- [33] B. Tian and C. M. Lieber, "Nanowired bioelectric interfaces: Focus review," *Chemical reviews*, vol. 119, no. 15, pp. 9136–9152, 2019.
- [34] Y. Cui, Q. Wei, H. Park, and C. M. Lieber, "Nanowire nanosensors for highly sensitive and selective detection of biological and chemical species," *science*, vol. 293, no. 5533, pp. 1289–1292, 2001.
- [35] A. Mukherjee and Y. Rosenwaks, "Recent advances in silicon fet devices for gas and volatile organic compound sensing," *Chemosensors*, vol. 9, no. 9, p. 260, 2021.
- [36] M. Nehra, N. Dilbaghi, G. Marrazza, A. Kaushik, R. Abolhassani, Y. K. Mishra, K. H. Kim, and S. Kumar, "1d semiconductor nanowires for energy conversion, harvesting and storage applications," *Nano Energy*, p. 104991, 2020.
- [37] A. I. Hochbaum and P. Yang, "Semiconductor nanowires for energy conversion," *Chemical reviews*, vol. 110, no. 1, pp. 527–546, 2010.
- [38] B. Tian, X. Zheng, T. J. Kempa, Y. Fang, N. Yu, G. Yu, J. Huang, and C. M. Lieber, "Coaxial silicon nanowires as solar cells and nanoelectronic power sources," *nature*, vol. 449, no. 7164, pp. 885–889, 2007.
- [39] Z. Li, H. H. Tan, C. Jagadish, and L. Fu, "Iii–v semiconductor single nanowire solar cells: a review," *Advanced Materials Technologies*, vol. 3, no. 9, p. 1800005, 2018.

- [40] Z. Zhong, Z. Li, Q. Gao, Z. Li, K. Peng, L. Li, S. Mokkapati, K. Vora, J. Wu, G. Zhang, *et al.*, "Efficiency enhancement of axial junction inp single nanowire solar cells by dielectric coating," *Nano Energy*, vol. 28, pp. 106–114, 2016.
- [41] I. Åberg, G. Vescovi, D. Asoli, U. Naseem, J. P. Gilboy, C. Sundvall, A. Dahlgren, K. E. Svensson, N. Anttu, M. T. Björk, *et al.*, "A gaas nanowire array solar cell with 15.3% efficiency at 1 sun," *IEEE Journal of photovoltaics*, vol. 6, no. 1, pp. 185–190, 2015.
- [42] M. Law, L. E. Greene, J. C. Johnson, R. Saykally, and P. Yang, "Nanowire dye-sensitized solar cells," *Nature materials*, vol. 4, no. 6, pp. 455–459, 2005.
- [43] M. Zi, M. Zhu, L. Chen, H. Wei, X. Yang, and B. Cao, "Zno photoanodes with different morphologies grown by electrochemical deposition and their dye-sensitized solar cell properties," *Ceramics international*, vol. 40, no. 6, pp. 7965–7970, 2014.
- [44] D. Lee, Y. Rho, F. I. Allen, A. M. Minor, S. H. Ko, and C. P. Grigoropoulos, "Synthesis of hierarchical tio 2 nanowires with densely-packed and omnidirectional branches," *Nanoscale*, vol. 5, no. 22, pp. 11147–11152, 2013.
- [45] Z. L. Wang, "Characterizing the structure and properties of individual wire-like nanoentities," *Advanced Materials*, vol. 12, no. 17, pp. 1295–1298, 2000.
- [46] G. Bussone, H. Schäfer-Eberwein, E. Dimakis, A. Biermanns, D. Carbone, A. Tahraoui, L. Geelhaar, P. Haring Bolívar, T. U. Schüllli, and U. Pietsch, "Correlation of electrical and structural properties of single as-grown gaas nanowires on si (111) substrates," *Nano Letters*, vol. 15, no. 2, pp. 981–989, 2015.
- [47] V. Rodrigues, J. Bettini, A. Rocha, L. G. Rego, and D. Ugarte, "Quantum conductance in silver nanowires: Correlation between atomic structure and transport properties," *Physical Review B*, vol. 65, no. 15, p. 153402, 2002.
- [48] Z. L. Wang, "New developments in transmission electron microscopy for nanotechnology," *Advanced Materials*, vol. 15, no. 18, pp. 1497–1514, 2003.
- [49] A. M. Morales and C. M. Lieber, "A laser ablation method for the synthesis of crystalline semiconductor nanowires," *Science*, vol. 279, no. 5348, pp. 208–211, 1998.
- [50] Q. Xiong, G. Chen, J. Acord, X. Liu, J. Zengel, H. Gutierrez, J. Redwing, L. Lew Yan Voon, B. Lassen, and P. Eklund, "Optical properties of rectangular cross-sectional zns nanowires," *Nano Letters*, vol. 4, no. 9, pp. 1663–1668, 2004.
- [51] A. A. Koryakin, S. A. Kukushkin, K. P. Kotlyar, E. D. Ubyivovk, R. R. Reznik, and G. E. Cirilin, "A new insight into the mechanism of low-temperature au-assisted growth of inas nanowires," *CrystEngComm*, vol. 21, no. 32, pp. 4707–4717, 2019.

- [52] M. Tchernycheva, L. Travers, G. Patriarche, F. Glas, J.-C. Harmand, G. E. Cirlin, and V. G. Dubrovskii, "Au-assisted molecular beam epitaxy of inas nanowires: Growth and theoretical analysis," *Journal of Applied Physics*, vol. 102, no. 9, p. 094313, 2007.
- [53] S. A. Dayeh, J. Wang, N. Li, J. Y. Huang, A. V. Gin, and S. T. Picraux, "Growth, defect formation, and morphology control of germanium–silicon semiconductor nanowire heterostructures," *Nano letters*, vol. 11, no. 10, pp. 4200–4206, 2011.
- [54] C.-P. Li, C.-S. Lee, X.-L. Ma, N. Wang, R.-Q. Zhang, and S.-T. Lee, "Growth direction and cross-sectional study of silicon nanowires," *Advanced materials*, vol. 15, no. 7-8, pp. 607–609, 2003.
- [55] Y. Wu, Y. Cui, L. Huynh, C. J. Barrelet, D. C. Bell, and C. M. Lieber, "Controlled growth and structures of molecular-scale silicon nanowires," *Nano letters*, vol. 4, no. 3, pp. 433–436, 2004.
- [56] K. Tomioka, J. Motohisa, S. Hara, and T. Fukui, "Control of inas nanowire growth directions on si," *Nano letters*, vol. 8, no. 10, pp. 3475–3480, 2008.
- [57] Y. Wu and P. Yang, "Direct observation of vapor- liquid- solid nanowire growth," *Journal of the American Chemical Society*, vol. 123, no. 13, pp. 3165–3166, 2001.
- [58] F. Ross, J. Tersoff, and M. Reuter, "Sawtooth faceting in silicon nanowires," *Physical review letters*, vol. 95, no. 14, p. 146104, 2005.
- [59] S. Kodambaka, J. Tersoff, M. Reuter, and F. Ross, "Diameter-independent kinetics in the vapor-liquid-solid growth of si nanowires," *Physical review letters*, vol. 96, no. 9, p. 096105, 2006.
- [60] F. Lenrick, M. Ek, D. Jacobsson, M. T. Borgström, and L. R. Wallenberg, "Fib plan and side view cross-sectional tem sample preparation of nanostructures," *Microscopy and Microanalysis*, vol. 20, no. 1, pp. 133–140, 2014.
- [61] Z. Guan, B. Cao, Y. Yang, Y. Jiang, D. Li, and T. T. Xu, "Observation of 'hidden' planar defects in boron carbide nanowires and identification of their orientations," *Nanoscale research letters*, vol. 9, no. 1, pp. 1–9, 2014.
- [62] Z. Guan, "Boron carbide nanowires: Synthesis and characterization," *Ph. D. Thesis*, 2013.
- [63] Q. Zhang, Z. Cui, Z. Wei, S. Y. Chang, L. Yang, Y. Zhao, Y. Yang, Z. Guan, Y. Jiang, J. Fowlkes, *et al.*, "Defect facilitated phonon transport through kinks in boron carbide nanowires," *Nano Letters*, vol. 17, no. 6, pp. 3550–3555, 2017.
- [64] D. B. Williams and C. B. Carter, "Transmission electron microscopy : a textbook for materials science," 2009.

- [65] Y. Leng, *Materials characterization: introduction to microscopic and spectroscopic methods*. John Wiley & Sons, 2009.
- [66] K. Akhtar, S. A. Khan, S. B. Khan, and A. M. Asiri, "Scanning electron microscopy: Principle and applications in nanomaterials characterization," in *Handbook of materials characterization*, pp. 113–145, Springer, 2018.
- [67] A. A. Hilal, "Microstructure of concrete," *High Performance Concrete Technology and Applications*, pp. 3–24, 2016.
- [68] D. J. Smith, "Chapter 1 characterization of nanomaterials using transmission electron microscopy," in *Nanocharacterisation (2)*, pp. 1–29, The Royal Society of Chemistry, 2015.
- [69] M. J. Eskandari, R. Gostariani, and M. A. Asadabad, "Transmission electron microscopy of nanomaterials," in *Electron Crystallography*, p. 9, IntechOpen, 2020.
- [70] Y. Chimupala, *Synthesis and Characterization of the TiO₂ (B) phase*. PhD thesis, University of Leeds, 2015.
- [71] T. P. Inc., "Tem/stem test specimens." https://www.tedpella.com/calibration_html/TEM_STEM_Test_Specimens.aspx, 2022.
- [72] Microscopy and analysis, "Wavelength-dispersive (x-ray) spectroscopy." http://www.laborexport.hu/_data/VFS_be564080af6d6a2942db1be5b9743e39. PDF, 2016.
- [73] Y. University, "Eds principle." <https://ywcmatsci.yale.edu/edx-principle>, 2022.
- [74] D. S. Rao, K. Muraleedharan, and C. Humphreys, "Tem specimen preparation techniques," *Microscopy: science, technology, applications and education*, vol. 2, p. 1232, 2010.
- [75] M. Measurements, "M-bond 610, strain gage adhesive for stress analysis and transducer applications." <http://www.vishaypg.com/docs/11013/bond610.pdf>, Oct. 2017.
- [76] P. Polishing, "Diamond lapping film." <https://www.precision-polishing.com/en/news/diamond-lapping-film>, June 2019.
- [77] T. P. Inc., "Pelco lapping discs, diamond and aluminum oxide." https://www.tedpella.com/Material-Sciences_html/PELCO_Lapping_Discs.htm, 2021.
- [78] W. Edge, "Lapping films - what they are and how to use them." <https://support.wickededgeusa.com/portal/en/kb/articles/lapping-films-what-they-are-and-how-to-use-them>, July 2019.

- [79] G. Inc., “Dimple grinder, model 656 user’s guide.” <http://emcfiles.missouri.edu/pdf/manuals/Model656.pdf>, Nov. 1998.
- [80] G. Inc., “Precision ion polishing system, owner’s manual and user’s guide.” <https://www.tem-analysis.com/instruction-manuals/gatan-691-pips-instruction-manual.pdf>, Feb. 2008.
- [81] L. Yang, Y. Tao, J. Liu, C. Liu, Q. Zhang, M. Akter, Y. Zhao, T. T. Xu, Y. Xu, Z. Mao, *et al.*, “Distinct signatures of electron–phonon coupling observed in the lattice thermal conductivity of nbse3 nanowires,” *Nano letters*, vol. 19, no. 1, pp. 415–421, 2018.
- [82] J. Zhou, H. D. Shin, K. Chen, B. Song, R. A. Duncan, Q. Xu, A. A. Maznev, K. A. Nelson, and G. Chen, “Direct observation of large electron–phonon interaction effect on phonon heat transport,” *Nature communications*, vol. 11, no. 1, pp. 1–9, 2020.
- [83] J. Hodeau, M. Marezio, C. Roucau, R. Ayroles, A. Meerschaut, J. Rouxel, and P. Monceau, “Charge-density waves in nbse3 at 145k: Crystal structures, x-ray and electron diffraction studies,” *Journal of Physics C: Solid State Physics*, vol. 11, no. 20, p. 4117, 1978.
- [84] S. Srivastava and B. Avasthi, “Preparation, structure and properties of transition metal trichalcogenides,” *Journal of materials science*, vol. 27, no. 14, pp. 3693–3705, 1992.
- [85] S. van Smaalen, J. L. de Boer, A. Meetsma, H. Graafsma, H.-S. Sheu, A. Darovskikh, P. Coppens, and F. Levy, “Determination of the structural distortions corresponding to the q 1-and q 2-type modulations in niobium triselenide nbse 3,” *Physical Review B*, vol. 45, no. 6, p. 3103, 1992.
- [86] L. Yang, *Phonon Transport in Nanowires–Beyond Classical Size Effects*. Vanderbilt University, 2019.
- [87] Q. Zhang, C. Liu, X. Liu, J. Liu, Z. Cui, Y. Zhang, L. Yang, Y. Zhao, T. T. Xu, Y. Chen, *et al.*, “Thermal transport in quasi-1d van der waals crystal ta2pd3se8 nanowires: size and length dependence,” *ACS nano*, vol. 12, no. 3, pp. 2634–2642, 2018.
- [88] L. Yang, Y. Tao, Y. Zhu, M. Akter, K. Wang, Z. Pan, Y. Zhao, Q. Zhang, Y.-Q. Xu, R. Chen, *et al.*, “Observation of superdiffusive phonon transport in aligned atomic chains,” *Nature nanotechnology*, vol. 16, no. 7, pp. 764–768, 2021.
- [89] J. Wang, Q.-A. Huang, and H. Yu, “Size and temperature dependence of young’s modulus of a silicon nano-plate,” *Journal of physics D: Applied physics*, vol. 41, no. 16, p. 165406, 2008.

- [90] X. Sun, X. Liu, J. Yin, J. Yu, Y. Li, Y. Hang, X. Zhou, M. Yu, J. Li, G. Tai, *et al.*, “Two-dimensional boron crystals: Structural stability, tunable properties, fabrications and applications,” *Advanced Functional Materials*, vol. 27, no. 19, p. 1603300, 2017.
- [91] A. R. Oganov, J. Chen, C. Gatti, Y. Ma, Y. Ma, C. W. Glass, Z. Liu, T. Yu, O. O. Kurakevych, and V. L. Solozhenko, “Ionic high-pressure form of elemental boron,” *Nature*, vol. 457, no. 7231, pp. 863–867, 2009.
- [92] J. He, E. Wu, H. Wang, R. Liu, and Y. Tian, “Ionicities of boron-boron bonds in b 12 icosahedra,” *Physical review letters*, vol. 94, no. 1, p. 015504, 2005.
- [93] Z. Zhang, E. S. Penev, and B. I. Yakobson, “Two-dimensional boron: structures, properties and applications,” *Chemical Society Reviews*, vol. 46, no. 22, pp. 6746–6763, 2017.
- [94] V. Domnich, S. Reynaud, R. A. Haber, and M. Chhowalla, “Boron carbide: structure, properties, and stability under stress,” *Journal of the American Ceramic Society*, vol. 94, no. 11, pp. 3605–3628, 2011.
- [95] H. Werheit, “On microstructure and electronic properties of boron carbide,” in *Advances in Ceramic Armor X: A Collection of Papers Presented at the 38th International Conference on Advanced Ceramics and Composites January 27–31, 2014*, vol. 35, pp. 87–102, Wiley Online Library, 2014.
- [96] A. Bute, S. Jena, D. Bhattacharya, S. Kumar, N. Chand, N. Keskar, and S. Sinha, “Composition dependent microstructure and optical properties of boron carbide (bxc) thin films deposited by radio frequency-plasma enhanced chemical vapour deposition technique,” *Materials Research Bulletin*, vol. 109, pp. 175–182, 2019.
- [97] C. Cheng, K. M. Reddy, A. Hirata, T. Fujita, and M. Chen, “Structure and mechanical properties of boron-rich boron carbides,” *Journal of the European Ceramic Society*, vol. 37, no. 15, pp. 4514–4523, 2017.
- [98] L. E. Bell, “Cooling, heating, generating power, and recovering waste heat with thermoelectric systems,” *Science*, vol. 321, no. 5895, pp. 1457–1461, 2008.
- [99] A. I. Hochbaum, R. Chen, R. D. Delgado, W. Liang, E. C. Garnett, M. Najarian, A. Majumdar, and P. Yang, “Enhanced thermoelectric performance of rough silicon nanowires,” *Nature*, vol. 451, no. 7175, pp. 163–167, 2008.
- [100] H. Werheit, B. Herstell, W. Winkelbauer, G. Pristáš, S. Gabáni, K. Flachbart, and S. Shalamberidze, “Electrical conductivity of boron carbide from 5 to 2100 k in the whole homogeneity range,” *Solid State Sciences*, vol. 132, p. 106987, 2022.

- [101] D. Zhang, D. McIlroy, Y. Geng, and M. G. Norton, "Growth and characterization of boron carbide nanowires," *Journal of materials science letters*, vol. 18, no. 5, pp. 349–351, 1999.
- [102] M. Carlsson, F. J. García-García, and M. Johnsson, "Synthesis and characterisation of boron carbide whiskers and thin elongated platelets," *Journal of crystal growth*, vol. 236, no. 1-3, pp. 466–476, 2002.
- [103] R. Ma and Y. Bando, "High purity single crystalline boron carbide nanowires," *Chemical Physics Letters*, vol. 364, no. 3-4, pp. 314–317, 2002.
- [104] R. Ma and Y. Bando, "Investigation on the growth of boron carbide nanowires," *Chemistry of materials*, vol. 14, no. 10, pp. 4403–4407, 2002.
- [105] B. Li-Hong, L. Chen, T. Yuan, T. Ji-Fa, H. Chao, W. Xing-Jun, S. Cheng-Min, and G. Hong-Jun, "Synthesis and photoluminescence property of boron carbide nanowires," *Chinese Physics B*, vol. 17, no. 12, p. 4585, 2008.
- [106] A. Velamakanni, K. Ganesh, Y. Zhu, P. J. Ferreira, and R. S. Ruoff, "Catalyst-free synthesis and characterization of metastable boron carbide nanowires," *Advanced Functional Materials*, vol. 19, no. 24, pp. 3926–3933, 2009.
- [107] X. Tao, L. Dong, X. Wang, W. Zhang, B. J. Nelson, and X. Li, "B₄C-nanowires/carbon-microfiber hybrid structures and composites from cotton t-shirts," *Advanced Materials*, vol. 22, no. 18, pp. 2055–2059, 2010.
- [108] W.-B. Luo, S.-L. Chou, J.-Z. Wang, and H.-K. Liu, "Ab 4 c nanowire and carbon nanotube composite as a novel bifunctional electrocatalyst for high energy lithium oxygen batteries," *Journal of Materials Chemistry A*, vol. 3, no. 36, pp. 18395–18399, 2015.
- [109] L. Luo, S.-H. Chung, H. Yaghoobnejad Asl, and A. Manthiram, "Long-life lithium–sulfur batteries with a bifunctional cathode substrate configured with boron carbide nanowires," *Advanced Materials*, vol. 30, no. 39, p. 1804149, 2018.
- [110] Y. Liao, "Practical electron microscopy and database-an online book," *can be found under <http://www.globalsino.com/EM/>, nd*, 2018.
- [111] P. Gadkari, A. Warren, R. Todi, R. Petrova, and K. Coffey, "Comparison of the agglomeration behavior of thin metallic films on SiO₂," *Journal of Vacuum Science & Technology A: Vacuum, Surfaces, and Films*, vol. 23, no. 4, pp. 1152–1161, 2005.
- [112] J.-Y. Kwon, T.-S. Yoon, K.-B. Kim, and S.-H. Min, "Comparison of the agglomeration behavior of Au and Cu films sputter deposited on silicon dioxide," *Journal of applied physics*, vol. 93, no. 6, pp. 3270–3278, 2003.

- [113] J. Petersen and S. Mayr, "Dewetting of ni and niag solid thin films and formation of nanowires on ripple patterned substrates," *Journal of Applied Physics*, vol. 103, no. 2, p. 023520, 2008.
- [114] A. M. Thron, P. Greene, K. Liu, and K. van Benthem, "In-situ observation of equilibrium transitions in ni films; agglomeration and impurity effects," *Ultra-microscopy*, vol. 137, pp. 55–65, 2014.
- [115] K. Banno, M. Mizuno, K. Fujita, T. Kubo, M. Miyoshi, T. Egawa, and T. Soga, "Transfer-free graphene synthesis on insulating substrates via agglomeration phenomena of catalytic nickel films," *Applied Physics Letters*, vol. 103, no. 8, p. 082112, 2013.
- [116] R. Lamber, N. Jaeger, and G. Schulz-Ekloff, "On the metal-support interaction in the ni-sio 2 system," *Surface science*, vol. 227, no. 3, pp. 268–272, 1990.
- [117] A. M. Thron, P. K. Greene, K. Liu, and K. van Benthem, "Structural changes during the reaction of ni thin films with (1 0 0) silicon substrates," *Acta materialia*, vol. 60, no. 6-7, pp. 2668–2678, 2012.
- [118] M. Liehr, H. Lefakis, F. LeGoues, and G. Rubloff, "Influence of thin sio 2 interlayers on chemical reaction and microstructure at the ni/si (111) interface," *Physical Review B*, vol. 33, no. 8, p. 5517, 1986.
- [119] H. Dallaporta, M. Liehr, and J. Lewis, "Silicon dioxide defects induced by metal impurities," *Physical Review B*, vol. 41, no. 8, p. 5075, 1990.
- [120] J. Mayer, R. Lin, and E. Garfunkel, "Surface and bulk diffusion of adsorbed nickel on ultrathin thermally grown silicon dioxide," *Surface science*, vol. 265, no. 1-3, pp. 102–110, 1992.
- [121] Y. Wei, R. M. Wallace, and A. C. Seabaugh, "Void formation on ultrathin thermal silicon oxide films on the si (100) surface," *Applied physics letters*, vol. 69, no. 9, pp. 1270–1272, 1996.
- [122] A. Earnshaw and N. N. Greenwood, *Chemistry of the Elements*, vol. 60. Butterworth-Heinemann Oxford, 1997.